OPTIMIZING THE DISPERSION OF CERAMIC NANOPARTICLES AND ASSESSING THE ROLE OF AGGREGATION IN MEDIATING BIOLOGICAL ACTIVITY

A Thesis Submitted to
the Graduate School of
İzmir Institute of Technology
in Partial Fulfillment of the Requirement for the Degree of

MASTER OF SCIENCE

in Biotechnology

by
Anıl Can ÖNDER

July 2022
İZMİR

ACKNOWDLEDGMENTS

First and foremost, I would like to express my gratitude to my supervisor: Asst. Prof. Ceyda ÖKSEL KARAKUŞ who believed in me and supported my scientific ideas and ambition. I am genuinely grateful for the support, guidance, and immense knowledge that I have been procured during my thesis period. I feel privileged to make her acquaintance because of her open-mindedness and selfless nature that made me feel trusted and cared for. I have been provided with encouragement to pursue my scientific interests without whom it might not be possible.

I would like to thank my laboratory colleague Dr. Aysel TOMAK who helped me in every aspect during this long process and made a remarkable contribution to my thesis and knowledge. I also am delighted to be a member of the BioNanoLab. I would like to thank my laboratory colleagues: Selin ÇEŞMELİ, Eyüp BİLGİ, M. Semih BAŞLAR, and Melisa TÜNCER who supported me and accompanied me on this path.

I would like to thank my co-advisor Prof. Mehmet POLAT and Prof. Hürriyet POLAT for their undeniable contribution to my knowledge about colloidal chemistry and dispersion. Also, I am deeply grateful to Prof. Ekrem ÖZDEMİR and Assoc. Prof. Sevgi KILIÇ ÖZDEMİR who allowed me to use their dynamic light scattering equipment throughout my thesis period.

I would like to offer my special thanks to Prof. Erdal BEDİR for being my mentor and advisor through the progression of my thesis.

I am not able to express how I feel for all my friends that motivated me in my academic journey, but the special snowflakes are Tolunay ARSLAN, Ege VATAN, K. Şafak ALKAN, Filiz BAŞER, Miray KURTOĞLU, and Burak YASDI.

As for many things in life, this research would not be fulfilled without the support of my family. Thank you Şengül, Emir, Suat. For all the things during this long path, you all made it possible.

Last but not the least, my eternal gratitude and affection to my angel in disguise: Duygu EŞTÜRK who has supported me in every aspect, not only in this period but beyond, and has made me feel loved. I would cease to exist without her.

ABSTRACT

OPTIMIZING THE DISPERSION OF CERAMIC NANOPARTICLES AND ASSESSING THE ROLE OF AGGREGATION IN MEDIATING BIOLOGICAL ACTIVITY

The aim of this study is to optimize the sample preparation protocol for dispersing powder-form ceramic nanoparticles (CeNPs) in liquid media by leveraging the power of the design of experiment approach to narrow down potential causes of aggregation and to investigate the subsequent effect of CeNP aggregation on the biological activity of SaOS-2 human osteosarcoma cells. Dispersion of the nanopowders is one of the problems in the nanotechnology field because of the tendency of the nanoparticles for aggregation. Although there are existing dispersion protocols, they offer a one-size-fits-all approach overseeing the unique physicochemical properties of the different nanomaterials. In this study, optimization of the sample preparation protocol for two CeNPs was assessed via the investigation of the most contributing parameters and their synergetic effect through measurements of Z-average and zeta potential. Evaluation of these parameters allowed the development of two different models for each nanomaterial, predicting Z-average and zeta potential for given parameter sets. Through these models, two different sample sets were selected to evaluate the effect of aggregation on the SaOS-2 cell line. Outcomes show that the concentration of nanomaterial, pH, and the presence of additive molecule are three main parameters that affect dispersion stability. It was seen that these parameters can be included in a design to develop an efficient model to predict Z-average and zeta potential for investigated nanomaterials. Moreover, cell viability tests show that there is no significant difference between untreated and nanomaterial-treated cells. The findings promise that tailor-made and reliable dispersion protocols for different nanopowders can be developed via design of experiment.

ÖZET

SERAMİK NANOPARÇACIKLARIN DAĞILIMININ OPTİMİZASYONU VE KÜMELENMENİN BİYOLOJİK AKTİVİTEDEKİ ROLÜNÜN DEĞERLENDİRİLMESİ

Bu tezin amacı toz formdaki seramik nanoparçacıkların (CeNPs) sıvı ortamdaki dağılımını optimize etmek için deney dizayn yaklaşımından faydalanılıp CeNP kümelenmesinin potansiyel sebeplerini irdelemek ve CeNP kümelenmesinin etkisi sonucunda SaOS-2 insan osteosarkom biyolojik aktivitesinin araştırılmasıdır. Nanotozların dağılımı, nanoparçacıkların kümelenme eğilimi dolayısıyla nanoteknoloji alanında karşılaşılan problemlerden biridir. Dağılım protokolleri halihazırda mevcut olsa da bu protokoller her bir nanomalzemenin eşsiz fizikokimyasal özelliklerini yok saymakta ve tüm nanomalzemeler için aynı yöntemi önermektedir. Bu çalışmada iki farklı CeNP için örnek hazırlama protokolü, dağılıma en çok etki eden parametreler ve bu parametreler arasındaki sinerjik etki araştırılarak Z-average ve zeta potansiyel ölçümleri aracılığıyla oluşturulmuştur. Bu parametrelerin değerlendirilmesi her nanomalzeme için verilen parametrelere göre Z-average ve zeta potensiyel değerlerini tahmin edebilen iki farklı model oluşturmaya olanak sağlamıştır. Bu modeller aracılığıyla iki farklı parametre seti seçilmiş ve kümelenmenin SaOS-2 hücre canlılığına olası etkileri araştırılmıştır. Sonuçlar, nanomalzeme konsantrasyonu, pH, ve ilave molekül varlığının dağılım dengesini etkileyen başlıca parametreler olduklarını göstermektedir. Bu parametrelerin seçilmiş nanomalzemeler için Z-average ve zeta potansiyel değerlerini tahmin edebilen verimli bir model oluşturmak için kullanılabileceği gösterilmiştir. Bununla birlikte, hücre canlılığı testleri sonuçlarında kümelenmenin hücre canlılığına etkisinde anlamlı bir farklılığa rastlanmamıştır. Bulgular deney dizaynı yöntemi kullanılarak farklı nanotozlar için güvenilir dağılım protokolleri geliştirilebileceğini göstermektedir.

TABLE OF CONTENTS

LIST OF FIGURES

Figure **Page**

Figure **Page**

Figure **Page**

LIST OF TABLES

Table **Page**

LIST OF ABBREVIATONS

ANOVA	Analysis of Variance
BSA	Bovine Serum Albumin
CeNP	Ceramic Nanoparticle
DLS	Dynamic Light Scattering
DLVO	Derjaguin, Landau, Verwey, Overbeek
DMEM	Dulbecco's Modified Eagle's Medium
EDL	Electrical Double Layer
EDX	Energy-dispersive X-ray
FBS	Fetal Bovine Serum
FCM	Flow Cytometry
FTIR	Fourier Transform Infrared Spectroscopy
HAp	Hydroxyapatite
ICP-MS	Inductively Coupled Plasma - Mass Spectrometry
ISO	International Organization for Standardization
NP	Nanoparticle
OECD	Organization for Economic Co-operation and Development
PBS	Phosphate Buffer Saline
SEM	Scanning Electron Microscope
TCP	Tricalcium Phosphate
TGA	Thermogravimetric Analysis
XRD	X-ray Diffraction

CHAPTER 1

INTRODUCTION

Ceramic nanoparticles (CeNPs) are increasingly used as bioresorbable bone replacement materials due to their biocompatibility and similar composition to the inorganic fraction of human bone. They are usually synthesized using chemical routes such as sol-gel and co-precipitation in the form of powders. Therefore, dispersing CeNPs in a suitable medium using a rigorous approach is a key requirement for various applications and purposes, ranging from lab-scale evaluation of physicochemical and toxicological properties to industrial-scale optimization of the final product and its performance. Although there are different sample preparation procedures for dispersing nanopowders in liquids (NANOGENOTOX, OECD, ISO protocols, etc.) these documented approaches are mostly based on the one-size-fits-all principle and do not differentiate enough between various types of nanoparticles (e.g. metal oxide, carbon-based, or ceramic nanoparticles). Considering the potential of the dispersion quality-related characteristics such as particle size and aggregation state in governing biological activity, there is a clear need to optimize dispersion protocol for commercial CeNPs in a way to ensure well-dispersed samples with uniform size distribution.

Here, the scope of this thesis is to investigate the most influential dispersion parameters by combining two different design of experiment (DoE) approaches: Plackett-Burman design (PBD), and central composite design (CCD) and to develop modified dispersion protocols for two different CeNPs that are commonly used in dental applications, hydroxyapatite (HAp) and tricalcium phosphate (TCP). Dispersion quality was equated to the Z-average value and monitored changes in particle size using SEM and DLS techniques. To compare the effect of aggregation on cytotoxic activity, two different samples were prepared, a well-dispersed and aggregated CeNP dispersions. Next, SaOS-2 human osteosarcoma cells were treated with varying concentrations of these two CeNP dispersions for 24h. Their cytotoxic (or proliferative) potential was assessed by WST-1 assay.

This thesis consists of five chapters. In Chapter 1, brief information about the course of the thesis is given. Chapter 2 describes the theoretical foundations of the colloidal dispersions and the corresponding nanomaterial dispersion parameters together

with the basics of DOE approaches used to construct a logical experimental plan that ensures the efficient use of time and resources. Chapter 2 also enlightens nanomaterial-mediated biological activity, providing a perspective on cell viability assessment of CeNP-treated SaOS-2 cells. The experimental approach has been explained in detail in Chapter 3 whilst corresponding results of these experiments are evaluated in Chapter 4. Chapter 5 concludes the thesis with a critical discussion of the findings and provides suggestions for future research.

CHAPTER 2

LITERATURE REVIEW

2.1. Colloidal Dispersion

Mixtures can be primarily divided into two categories: homogenous mixtures involving ionic or covalent solids that disperse evenly in a solvent and heterogenous mixtures involving two or more phases with non-uniform compositions. Colloids are a type of mixtures that fall between a solution and a heterogeneous suspension. To provide a theoretical basis for colloidal solutions, this chapter focuses on the interactions governing colloid stability and the role of intrinsic/extrinsic parameters in these interactions.

2.1.1. Mechanism of Colloidal Dispersion

Colloidal dispersion mainly occurs due to the movement of the particles and their interactions in a suspension. This movement is known to be correlated with particle-particle and particle-environment interactions. In the case of nanoparticle dispersions, the suspension to be dispersed consists of nanoparticle, the dispersion medium, and dispersive agents (Porter et al., 2008). Therefore, the complexity of interactions in dispersion comes from these chemical constituents.

Particle-related parameters and system conditions influence colloidal dispersion in unique ways. Physicochemical properties of nanoparticles such as shape, size, and density control different dimensions of the dispersion (Baysan et al., 2021). In particular, concentration and the surface properties including the surface charge of nanoparticles play a crucial role in the dispersion (Dai et al., 2020). Since nanoparticles in the colloid suspension are likely to interact with themselves and their surrounding environment, both particle-particle and particle-environment interactions contribute to the total interaction energy governing whether the particles will form aggregates or remain in a monodisperse state.

Although there are various types of interparticle forces (i.e. solvation, entropic, short-range) acting on a nanoparticle in a liquid medium, colloidal dispersion is mainly affected by electrostatic forces such as van der Waals forces, and steric forces (Rosen & Kunjappu, 2012) (Yu et al., 2018). Moreover, the intrinsic properties of a nanomaterial play a prominent role in dispersion. Nanoparticles with the same physicochemical properties dispersed in ultra-pure water medium yields both attractive and repulsive forces on the nanoparticle that are highly affected by the nanoparticle's structural properties. In particular, attraction forces acting on nanoparticles are mainly driven by van der Waals forces whereas the repulsion is caused by electrostatic forces (Yu et al., 2018). Moreover, the addition of dispersant to the system affects the colloidal suspension depending on the dispersant's physicochemical properties and concentration due to the possible interactions of nanoparticles with the dispersant molecule. More specifically, the dispersant contributes to the steric force together with the electrostatic force acting on the nanoparticle (Rosen & Kunjappu, 2012). Therefore, electrostatic stabilization and steric stabilization should be considered when controlling the colloidal stability of nanoparticle dispersions.

2.1.2. Electrostatic and Steric Stabilization

Nanoparticles in a suspension are charged if they are present in polar or any liquid with a high dielectric constant (Cao, 2004). The electrical charge density of a nanoparticle is affected by the pH of the suspension. Ions in the suspension that are adsorbed on the layer of the nanoparticle regulate the surface charge (Cao, 2004). The surface charge of a nanoparticle in a suspension is affected by the concentration of charge-determining ions in the environment. Considering the suspension environment is composed of H+ and OH- ions of water molecules, thus the pH value affects the surface charge of the nanoparticle. The value of pH in which the resulting surface charge of a nanoparticle is zero is called point zero charge (pzc). Moreover, surface charge density (E), is correlated with pH, the gas constant (R_g), temperature (T), and Faraday constant (F), derived from the Nernst equation given in Equation 2.1. (Cao, 2004).

$$E = \frac{2.303\ R_g T\ [(p.z.c. - pH)]}{F} \tag{2.1}$$

After the establishment of the surface charge for a nanoparticle, electrostatic forces act on the surface of the nanoparticle and molecules in proximity. The resulting segregation of positive and negative charges, combined with random movement of particles which is called Brownian motion, and dispersion in a system leads to the formation of an electrical double layer (EDL) (Israelachvili, 2011). EDL consists of both determining ions from the surface charge of a nanoparticle and counter ions from the suspension which are opposite charged ions of determining ions (Israelachvili, 2011). EDL consists of two layers separated by the Helmholtz plane (Israelachvili, 2011). These layers are called the Stern layer and the Gouy layer (diffuse double layer) (Israelachvili, 2011). The Stern layer is the region between the surface of a nanoparticle and the Helmholtz plane. In the Stern layer, counter ions in a suspension are attracted by the surface ions of a nanoparticle and the concentration of counter ions decrease as they are farther away from the surface (Israelachvili, 2011). Beyond the Helmholtz plane, the counter ions reach the average concentration level in the region called the Gouy layer (Israelachvili, 2011). The change in the electrical potential is related to the thickness of the Stern layer (H) (Cao, 2004).

$$E \propto e^{-\kappa(h-H)} \tag{2.2}$$

Beyond the Helmholtz plane, $1/\kappa$ which is called Debye-Hückel screening strength can also be used to represent the EDL thickness where C_i and Z_i are the concentration and valence of the counter ions and ε_0 and ε_r are dielectric constant of the solvent and permittivity of vacuum respectively (Cao, 2004).

According to the Debye-Hückel screening strength, the electrical potential at the solid surface and its proximity decreases with the increasing concentration and valence of the counter ions increase. Moreover, an increased dielectric constant of the solvent would result in increased electrical potential (Cao, 2004).

$$\kappa = \sqrt{\frac{F^2 \sum_i C_i Z_i^2}{\varepsilon_r \varepsilon_0 R_g T}} \tag{2.3}$$

Electrical potential and electrostatic interactions between particles govern the dispersion characteristics (Rosen & Kunjappu, 2012). The electrostatic repulsion of the

nanoparticles with the same charge in a suspension is the result of overlapping EDLs. If two particles are distant, there will not be an EDL overlap and the resulting electrostatic repulsion between two particles would consequently be zero (Rosen & Kunjappu, 2012). As the distance between two particles decreases and their EDLs overlap, repulsive force between two particles is developed (Cao, 2004). The developed electrical repulsion (Φ_R) between the same particles with spherical shapes is correlated with their radius r and separation distance S.

$$\Phi_R=2\pi\varepsilon_r\varepsilon_0 rE^2 e^{-\kappa S} \tag{2.4}$$

When electrostatic stabilization of nanoparticles in a suspension is considered, van der Waals forces play a crucial role, the significance of which becomes more prominent at short distances. Van der Waals forces together with Brownian motion lead to particle collision and interactions which, in return, causes agglomeration (Rosen & Kunjappu, 2012). The sum of all molecular interactions of the individual nanoparticles represents the van der Waals interaction between two nanoparticles (Israelachvili, 2011). Between two identical spherical nanoparticles with radius r and separation distance S, an attraction potential (Φ_A) arises.

Natural attraction interaction between two particles is represented as a negative sign (Cao, 2004). Hamaker constant, A, is dependent on the number of atoms per unit volume and the London dispersion constant. It is a positive constant arising from the polarization properties of both interacting materials as well as the suspension medium (Ohshima & Makino, 2014).

$$\Phi_A=-\frac{A}{6}\left\{\frac{2r^2}{S^2+4rS}+\frac{2r^2}{S^2+4rS+4r^2}+\ln\left(\frac{S^2+4rS}{S^2+4rS+4r^2}\right)\right\} \tag{2.5}$$

Dispersion of solid nanoparticles in a liquid phase can be affected by steric forces regardless of the presence of electrical barriers. These steric forces can act on a nanoparticle as the lyophilic chains of molecules are adsorbed onto the particle's surface and influence the interactions between nanoparticle bodies. These interactions result in two effects called the mixing effect and the entropic effect (Israelachvili, 2011). Chain overlapping of the extended solvent-chain interactions of the steric bodies is called the mixing effect. If the solvent-chain interaction is stronger than the overlapped chain-chain

interaction, an energy barrier is developed due to the increase in free energy, thus the nanoparticles repulse each other (Israelachvili, 2011). In the case of attraction, chain-chain interactions are stronger than solvent-chain interactions and the nanoparticles attract each other due to the decrease in free energy (Israelachvili, 2011). The entropic effect, on the other hand, is the effect that is occurred because of the restriction of mobility of the chains extending into the liquid phase. This restriction makes adjacent close-proximity nanoparticles unable to interact with each other (Israelachvili, 2011). Both effects contribute to the overall stability of the dispersion.

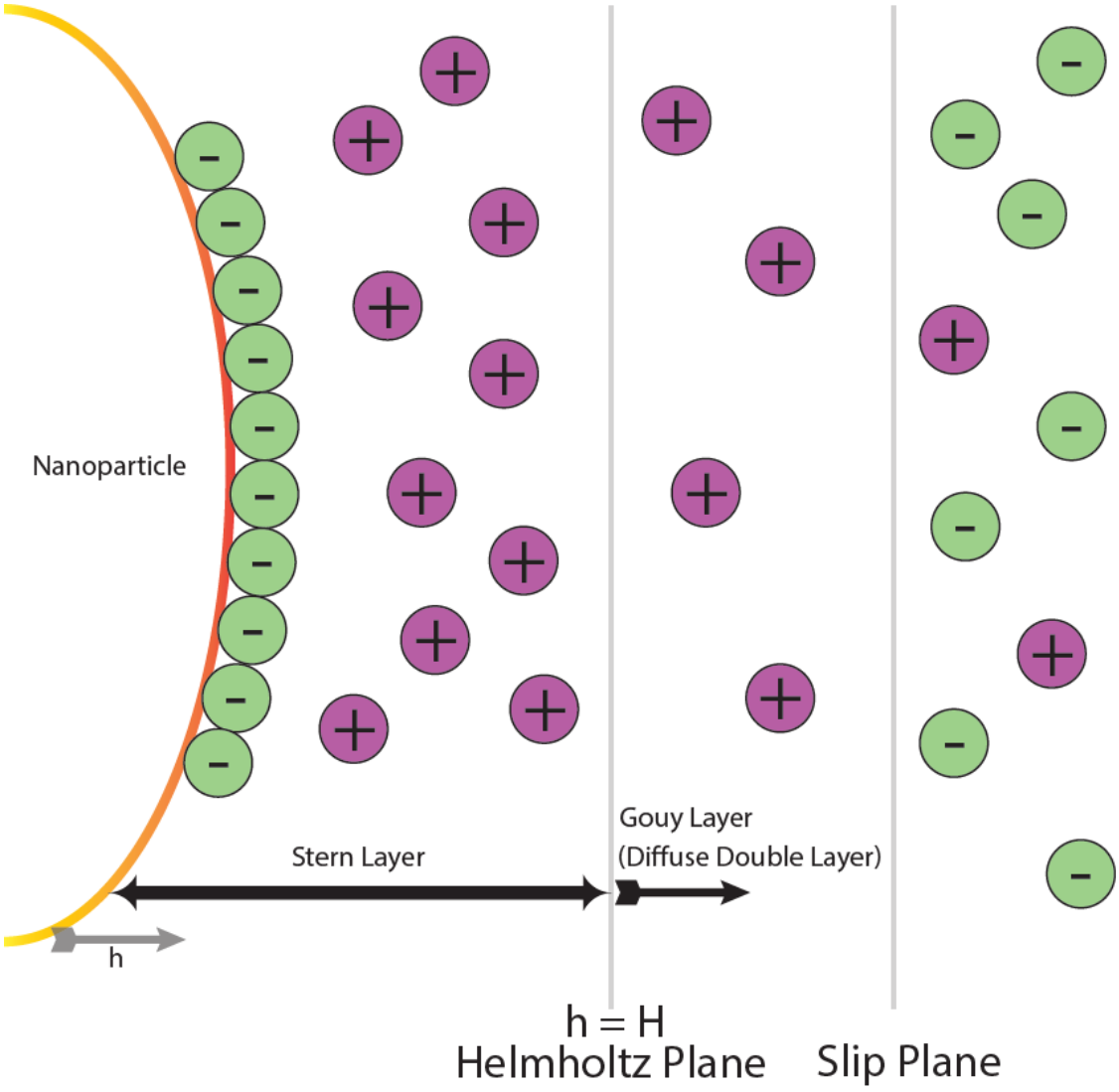

Figure 2.1. Illustration of the electrical double layer structure, nanoparticle surface charge is assumed and represented as negative.

Interactions of nanoparticles with their surrounding environment govern the dispersion stability. In theory, overall interactions determine whether the particles will attract each other and form aggregates or repel each other to achieve efficient mono-dispersion. In colloidal science, the relationship between electrostatic interactions and dispersion stability is explained by DLVO theory. DLVO theory states that total interaction energy (Φ_T) corresponds to the summation of Φ_R and Φ_A.

$$\Phi_T = \Phi_R + \Phi_A \tag{2.6}$$

2.1.3. DLVO Theory

Derjaguin and Landau in 1941, Verwey and Overbeek in 1948 independently developed a well-established theory about colloidal dispersion stability, explaining the nature of the electrostatic interactions between particles (Hotze et al., 2010). Named after its contributors, DLVO theory describes the lyophobic dispersions (dispersed particles without any surrounding solvent layer) according to their balance between attractive and repulsive forces acting on the particles. These attractive forces refer to van der Waals forces whereas repulsive forces are represented as the electrostatic interactions between the same-surface-charged particles. When attractive forces overcome repulsion, primary and secondary minimum energy levels are observed in DLVO. Primary minimum indicates that aggregation is promoted due to the relatively low interaction potential energy whereas the secondary minimum is a level where aggregation due to the attractive forces can be reversed (Hotze et al., 2010). Although there are various forces acting on particles other than van der Waals and electrostatic, DLVO simply explains the colloidal stability via the summation of these two forces. Since there is a clear need for the inclusion of the forces that contribute to the particle-particle interaction, an extended version of DLVO (xDLVO) theory is proposed to take into account these additional collective forces such as steric repulsion forces that contribute to the stability of dispersions (Hotze et al., 2010). These collective forces may present challenges to understanding aggregation in the case of nanomaterial-included systems since more than one xDLVO force is important to evaluate dispersion stability because of the short-distance forces acting on nanoparticles (Hotze et al., 2010).

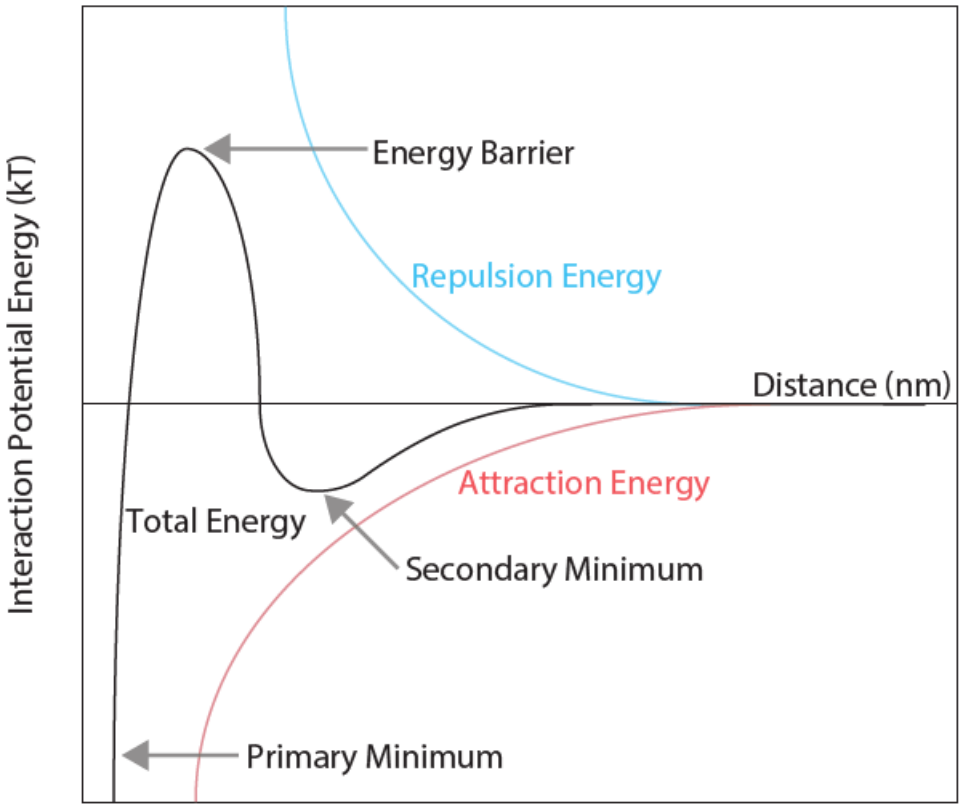

Figure 2.2. DLVO total energy graph representation.

DLVO theory cannot fully explain nanoparticle dispersion kinetics because of the unique physicochemical properties that nanomaterials possess. Since nanoparticles are small enough in size, the surface curvature of the nanoparticle cannot be assumed to be flat unlike in DLVO (Hotze et al., 2010). Moreover, the Hamaker constant that governs van der Waals attraction also interferes with the DLVO framework in nanoparticle dispersions. Nanoparticles that have a high inherent tendency to form aggregates usually have greater Hamaker constants (Hotze et al., 2010). Bulk materials that have molecular structures favoring the permanent or induced dipoles by van der Waals attraction usually have a high Hamaker constant value (Hotze et al., 2010). Besides that, the Hamaker constant is also correlated with the crystal structure of the nanoparticle (Hotze et al., 2010). In addition, some nanomaterials that have magnetic or hydrophobic interactions such as ferromagnetic nanomaterials may promote aggregation (Hotze et al., 2010). Moreover, DLVO theory assumes that the particles in the discussion are spherical. However, there are various shaped nanoparticles that can be produced. DLVO model further fails to efficiently include complex surfactant and surface coating molecules that

are present in the nanoparticle-containing suspensions to achieve more stable dispersions (Hotze et al., 2010).

Given the explained reasons in this subchapter, it is not possible to accurately model nanoparticle dispersions based on the principles of DLVO theory, hence, parameters affecting the dispersion stability of nanoparticles must be evaluated individually. Deriving from the DLVO theory, interfering properties of nanomaterial dispersion can be assessed in practice to some level.

2.2. Parameters Affecting Nanomaterial Dispersion

Nanoparticles are used in various applications in the biomedical field. When produced in powder form, nanoparticles require elaborative investigation since their appropriate evaluation is achieved optimally when the particles are in a monodisperse state. In general, small nanoparticles in a suspension are considered to have higher toxicity levels. (Sukhanova et al., 2018; Carnovale et al., 2019; Quintero-Quiroz et al., 2019). Hence, aggregation of nanoparticles may result in deceptive outcomes in nanotoxicity measurements. Therefore, sample preparation and the dispersion of the nanoparticles prior to the nanoparticle characterization are crucial to proceeding with biomedical studies. After recognizing the importance of aggregation state for the success of *in vivo* applications, various projects have proposed distinct guidelines to provide standardized protocols of sample preparation and nanoparticle dispersion prior to risk evaluation of nanomaterials. The dispersion protocols of international research projects such as ENPRA (Jacobsen et al., 2018), PROSPEcT (OECD WPMN, 2009), NANOGENOTOX (Jensen et al., 2011), NANOMMUNE (Nanommune, 2010), and standardization institutes such as NIST (Taurozzi et al., 2011) and CEINT (Taurozzi et al., 2012) are widely followed by researchers in the field (Warheit, 2018; Mahbubul et al., 2015). Together with these protocols, tailor-made approaches to dispersion methodology are prevalent and trending in the biomedical field (Demir et al., 2015; Barnes et al., 2008). Although these protocols differ in distinct key parameters of the sample preparation for preparing nanoparticle dispersion, they all aim to achieve the goal of providing a basis for reproducible and widely applicable dispersion protocol.

Sample preparation is a crucial part of the nanoparticle dispersion process. Some of the key parameters such as the concentration of nanoparticles in solution, pre-wetting

process, dispersion medium and its content, sonication parameters, and dispersive agents determine the vast majority of the outcome of the dispersion process through sample preparation, together with nanomaterial's intrinsic properties such as its morphological and surface characteristics (Khan et al., 2019). Even though a standardized dispersion protocol is required to maintain the integrity of reproducible and consistent data production, it may not be sufficient to approach every individual nanomaterial with the same aspect because of the specificity of the material properties. Existing projects in the nanoscience field propose slightly modified dispersion protocols which, in theory, can be used for different classes of nanomaterials. However, overlooking the phenomenon that every material has unique properties can lead to a misinterpretation of the results obtained via existing one-size-fits-all protocols. The dispersion state is highly affected by the properties of the nanoparticle and its interactions with the environment. Therefore, modifying existing dispersion protocols according to nanoparticle specifications may improve the quality and stability of nanoparticle dispersion. Moreover, practical approaches such as *in vitro* toxicological assessments and implications of nanoparticles in biomedical systems show that colloidal stability of dispersed nanomaterials may alter due to particle-specific interactions and the formation of undesired effects such as aggregation or protein corona formation (Monopoli et al., 2011). Therefore, the physicochemical properties of nanomaterials and their specific interactions with the environment should be the primary focus to develop effective dispersion protocols or improving existing approaches.

At every stage of the sample preparation process, experimental parameters such as concentration, sonication parameters, and the use of surfactant govern the characteristics of the dispersion. For example, the concentration of nanoparticles in liquids directly influences the dispersion since the increased concentration of nanoparticles may lead to agglomeration and aggregation because of nanoparticles' interactions due to Brownian motion (Israelachvili, 2011). Moreover, using different sonication instruments that input energy in different levels to the dispersion suspension may affect the interactions between nanoparticles (DeLoid et al., 2017). Furthermore, sample preparation processes for the dispersion of particular nanoparticles can be improved with the availability of tailor-made nanoparticle-specific standard procedures. In particular, special attention should be given to the nanomaterial properties, its concentration in dispersion media, presence/absence of pre-wetting process, dispersion media selection, sonication, and dispersive agents that aid the dispersion.

Physicochemical properties of nanoparticles such as size distribution, surface area, shape, and crystal structure determine the polydispersity of the dispersion through interparticle interactions and interactions of particles with the environment (Rosen & Kunjappu, 2012). Before starting sample preparation for dispersion, particle properties should be known to achieve desired outcomes. Physicochemical characterization of nanoparticles involves a variety of measurements such as particle sizing, visual exploration of particle morphology, and compositional and elemental analysis. Ideally, nanoparticles that are purchased directly from a producer/distributor come with a specification sheet detailing physicochemical parameters. However, in practice, the physicochemical information obtained from the manufacturer needs to be validated and extended to include further characterization with mentioned methods before proceeding with dispersion. Characterization of physicochemical properties of the nanoparticle is the starting point to evaluate the sum of interactions in the dispersion suspension.

Dispersion of nanoparticles with similar surface characteristics may occur following the same phenomena since surface properties primarily affect the dispersion status (Rosen & Kunjappu, 2012). However, considering that each nanomaterial has unique properties, its dispersion stability may differ due to a variety of parameters other than surface characteristics. Alternatively, the coating material of nanoparticles and the aqueous environment in which the powder form nanoparticle was dispersed may affect dispersion stability. Although the surface properties play a prominent role in dispersion, other characteristics are also crucial. Therefore, the generation of standardized protocols for dispersion can be developed by considering surface properties since agglomeration behavior and size distribution are mainly driven by these properties (Rosen & Kunjappu, 2012). A distinct standardized dispersion protocol for a nanoparticle must be developed with consideration of its physicochemical characteristics.

Concentration for the dispersion stock solution should enable the effective execution of subsequent experiments. Therefore, the concentration of the stock solution should be appropriate for serial dilution as well as it should not exceed a limit to avoid undesired agglomeration. For example, the concentration value of the stock solution proposed by ENPRA, NANOGENOTOX, and PROSPeCT which is 2.56 mg/mL is determined based on the required dose for toxicity testing and with consideration of serial dilution (Hartmann et al., 2015). However, the concentration can be determined based on the field of application, thus, existing projects with different perspectives on tackling nanoparticle dispersion-related problems follow various protocols with varying

concentration values from 0.5 mg/mL to 20 mg/mL (Hartmann et al., 2015). Moreover, depending on the utilization of the dispersed media for the subsequent experiments in different areas such as in vitro toxicity testing or nanoecotoxicity, the followed protocol may vary in terms of concentration. Although the stability of stock concentration strictly depends on the material properties, determining the optimal standard value for any given dispersion protocol still might be necessary. Nonetheless, it must be pointed out that every nanoparticle may vary in size, shape, and surface characteristics which, in return, affects the interparticle interactions in the suspension and the optimum concentration value for a given nanoparticle.

Regardless of the stock concentration of the nanomaterial in suspension, pre-wetting may be required to stabilize the dispersion due to the hydrophobic characteristics of a nanomaterial. The hydrophobicity is related to the material's surface properties and the pre-wetting medium displaces air completely from the material's surface (Jahanbakhsh et al., 2021). Hence, materials that are hydrophobic do not form clusters and agglomerate when they encounter dispersing media such as deionized water. This is maintained due to the preparation of the powder material with a hydrophilic molecule with lower surface tension than water in which this pre-wetting agent usually is ethyl alcohol with the surface tension of 0.02 N/m for biomedical nanomaterial dispersions (Khattab et al., 2012).

Not all materials may require pre-wetting. However, standardized dispersion protocols use pre-wetting regardless of the type of the material or application. Although using a pre-wetting agent initially improves the dispersion, it also may affect the surface properties of the material in suspension (Qayyum et al., 2022). Nonetheless, although the used pre-wetting agent would affect the dispersion, potential effects must be considered in terms of follow-up applications such as cellular toxicity assessments. Used agent may cause adverse effects if not removed appropriately from the suspension. Therefore, using pre-wetting agents must be determined based on the application that will be followed, and utilizing the pre-wetting process must be adopted only if the material in discussion is not appropriately dispersed in water because of its properties related to hydrophobicity.

The choice of medium for the dispersion of nanomaterials for nanotoxicology studies must be made in consideration of the simple and defined chemical composition and biological relevance of the liquid medium. The medium to be chosen should allow nanoparticles in suspension to disperse efficiently and prevent the formation of heteroaggregation (aggregation occurred with more than one type of chemical

constituents). In general, due to the biological relevance, ultra-pure water with at least 18.2 MΩ-cm resistivity at 25°C is used in nanoparticle dispersions because of its defined non-toxic characteristics that provide a decent chemical background to avoid unpredicted and uncontrolled dispersion stability issues. The medium of dispersion does not necessarily have to possess essential nutrients for the survival of test organisms, but it should have no toxic effects to proceed with nanotoxicology studies (Hartmann et al., 2015). In addition to ultra-pure water, phosphate buffer saline is one of the media that is used for the dispersion of nanomaterials for biological *in vitro* and *in vivo* studies (Hartmann et al., 2015).

If the nanomaterial dispersion is prepared for toxicology research, the test organism usually is exposed to the nanomaterial of interest prior to the desired toxicity testing. In *in vitro* perspective, this exposure may be achieved by the treatment of the cells with the nanomaterial suspension. Cells are grown in a basal medium such as Dulbecco's Modified Eagle Medium (DMEM) supplemented with growth-promoting serums such as fetal bovine serum (FBS) and dispersed nanomaterials in suspension can be supplemented as well for exposure. The initial nanomaterial dispersion is not prepared with the cell growth media since it is not favorable due to the potential development of protein opsonization (coating of nanoparticles with proteins in the environment) resulting in the formation of a protein-containing layer called protein corona (Lu et al., 2019). Formed protein corona on the surface of a nanoparticle increases the nanoparticle's hydrodynamic diameter and may alter its reactive behavior. Additionally, the dispersion may be facilitated with sonication. In particular, sonicating the culture media promotes the generation of reactive oxygen species and denaturation of the proteins present in the media which may have negative effects on cell viability (DeLoid et al., 2017). Moreover, the stability of various nanomaterials in different culture media (e.g. DMEM with FBS, MEM with FBS, RPMI with FBS, human blood plasma) has been documented and it has been shown that the colloidal stability is affected by the type of media and nanomaterial (Moore et al., 2015). Hence, the choice of the appropriate culture medium for the given nanomaterial is essential.

Dispersion of powder-form nanomaterials is usually accompanied by ultrasonication. The application of sound energy facilitates the dispersion of nanomaterials due to the delivered acoustic energy to the system (DeLoid et al., 2017). Additionally, milder methods can also be utilized such as magnetic stirring, shaking, and vortexing to disperse nanomaterials but these methods may not be sufficient for the

dispersion. Usually, direct, or indirect sonication is used to achieve dispersion, each of which has its own advantages and disadvantages (Hartmann et al., 2015). Probe sonication can be used as a direct method. However, probe sonication requires immersion of the probe into the sample and due to the delivered acoustic energy during the sonication process, probe corrosion can occur and contaminate the sample of interest (Tello et al., 2017). Additionally, probe sonication generates high energy that may result in fracturing some nanoparticles during the process (Sabet et al., 2015). On the other hand, bath sonication can be a reliable alternative for nanomaterials that can be fractured by probe sonication. Bath sonication is an indirect method in which the sample vial is placed inside the bath and sonication induces vibrations to disperse the nanoparticles (DeLoid et al., 2017). Although it does not deliver as high energy as probe sonication does, it is also widely used for nanomaterial dispersions.

Sonication energy and time of sonication can be adjusted according to the nanomaterial to be dispersed. To optimize the settings for the sonication process, it is proposed by several studies (DeLoid et al., 2017; Taurozzi et al., 2011; Hartmann et al., 2015) that delivered acoustic energy of the sonication device with the equipped probe should be calculated. This calculation relies on the increase in the temperature due to the given energy. For each sonication energy amplitude value, an increase in the temperature over time can be recorded until the temperature no longer increases. Thus, the acoustic energy that is delivered by the sonication device can be calculated by the "$P = mC(dT/dt)$" equation. Moreover, delivered critical sonication energy can also be calculated for the given nanomaterial (DeLoid et al., 2017). Above this energy level, a decrease in hydrodynamic size of a given nanomaterial in a liquid phase is no longer seen. Such adjustments can be made to optimize the sonication energy and time parameters for the nanomaterial dispersions.

Sonication should also be assessed from a biological point of view. Sonication may lead to the formation of reactive oxygen species and oxygen radicals and this phenomenon is called sonic activation (Taurozzi et al., 2011). Also, as forementioned, sonication of biological media is not favorable because of the sonic activation phenomenon and denaturation of proteins as a result of sonolysis. Although there are various studies (Caro & Cederbaum, 2004; Brown & Brown, 2012) reporting enhanced toxicity for dispersion prepared by bath and probe sonications compared to non-sonicated dispersions, the observed toxicity cannot be solely attributed to the sonication due to the presence of numerous contributing factors. Moreover, direct comparison of these studies

is inhibited using different parameters such as test organisms, materials, and sonication settings (Hartmann et al., 2015). Overall, obtaining well-dispersed samples with minimal energy input would be a preferred way to achieve nanomaterial dispersion from the biological perspective.

Ultrasonication may not be adequate for the maintenance of monodispersed nanoparticles. In such cases, a dispersing agent can be added to the aqueous media to enhance the stability of the suspension. This enhancement of stability is accomplished by overcoming the attraction forces mainly originated by van der Waals forces through both electrostatic and steric repulsion (Israelachvili, 2011). A dispersing agent may be a natural body such as proteins and glycolipids, as well as synthetic constituents such as dimethyl sulfoxide (DMSO) or sodium dodecyl sulfate (SDS) (Hartmann et al., 2015). A dispersing agent, also called a surfactant or dispersant, should be chosen considering the biological perspective. Ideally, a dispersant should not interfere with the biological activity of the nanomaterial and should not induce toxic effects when in contact with biological tissues.

Dispersing agents are classified based on the nature of their hydrophilic group. These are (1) anionics with a negatively charged surface-active part, (2) cationics with positively charged surface-active regions, (3) zwitterionics with both charges on the surface-active portion, and (4) non-ionic ones without a net charge on the surface-active domain (Rosen & Kunjappu, 2012). The electrostatic interactions of the dispersants with their environment are governed by their ionic characteristics. There are various types of dispersants that have different ionic characters in the aqueous environment. Depending on the physicochemical properties and the behavior of nanoparticles in a liquid phase, various dispersants such as serum proteins, natural organic matter, and poloxamers can be used (Hartmann et al., 2015). Additionally, other dispersants such as SDS, Triton, polyvinylpyrrolidone, and polyethylene glycol are also utilized (Hartmann et al., 2015). Serum proteins are widely used in dispersion sample preparation. Bovine serum albumin (BSA) is the most abundant protein that is found in FBS, and it efficiently enhances the dispersion of many nanomaterials (Tantra et al., 2010). Although possible interactions of nanoparticles with BSA may affect cellular internalization, BSA is a non-toxic dispersing agent contributing to the dispersion stability when ultrasonication itself is insufficient. However, BSA conformation is dependent on the pH, and changes in the pH value might be correlated with the possible dispersant activity of BSA.

One of the critical parameters of dispersion is the pH of the surrounding environment. The pH is directly correlated with the surface charge of the nanoparticles,

as well as the surfactant molecules in the system. Electrostatic stability of nanoparticles is governed by the pH level which is called the point of zero charge or isoelectric point at which the surface charge determining ions are neutralized with the co-ions in the system (Cao, 2004). Above the point of zero charge, nanoparticle surfaces are negatively charged whereas they are positively charged below the point of zero charge. Overall, an increased magnitude of the surface charge of a nanoparticle leads to a more electrostatically stable system (Hartmann et al., 2015). However, the accumulation of counterparts of surface charge ions of a nanoparticle causes a zeta-potential that corresponds to the overall charge of the system around the given nanoparticle (Rosen & Kunjappu, 2012). It has been observed that the zeta-potential of a nanoparticle increases in magnitude as the pH of the environment gets more distant to the point of zero charge of the nanoparticle (Hartmann et al., 2015). Also, additive molecules and dispersion-aiding agents affect the zeta-potential together with the pH of the environment. Since the charges of these molecules are also affected by the pH as well, pH adjustment is crucial for the dispersion and its stability.

Parameters that are relevant for the dispersion procedure may affect each other, making the dispersion process even more complex. Considering the multitude of contributory factors and the specificity of each nanomaterial, the development of an optimized dispersion protocol that is applicable to all nanomaterials is not practical. Rather, a dispersion protocol should be optimized considering the nanomaterial of interest within the boundaries of the effective parameters of dispersion. Considering that even the same type of nanomaterials may possess different physicochemical characteristics (such as varying shape or size), the dispersion protocol may vary between these nanomaterials as well. Concomitantly, a full factorial design that runs all possible combinations of variable level factors may result in a high number of experiments to be performed. Hence, an optimization for the nanomaterial dispersion can be achieved via the consideration of the labor intensity with effective parameters connected to nanomaterial properties. For evaluating the effectiveness of (different combinations of) influential parameters with decreased labor intensity, design of experiment methods can be utilized.

2.3. Design of Experiment

Investigation of the effect of controlled input parameters of a distinct process on its responses can be done via DoE. DoE is an effective statistical approach to analyzing the effectiveness of parameters and their interactions with the response to be evaluated. DoE is utilized to optimize parameters and their values and to design experimental sets that are appropriate to achieve desired response values. Through DoE, initial parameter screening can be conducted to analyze the most effective parameters for the investigated response. As a final optimization, interactions between these influential parameters and their impact on the investigated response can be analyzed to develop a statistical model for the desired experimental design. Two of the widely used methods of DoE for initial and final optimization are parameter screening and response surface analysis.

Amongst many parameters that are considered to have a response effect, it may be useful to analyze which of those parameters are the most effective ones. This approach is exploratory and narrows down the list of parameters with the selection of the factors with the highest contribution. Such designs are called screening designs. Unlike full factorial designs, screening designs require fewer experimental runs, and hence, they are less labor-intensive. Plackett-Burman design (PBD) is one of the screening designs that allows the investigation of the main factors. PBD can screen *n-1* variables with *n* experiments (Vanaja & Shobha Rani, 2007). With a minimum of 12 runs, 12 + 4x experiments (12, 16, 20, etc.) are performed to determine the main factors in PBD (Vanaja & Shobha Rani, 2007). After the initial parameter pool is determined, minimum and maximum values of the parameters are set. PBD generates a matrix with the minimum-maximum values for the corresponding parameters and randomized (block) experimental sets are created. The predetermined response is then measured as the outcome of these experimental sets. Based on the responses, an interpretation of the effect of each individual parameter can be made. This process eliminates the less-important (redundant) parameters and allows for progress with efficient design. Although PBD can elaborate on whether the parameter is effective or not, it does not indicate the quadratic interactions between parameters. Further analysis is required to determine a model that considers the potential interaction between screened parameters.

After all the parameters are screened while searching for the most effective ones, response surface designs can be complementarily done. Interaction of parameters with

each other can be a contributing factor to the response. Since screening designs such as PBD lack the ability to evaluate interactions between parameters, response surface designs conducted after the parameter screening can offer an experimental model that is relevant for the investigated response. Central composite design (CCD) can be given as an example of response surface design. CCD is a fractional factorial design that can be used to model the curvature of the relationship between screened parameters and the response (Yang et al., 2020). Augmentation of center points with "star points" allows such estimation (Bhattacharya, 2021). Augmented star points are new extreme values for each parameter in the design (Bhattacharya, 2021). Estimated curvature of screened parameters via star points are utilized to generate models for the response. Hence, CCD is used to optimize experimental designs by investigating the curvature of the relationship between screened parameters and the response.

In experimental design optimization, it is crucial to determine the initial set of parameters that may potentially affect the result. The theoretical background of any given topic can be implemented with a statistical approach to minimize the number of experiments and labor intensity whilst providing efficient models to represent the data. All the selected parameters can be pretreated via screening designs such as PBD to reduce the number of parameters to be screened. Consequently, response surface designs can be conducted to estimate the factor interactions and curvature of these factors with the response.

Nanomaterial dispersion is affected by various factors. Dispersion of nanoparticles may be influenced by the selected nanomaterial because of the distinct physicochemical characteristics that each nanomaterial possesses. Although nanomaterials are unique in terms of their physicochemical characteristics, there is a clear gap in the assessment of optimized dispersion parameters for different types of nanomaterials. Moreover, parameters that potentially affect the nanomaterial dispersion can be pooled and analyzed to rank their efficiency. In such a case, the most effective parameters for the efficient dispersion can be statistically determined via screening design methods and complementarily optimized via response surface designs. Thus, DoE can be a promising tool to develop an optimized nanomaterial dispersion protocol to assess the effect of nanoparticles on biological activity.

2.4. Effect of Nanoparticles on Cell Viability

From internalization to the extensive molecular mechanisms in cell machinery, nanoparticles may either possess threats or improve the viability of the cells. There are different types of uptake mechanisms that are assumed to be involved in nanoparticle internalization. The cellular uptake of nanoparticles depends on the physicochemical properties of the nanomaterial and its interaction with the cell. The internalized nanoparticles may alter the cellular functions which may affect the rate of cell viability. Hence, the connection between physicochemical properties of the nanomaterial with cell-nanoparticle interactions is a crucial point for the assessment of its effects on the biological response.

Interaction between cells and nanoparticles may affect the viability of the cells. Variety of research, both *in vivo* and *in vitro*, have been conducted to elucidate the effect of nanoparticles on relevant biological responses, especially toxicity. It has been shown that nanoparticles may act as toxic agents that lead cells to perish as well as they may improve the conditions of the cells in a way to increase their rate of viability (Yu et al., 2020; Augustine et al., 2019). Versatile effects of various nanoparticles on different cells and tissues arise from the bioavailability and processability depending on their physicochemical properties. Moreover, *in vitro* nanotoxicity results for nanomaterials may not be correlated with the *in vivo* findings which leads to the necessity of complementary assessments to show the effect of nanoparticles in both *in vitro* and *in vivo* (Fischer & Chan, 2007). Although *in vivo* research validation is required for the appropriate nanotoxicity assessment, *in vitro* experiments still present a valid checkpoint as the fundamentals.

In general, physicochemical properties of nanoparticles such as size, shape, surface charge, and coating determine the effect of the nanomaterial on the cell (Sharifi et al., 2012). The effect of nanoparticles depends on the cell-nanoparticle interactions and utilization of the nanoparticle by the cell. If nanoparticles enter the cell, it may have the potential to alter the cellular functions which may lead to increased toxicity. For example, as the size of the nanoparticle decreases, nanotoxicity may increase (Sharifi et al., 2012). Moreover, nanoparticles that have a larger contact area (such as rod-shaped or fiber-like nanoparticles) are not able to get into the cells as easily as their globular shape counterparts which may decrease their toxicity (Sharifi et al., 2012). Furthermore, the

surface properties of nanoparticles alter the cells' biological response. Usually, it is thought that cationic surfaces are more toxic than anionic surfaces (Sharifi et al., 2012). Additionally, the coating material may alter the reactivity of the nanoparticle, hence, the biological response (Sharifi et al., 2012). Up to date, the main driving force of nanoparticle-mediated cytotoxicity is accepted as oxidative stress and inflammation. However, internalized nanoparticle through endocytic pathways is usually translocated to lysosomes inside the cells. Therefore, autophagy and lysosomal dysfunction may also be potential mechanisms behind nanotoxicity (Stern et al., 2012).

Cells may respond differently to distinct types of nanomaterials. These biological responses may be related to the toxicity as well as they may contribute to the proliferation of the cells. It has been shown that the cell viability of SaOS-2 cells that were exposed to methotrexate nanohybrids has been decreased in a dose-dependent manner (Choi et al., 2008) Another study proposes that SiO_2-Gentamicin nanohybrids are also toxic to SaOS-2 cells and toxicity is dose-dependent (He et al., 2018). On contrast, another osteosarcoma cell line, U2OS cells that have been treated with hydroxyapatite NPs showed greater cell viability (Cai et al., 2007). Additionally, SaOS-2 cells grown on HAp surface demonstrated increased cell viability compared to tissue culture plastic (Baxter et al., 2009).

It is evident that the biological response of SaOS-2 cells to various types of nanomaterials differs. In particular, HAp may induce the cell viability rate of SaOS-2 cells according to the literature. HAp is widely used in medical application as a hard tissue replacement material due to its similarity to the inorganic part of the human bone and teeth. The increase in the viability of osteoblast cells, SaOS-2, can be explained by this phenomenon.

CHAPTER 3

EXPERIMENTAL METHODOLOGY

3.1. Nanomaterials

Hydroxyapatite ($Ca_5(OH)(PO_4)_3$) and tricalcium phosphate ($Ca_3(PO_4)_2$) are biocompatible and osteoconductive biomaterials (Bordea et al., 2020). Their nanoforms have been widely used in research covering bone repair, substitution, and augmentation (Rey et al., 2017; Meirelles et al., 2008). Both nanomaterials are calcium phosphate derivatives (Rey et al., 2017). The Ca/P ratio of HAp is approximately 1.67 whereas TCP displays around 1.5 Ca/P ratio (Rey et al., 2017). Crystalline forms of HAp and TCP differ. HAp is an apatite calcium phosphate which is the most abundant crystalline structure found in all mineralized tissues of mammals (Rey et al., 2017). By contrast, TCP has two main crystalline phases: α-TCP and β-TCP. α-TCP is a highly unstable and high-temperature variety of TCP whereas β-TCP is the most widely encountered crystalline phase (Rey et al., 2017). Together with apatite, TCP crystalline phases are the most widely used calcium phosphate biomaterials due to being their bioresorbable nature (Rey et al., 2017). HAp (Sigma-Aldrich, 677418) with >97% purity and TCP hydrate (Sigma-Aldrich, 693898) synthetic nanopowders were used in the experiments.

3.2. Nanomaterial Characterization

Characterizations of HAp and TCP nanomaterials were done via FTIR, XRD, EDX, BET, and TGA analyses for the verification of commercial HAp and TCP characteristics. BET analyses of HAp and TCP nanopowders were conducted for surface area and porosity via N_2 gas absorption under 77^oK with a surface area analyzer device (Micromeritics, Gemini V). FTIR analyses of HAp and TCP nanopowders were performed by FTIR spectrophotometer (Perkin Elmer, Spectrum Two FT-IR Spectrometer). Transmission scanning was done between 400-4000 cm^{-1} spectrum. The X-ray diffraction method was performed to analyze the crystal structure of HAp and TCP.

X-ray diffractometer possessing copper Kα beams, (Philips, X'Pert Pro) equipped with a copper X-ray tube was used to collect data between 10-80^o 2θ with 0,1^o resolution. EDX analysis of HAp and TCP nanopowders was done with a scanning electron microscope (FEI, Quanta™ 250 FEG) with 15 kV working voltage, using an EDX detector (via Oxford Instruments, Aztec software). Elements with less than 1% (both atomic % and weight %) were excluded from the results. Weight loss of HAp and TCP nanopowders was analyzed via TGA/DTA instrument (Perkin Elmer, Diamond). Samples were analyzed between 25-800^{o}C with 10^{o}C/minute heating under N_2 atmosphere.

3.3. Design of Experiment

DoE part consists of two categories: screening design and response surface design. For both nanomaterials, the Plackett-Burman design was used in the screening design whereas the central composite design was followed as the response surface design. Both DoEs were conducted via DX7 software. Initially, potential parameters that are effective on dispersion were determined based on a literature survey. Then, PBD was conducted to screen the parameters. Based on the chosen parameters from PBD that are contributing to the dispersion, CCD was performed. Z-average (intensity weighted mean hydrodynamic size) and zeta potential response values were measured with a DLS instrument (Malvern Panalytical, Nano-ZS Zetasizer). Particle size was measured via a DLS instrument with a detector located at 173^o via collected scattered light. 1 mL of stock sample was used for the analyses and measurements were done at room temperature. Refractive indexes for HAp and TCP were set as 1.65 and 1.63 respectively whilst the absorption value for both nanomaterials was 0.01. All measurements were done as triplicates. Models for HAp and TCP were developed from CCD Z-average and zeta potential responses and validated with eight parameter sets represented in Table 4.10. and Table 4.11.

3.3.1. Plackett-Burman Design

Six parameters were chosen as a first step for the screening design and a 12-run PBD was performed with six parameters and five dummy variables. These parameters are concentration of the nanomaterial, application of pre-wetting, presence of the additive, sonication type, pH, and type of dispersion medium. Amongst these parameters,

minimum and maximum values for concentration is 1 mg/mL and 5 mg/mL whereas 5 and 10 for pH, respectively. For pre-wetting, 99.9% ethanol was used to make a paste of nanopowders as the final volume of ethanol was 0.05% (v/v) after the corresponding dispersion medium was added. For additive, 0.05% (w/v) BSA in UPW or PBS was used, depending on the dispersion medium parameter. The preparation of BSA solutions is represented in Appendix B. As sonication, two types were used utilizing bath sonicator (Bandelin, Sonorex Digiplus) and probe sonicator (Bandelin, Sonopuls HD 2200.2 with KE76 probe). Sonication amplitude and sonication time for both bath and probe sonicators were determined based on the literature survey and outcomes of the findings represented in Appendix A. For bath sonication: amplitude and time were determined as 100% and 15 minutes respectively whereas 10% amplitude and 2 minutes were used for probe sonication. In addition, two types of dispersion medium: UPW and PBS (0.1M) were used. Minimum and maximum values for numerical variables (concentration and pH) and categorical indications for categorical variables (pre-wetting, additive, sonication type, dispersion medium) can be seen in Table 3.1 whereas PBD matrices for HAp and TCP are shown in Table 4.3. and Table 4.5. respectively.

Table 3.1. Plackett-Burman Design matrix.

Parameter	**Minimum/Categorical Value**	**Maximum/Categorical Value**
Concentration	1 mg/mL	5 mg/mL
Pre-wetting	No	Yes
Additive	No	Yes
Sonication Type	Bath	Probe
pH	5	10
Dispersion Medium	UPW	PBS

3.3.2. Central Composite Design

CCD was used to evaluate the synergetic effect of three efficient contributing parameters of dispersion determined by PBD: concentration, pH, and presence of the additive. Samples were not pre-wetted priorly, dispersed in UPW via bath sonication with the same settings from PBD experiments. 26 data points with 8 axial points, 10 factorial points, and 8 hybrid replicate points were analyzed via CCD for modeling and can be seen in Table 4.7. Developed models for both HAp and TCP Z-ave and zeta potential

values were verified via three internal and five external parameter sets as shown in Table 4.10. and Table 4.11. All measurements were done as triplicates.

3.4. Preparation and Characterization of Dispersion Samples

Two sets of parameters that are annotated as well-dispersed (WD) and aggregated (AGG) shown in Table 4.12. were determined via models generated by CCD for both HAp and TCP nanomaterials. For both nanomaterials, Z-average and zeta potential values of both parameter sets were evaluated and compared with the expected values from CCD models. Concordantly, SEM analysis was done to monitor the shape and size of the nanoparticles. The analyses were done within 5-15 kV working voltage via a scanning electron microscope (FEI, Quanta™ 250 FEG) equipped with backscattered electron and secondary electron detectors. 1/10 dilution of samples was prepared and 5 µl of the dispersed sample was dropped on SiO_2 wafer and let dry in an open atmosphere before analysis.

3.5. SaOS-2 Cell Culture

SaOS-2 (human bone osteosarcoma cells, ATCC HTB-85) cells were maintained to be used in cellular uptake and cell viability analyses. SaOS-2 cells were cultured in DMEM High Glucose (Sigma-Aldrich, D6429) medium supplemented with 10% FBS (Gibco™, 26140079) and 1% Penicillin/Streptomycin (Gibco™, 15140122) and incubated in a cell incubator in 37^{o}C and 5% CO_2 atmosphere. All materials were heated in a water bath set to 37^{o}C before cells were exposed. Initially, SaOS-2 cell stocks from the N_2 tank were thawed by dipping the cryovials in a 37^{o}C water bath as the caps of the cryovials were not inside the water. The 1 mL of the cell containing freezing medium was taken into a 15 mL falcon tube while it was still cold, and a 9 mL DMEM high glucose complete medium was added on top of it. The tube was centrifuged at 1000 RPM for 5 minutes and the supernatant was discarded to remove the DMSO (Sigma-Aldrich, D8418). Remained cell pellet was dissolved with DMEM high glucose complete medium and seeded into a 25 cm^2 cell culture flask. Cells were monitored periodically and transferred to a 75 cm^2 cell culture flask when they reached approximately 85-90% confluency. To reach the adequate cell number for the corresponding assays, SaOS-2 cells were either subcultured or frozen for making stocks for the proceeding applications. Cells

were subcultured when they reached approximately 85-90% confluency. The cells in a 75 cm^2 cell culture flask were treated with 2 mL of sterile PBS solution (Pan Biotech, P04-36500) thoroughly after the medium was discarded. Then the cells were treated with 2 mL of trypsin (Gibco™, 25200-056) for detachment and incubated for 5 minutes at 37°C and 5% CO_2. Cells were observed after incubation and transferred to a 15 mL falcon tube if they detached from the flask. 8 mL DMEM high glucose complete medium was added on top, and the tube was centrifuged with 1000 RPM for 5 minutes and the supernatant was discarded to remove trypsin. Then cell pellet was either dissolved with DMEM high glucose complete medium for the subculturing or freezing medium containing 90% DMEM high glucose complete medium and 10% DMSO for storage. For subculturing, dissolved cells were shared to the desired number of 75 cm^2 cell culture flasks and the volume of the flasks was completed to 10 mL and incubated in 37°C and 5% CO_2 for cells to grow. To stock the cells, 1 mL of freezing medium was transferred to cryovials and put at -20°C for a day. After a day, cryovials were transferred to either -80°C or the N_2 tank. To be used in analyses, cells were harvested when they reached approximately 85-90% confluency and viable cells were counted with a hemocytometer. 5 x 10^3 cells/well were seeded into a 96-well plate for WST-1 cell viability assay.

3.6. Cell Viability Assay by WST-1

WST-1 assay (Sigma-Aldrich, 11644807001) was used to assess the cell viability of SaOS-2 cells. Cell viability evaluation of WST-1 assay is based on the production of dark red formazan dye from slightly red tetrazolium salt by metabolically active cells. Cultured SaOS-2 cells were kept between 1-10 passage numbers for WST-1 assay. 5 x 10^3 cells/well were subcultured to 96-well plates and incubated for 24 hours under 37°C and 5% CO_2 atmosphere. Cells were then treated with either previously prepared WD or AGG samples of either HAp or TCP with four different concentrations diluted with 0.05% (w/v) BSA from their corresponding stock dispersion: 50 µg/mL, 100 µg/mL, 200 µg/mL, and 300 µg/mL. Untreated cells were used as controls. Cells were incubated under 37°C and %5 CO_2 conditions for either 6 hours or 24 hours after treatment. Incubated cells were treated with 10 µl of WST-1 solution and incubated for 3 hours under 37°C and 5% CO_2 environment. After incubation, 450 nm (WST-1 formazan wavelength) and 630 nm (background wavelength) absorbance values were measured as triplicates with a

spectrophotometer (Thermo Scientific, Multiskan Sky) and data were collected. 630 nm absorbance values of each sample were subtracted from 450 nm absorbance values and absorbance versus nanomaterial concentration graphs were plotted.

CHAPTER 4

RESULTS AND DISCUSSION

4.1. Characterization of Ceramic Nanomaterials

Characterization of physicochemical properties of HAp and TCP was performed for the evaluation of commercial nanopowders. FTIR spectroscopy was utilized to assess the bond formation of nanomaterials for the determination of present functional groups and comparison of obtained transmission peaks with those of HAp and TCP peaks in the literature.

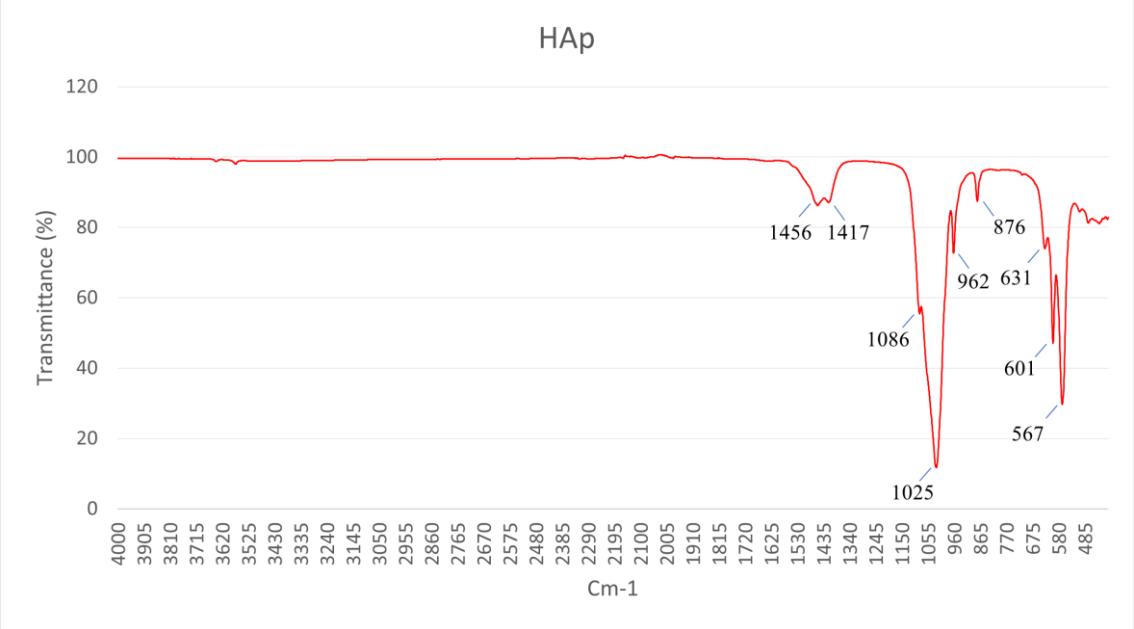

Figure 4.1. FTIR spectra of HAp.

For HAp, bands occurring at 567 cm^{-1}, 601 cm^{-1}, and 631 cm^{-1} indicates phosphate ν_4 vibrations. 876 cm^{-1} band represents carbonate ν_2 vibration and 962 cm^{-1} band shows phosphate ν_1 symmetric stretch vibration. Strong bands at 1025 cm^{-1} and 1086 cm^{-1} are referring to phosphate ν_3 vibration whereas bands that occurred at 1417 cm^{-1} and 1456 cm^{-1} show ν_3 vibrations of surface carbonate groups. FTIR spectra bands for TCP had similar characteristic peaks to HAp, referring same functional groups for the given band

range, except bands occurred at 1400-1460 cm^{-1} spectrum. FTIR spectra of characterized HAp and TCP have been found to correlate with the FTIR spectra of HAp and TCP available in the literature (Rehman & Bonfield, 1997).

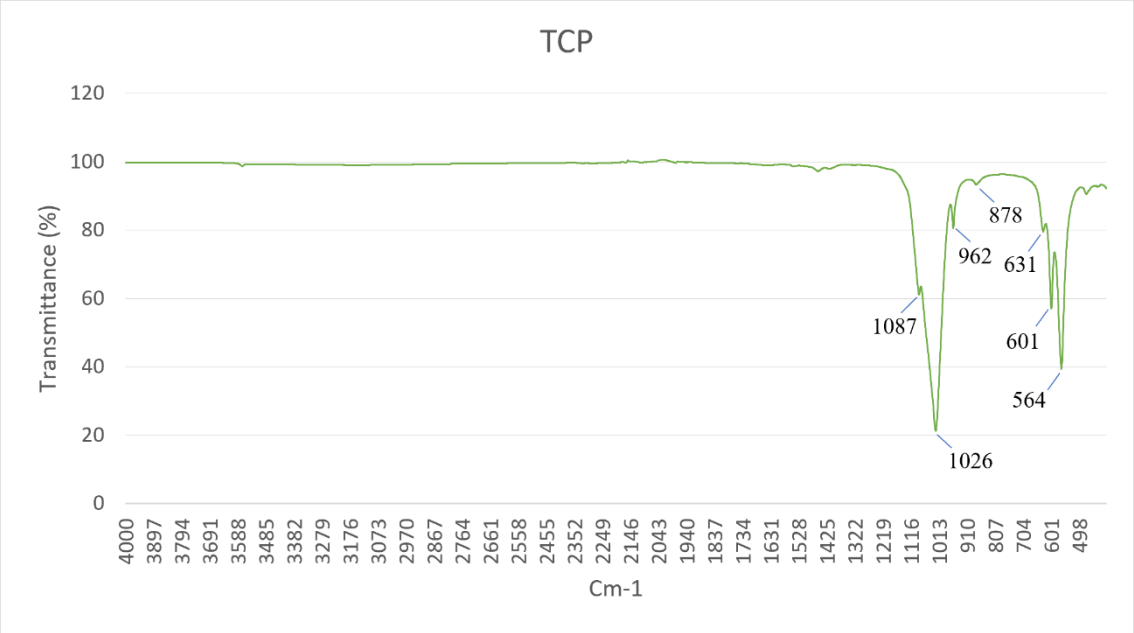

Figure 4.2. FTIR spectra of TCP.

XRD analyses have been conducted to evaluate crystal structures of commercial HAp and TCP. XRD graph of HAp can be seen in Figure 4.3. whereas TCP XRD graph is shown in Figure 4.4. Obtained data were compared with International Centre for Diffraction Data (ICDD, formerly known as Joint Committee on Powder Diffraction Standards) database (JCPDS no. 09-0432 for HAp and JCPDS no. 09-0169 for β-TCP). It has been found that HAp and TCP have correlated characteristic XRD peaks with ICDD data. In particular, commercial TCP possesses HAp-like XRD peaks between 30^{o}-35^{o} bands showing that TCP resembles of HAp in terms of its crystal structure.

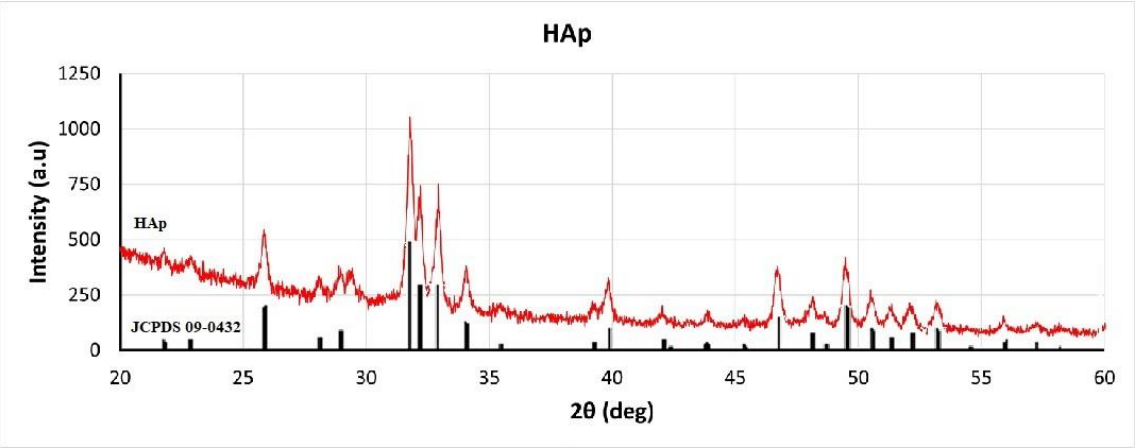

Figure 4.3. XRD peaks of HAp compared to ICDD HAp peaks (JCPDS 09-0432).

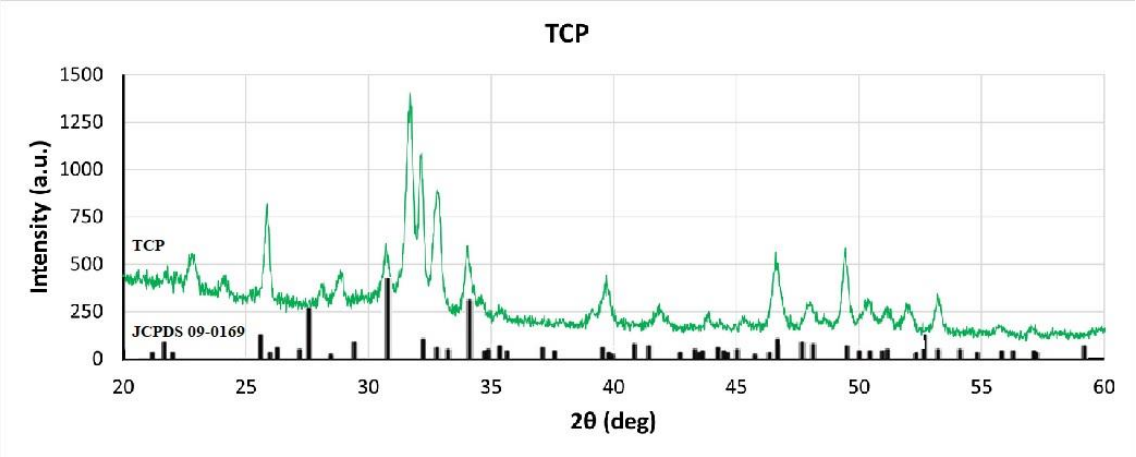

Figure 4.4. XRD peaks of TCP compared to ICDD β-TCP peaks (JCPDS 09-0169).

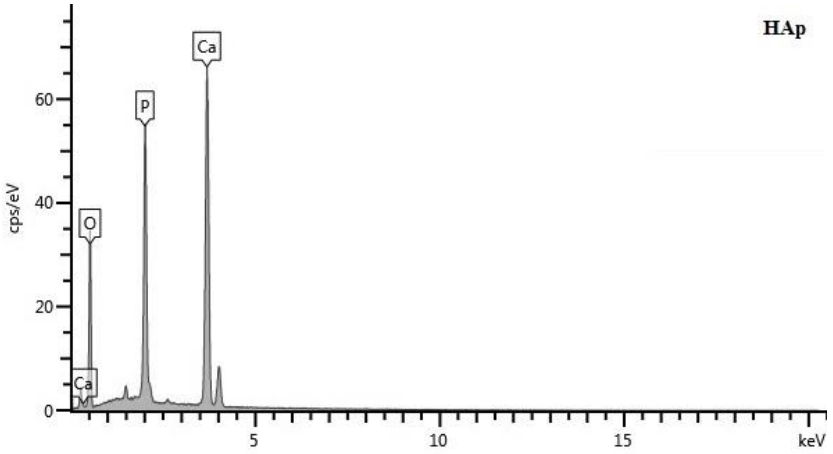

Figure 4.5. Intensities of elements in HAp measured via EDX.

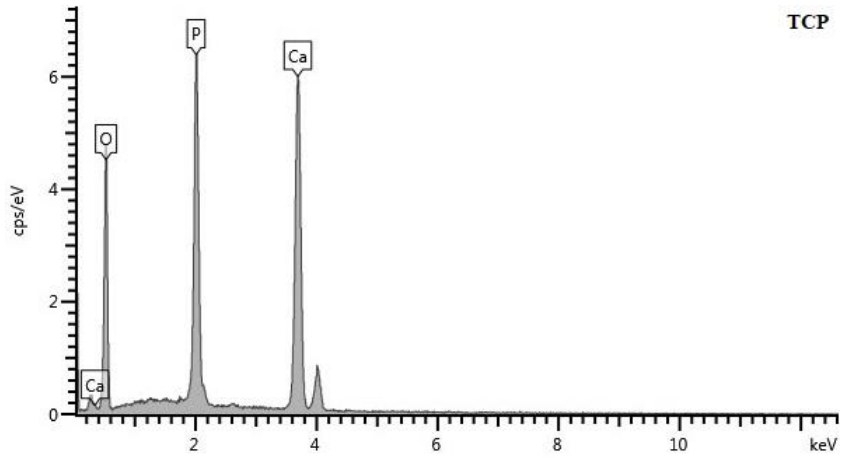

Figure 4.6. Intensities of elements in TCP measured via EDX.

EDX analyses were performed to determine the elemental content of the commercial samples. Ca/P ratio of HAp was found to be 1.86 whereas the ratio for TCP is 1.49 according to EDX results. Although stoichiometric Ca/P ratios of HAp and TCP are 1.67 and 1.5 respectively, the results obtained via EDX analyses are within the acceptable range for both nanomaterials (Abifarin et al., 2019; Mansur et al., 2005). Intensities of elemental constituents of HAp and TCP can be seen in Figure 4.5. and Figure 4.6. and Ca/P ratios with Ca, O, and P percentages are shown in Table 4.1.

Table 4.1. Elemental composition of HAp and TCP.

Element or Ratio	Atomic % in HAp	Atomic % in TCP
O	64.55	68.87
P	12.38	12.55
Ca	23.07	18.58
Ca/P	1.86	1.49

Single point surface area, BET surface area, Langmuir surface area, pore volume, and pore size properties measured via BET analyses can be seen in Table 4.2. Measured BET surface areas of HAp and TCP are 31.3 and 36.5 m^2/g, respectively. BET surface area value of HAp is 2.33-fold higher than of commercial product's specification sheet value (~9.4) whereas no information was provided by the supplier for TCP. BET results indicate that TCP has a higher surface area than HAp whereas HAp has a more porous structure. Pore volume and size of HAp may indicate increased bioavailability due to the accessibility of the nanomaterial, especially in calcified structures.

Table 4.2. Surface properties of HAp and TCP obtained via BET analyses.

	HAp	**TCP**
Single Point Surface Area (m^2/g)	30.7	35.8
BET Surface Area (m^2/g)	31.3	36.5
Langmuir Surface Area (m^2/g)	49.1	57.1
Pore Volume (cm^3/g)	1.8	0.8
Pore Size (Å)	2357	883

Changes in weight percentages of the HAp and TCP due to temperature increase were measured with TGA/DTA instrument and the results were shown in Figure 4.7. and Figure 4.8. Weight loss percentages for HAp and TCP were 2.1% and 1% respectively. It has been observed that both nanomaterials lost approximately 1-2% weight between 400°C and 600°C and have relatively high thermal stability.

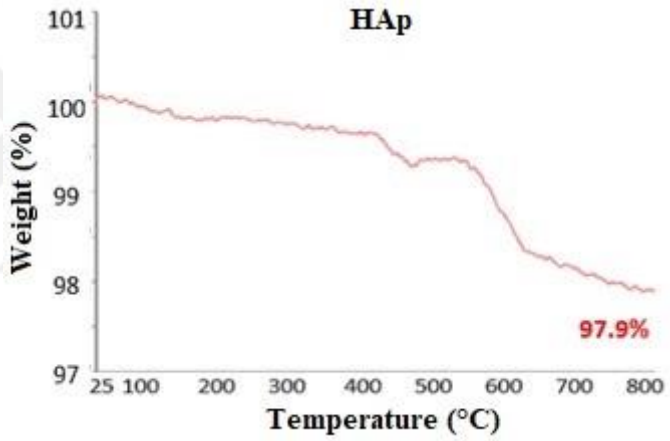

Figure 4.7. TGA spectrum of HAp nanopowders.

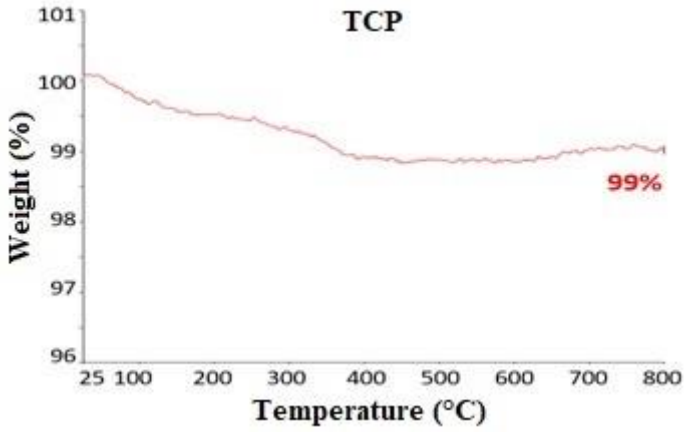

Figure 4.8. TGA spectrum of TCP nanopowders.

4.2. Design of Experiment Derived Dispersion Conditions

Assessment of the effectiveness of the selected parameters on dispersion efficiency was determined via a two-step statistical approach: PBD and consequently, CCD. Obtained responses of Z-average and zeta potential via PBD matrix with minimum and maximum values, together with categorical variables can be seen in Table 4.3. for HAp.

Table 4.3. Plackett-Burman design matrix and measured response values of HAp.

Run Number	Concentration (mg/mL)	Prewetting	Additive	Sonication Type	pH	Dispersion Medium	Z Ave (nm)	Zeta (mV)
1	5	Yes	No	Bath	5	PBS	3324	+10
2	5	No	No	Probe	5	UPW	3350	+15
3	5	Yes	No	Bath	10	UPW	8823	+10
4	1	Yes	No	Probe	10	PBS	2742	-7
5	5	Yes	Yes	Probe	10	UPW	1868	-9
6	1	No	No	Bath	5	UPW	3584	0
7	5	No	Yes	Probe	5	PBS	3141	0
8	1	Yes	Yes	Bath	5	PBS	315	-8
9	1	No	No	Probe	10	PBS	4852	-14
10	1	No	Yes	Bath	10	UPW	272	-17
11	1	Yes	Yes	Probe	5	UPW	197	-12
12	5	No	Yes	Bath	10	PBS	3976	-1

The contribution of the parameters used in PBD to Z-average and zeta potential for HAp can be seen in Table 4.4. Concentration with %30.39, additive with %42.3, and pH with 5.61% contributions cover the total contribution of 78.3% for Z-average response whereas these three parameters contribute 49.56%, 26.77%, and 13.3% respectively with 89.63% total to zeta potential response for HAp. Three parameters, pH together with concentration and additive were selected for the CCD experiments for HAp.

Table 4.4. % Contribution of parameters in Plackett-Burman design of HAp. Cont: contribution, C: concentration, P: pre-wetting, A: additive, S: sonication type, DM: dispersion medium. D1, D2, D3, D4, D5: dummy factors. * represents statistically significant values.

		C	P	A	S	pH	DM	D1	D2	D3	D4	D5
Z ave	**Cont (%)**	30.39	4.48	42.30	0.06	5.61	3.76	4.94	0.07	0.88	0.66	6.84
	***p* Value**	0.02*	0.25	0.01*	0.88	0.21	0.29	-	-	-	-	-
Zeta	**Cont (%)**	49.56	0.01	26.77	3.17	13.3	0.35	1.22	1.22	2.6	1.22	0.58
	***p* Value**	0.002*	0.94	0.007*	0.19	0.03*	0.63	-	-	-	-	-

PBD matrix and measured response values of TCP can be seen in Table 4.5. Consecutively, contributions of the most effective parameters in PBD for TCP are shown in Table 4.6. Like PBD results of HAp, concentration with 38.43% and additive with 42.14% were two prominent parameters for Z-average response. Concentration, additive, and pH with the respective contributions of 7.85%, 40%, and 42.2% and a total contribution of 90.05% have a significant effect on zeta potential. Although the effect of pH on Z-average was not significant for TCP, consideration of the effect of pH on surface charge regulation and consistency of pH with zeta potential were evaluated and concentration, additive, and pH parameters were selected to proceed with CCD experiments. Despite the sonication parameter having a significant contribution to zeta potential, it was excluded from the CCD experiments for the integrity and correlation with the Z-average evaluations and experimental setup creation.

Table 4.5. Plackett-Burman design matrix and measured response values of TCP.

Run Number	Concentration (mg/mL)	Prewetting	Additive	Sonication Type	pH	Dispersion Medium	Z Ave (nm)	Zeta (mV)
1	5	Yes	No	Bath	5	PBS	3567	+4.6
2	5	No	No	Probe	5	UPW	8075	+1.9
3	5	Yes	No	Bath	10	UPW	4043	0
4	1	Yes	No	Probe	10	PBS	2114	-9
5	5	Yes	Yes	Probe	10	UPW	2368	-11.1
6	1	No	No	Bath	5	UPW	3036	+3.76
7	5	No	Yes	Probe	5	PBS	2518	-5.3
8	1	Yes	Yes	Bath	5	PBS	520	-5.7
9	1	No	No	Probe	10	PBS	3371	-8.4
10	1	No	Yes	Bath	10	UPW	288.9	-13.9
11	1	Yes	Yes	Probe	5	UPW	224	-5.8
12	5	No	Yes	Bath	10	PBS	3008	-9.55

Table 4.6. % Contribution of parameters in Plackett-Burman design of TCP. Cont: contribution, C: concentration, P: pre-wetting, A: additive, S: sonication type, DM: dispersion medium. D1, D2, D3, D4, D5: dummy factors. * represents statistically significant values.

		C	P	A	S	pH	DM	D1	D2	D3	D4	D5
Z ave	**Cont (%)**	38.43	5.71	42.14	1.12	0.43	2.16	0.03	0.0001	0.39	6.16	3.44
	***p* Value**	0.007*	0.15	0.006*	0.49	0.66	0.35	-	-	-	-	-
Zeta	**Cont (%)**	7.85	0.41	40	5.85	42.20	1.38	0.92	0.24	0.62	0.02	0.51
	***p* Value**	0.009*	0.39	0.0002*	0.02*	0.0002*	0.14	-	-	-	-	-

CCD matrices for HAp and TCP were created based on the selected parameters from PBD experiments. Concentration, additive, and pH parameters were selected for both HAp and TCP, and CCD matrix was created as shown in Table 4.7. together with experimental responses.

Table 4.7. Central composite design matrix and response values of HAp and TCP.

Run Number	Concentration (mg/mL)	Additive	pH	HAp Z Ave (nm)	HAp Zeta (mV)	TCP Z Ave (nm)	TCP Zeta (mV)
1	3	No	7.5	3192	8.4	2821.5	+0.284
2	3	No	3.96	3480	7.4	3913	+8.72
3	3	Yes	7.5	772.8	-9.1	451.8	-9.71
4	3	Yes	75	1222	-9.7	296.4	-10.8
5	3	No	7.5	4717	0.4	4162.5	-1.65
6	1	Yes	10	258.4	-14.8	215.7	-21
7	3	Yes	7.5	446.7	-11	564.7	-7.76
8	5	Yes	5	2087	-3	2494.7	-5.21
9	3	No	7.5	2746	14.3	4210	-0.7
10	1	Yes	5	344.7	-8.5	214.2	-7.13
11	3	No	7.5	2426.5	8.7	2954.3	-1.38
12	5.83	Yes	7.5	2398	-7.4	254.9	-9.01
13	5	No	5	3419	0.8	1937	-0.13
14	0.17	No	7.5	1323	2.05	1183	+0.21
15	0.17	Yes	7.5	209	-10.4	205.6	-10.9
16	3	Yes	7.5	946.6	-5.8	266.5	-13.9
17	3	No	7.5	6438	-15	3822.5	-5.62
18	5	No	10	3468	6.61	4024	-2.23
19	1	No	10	7452	5.7	2961	-2.09
20	3	No	11.04	3228	12.1	4325	-8.78
21	3	Yes	11.04	728.3	-10	207.8	-23.6
22	1	No	5	2203	-0.888	3183.3	+4.61
23	5.83	No	7.5	5846	-15.5	NA	-0.52
24	5	Yes	10	584.3	-8.1	358.34	-16.3
25	3	Yes	3.96	1663	-0.2	876.6	-0.47
26	3	Yes	7.5	1604	-5.1	257.6	-11.1

A reduced quadratic model equation for both Z-average and zeta potential responses of HAp (Equation 4.1. and Equation 4.2.) and two-factor interaction model for Z-average response of TCP (Equation 4.3.) with a reduced quadratic model equation for zeta potential response of TCP (Equation 4.4.) were provided via CCD analyses where A represents concentration (mg/mL), B represents pH, and C represents additive for all HAp and TCP Z-average and zeta potential equations.

$$\text{HAp Log10(Z-ave)} = +3.25 + 0.18A - 0.043B + 0.3C - 0.12AB - 0.15AC + 0.1BC - 0.093A^2 \quad (4.1)$$

$$\text{HAp Zeta Potential} = +0.015 + 1.39A - 0.64B + 6.99C + 0.16AB - 0.72AC + 3.02BC - 1.97A^2 + 0.17B^2 \quad (4.2)$$

$$\text{TCP Log10(Z-ave)} = +3.05 + 0.18A - 0.086B + 0.44C - 0.062AB - 0.1AC + 0.13BC \quad (4.3)$$

$$\text{TCP Zeta Potential} = -5.94 + 0.21A - 5.7B + 5.29C + 0.92AB - 0.95AC + 1.51BC - 0.12B^2 \quad (4.4)$$

Z-average values of 17th and 23rd runs of HAp and 5th, 12th, and 23rd runs of TCP were not included in corresponding analyses because of inconsistent outliers and non-available measured values. ANOVA was conducted to analyze the models. The probability values that are associated with the F values for all four models were found significant and this indicates that models are efficient in terms of prediction of Z-average and zeta potential for corresponding models. F values of HAp Z-average, HAp zeta potential, TCP Z-average, and TCP zeta potential models are 16.51, 18.63, 28.97, and 31.92 respectively whereas the *p* values of all four models were < 0.0001 and significant. Corresponding R^2 values indicating a correlation between coefficients of HAp Z-average, HAp zeta potential, TCP Z-average, and TCP zeta potential are 0.8784, 0.8976, 0.9157, and 0.9254 respectively. R^2 values for model prediction of corresponding responses of HAp Z-average, HAp zeta potential, TCP Z-average, and TCP zeta potential are 0.7029, 0.7756, 0.7405, and 0.8230 respectively. Additional information such as the significance of individual terms and lack of fit of ANOVA tests for the corresponding models can be seen in Table 4.8. and Table 4.9.

Surface curvature graphs of HAp and TCP Z-average models can be seen in Figure 4.9. and 4.10. respectively. The observed shape is planar-like with a slight curvature for both nanomaterials with and without BSA graphs. It has been seen that the presence of BSA has a significant effect on the Z-average value. An observation has been made that the increase in the concentration of nanoparticles whilst pH decreases cause the Z-average value to be higher. This phenomenon is clearer in the presence of BSA for both nanomaterials.

The graphs of surface curvatures for the zeta potential models of HAp and TCP are shown in Figure 4.11. and Figure 4.12. respectively. The shapes for the surface curvatures are planar-like with a saddle-like resemblance to HAp zeta potential model with and without BSA graphs. As in Z-average model surface curvature graphs, BSA is significant in terms of affecting the zeta potential values. It has been shown that the increasing nanoparticle concentration with a decrease in the pH value results in a lower magnitude of the zeta potential values. This outcome is correlated with the Z-average surface curvatures since the electrostatic stability of the nanoparticles is expected to increase with the increase in the magnitude of the zeta potential value. Thus, the lower zeta potential value may refer to the increasing aggregation behavior of the nanoparticles. This difference in the zeta potential values is more visible for both nanomaterials in the presence of BSA.

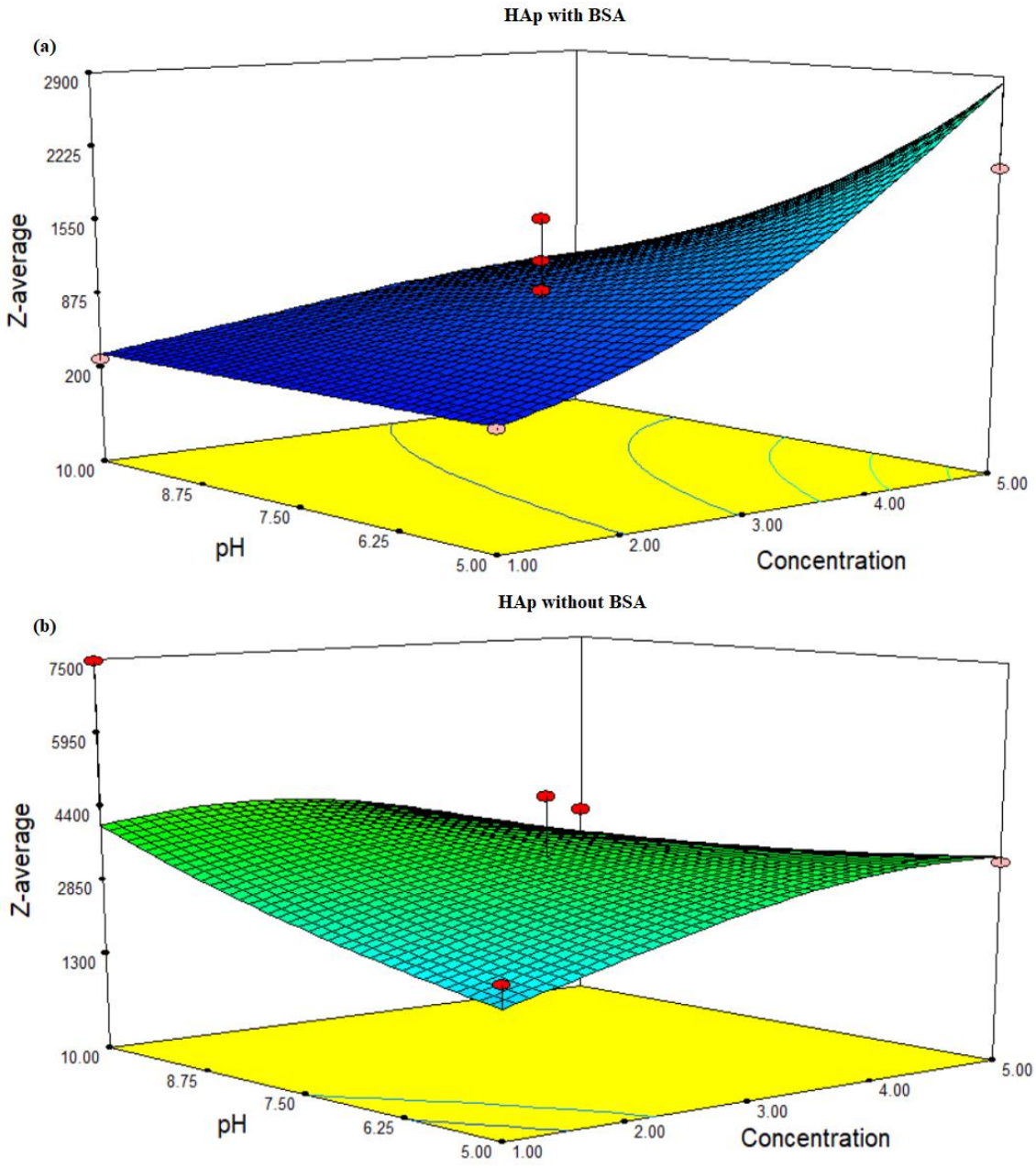

Figure 4.9. Surface curvature graphs of HAp Z-average model. (a) with BSA. (b) without BSA.

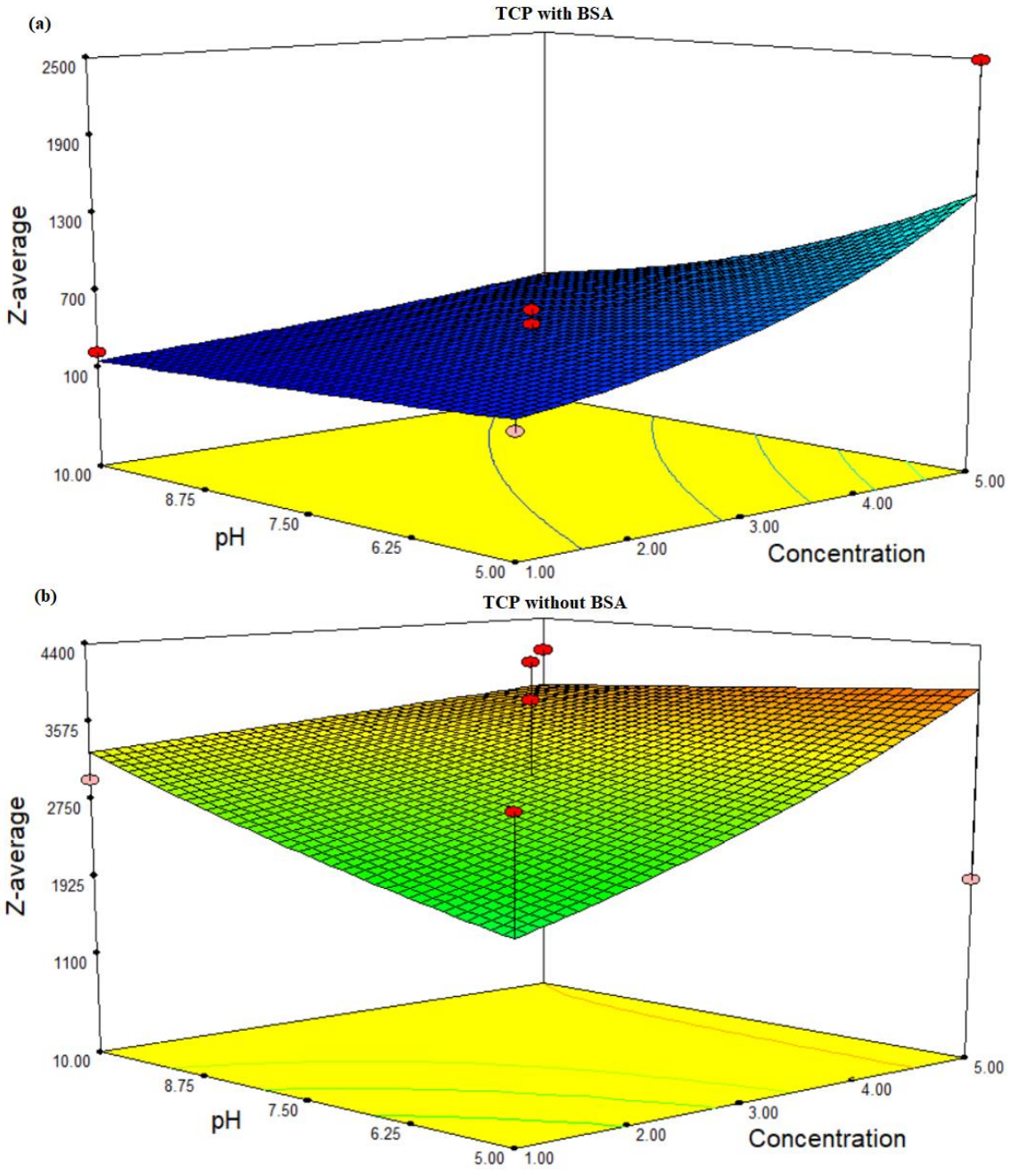

Figure 4.10. Surface curvature graphs of TCP Z-average model. (a) with BSA. (b) without BSA.

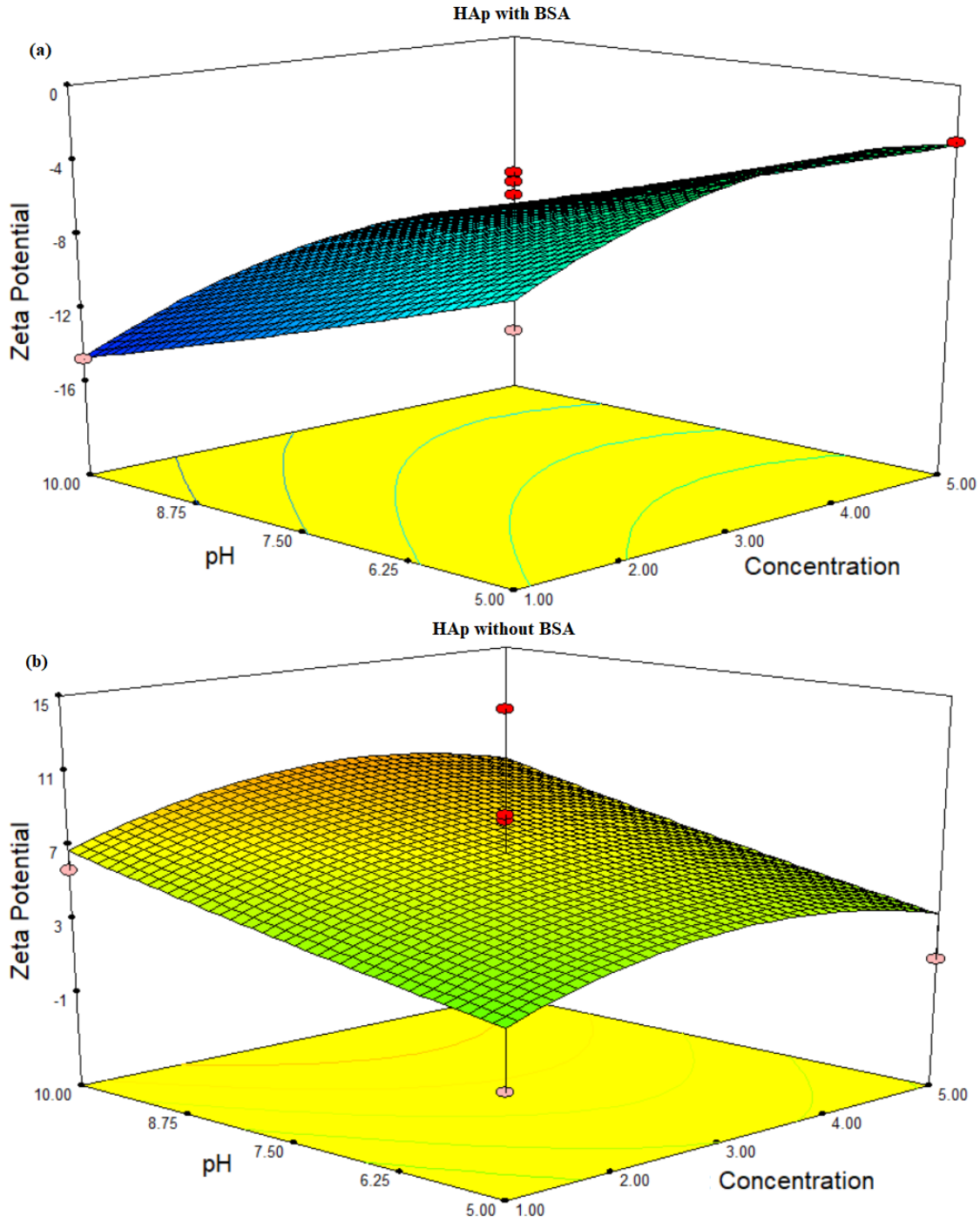

Figure 4.11. Surface curvature graphs of HAp zeta potential model. (a) with BSA. (b) without BSA.

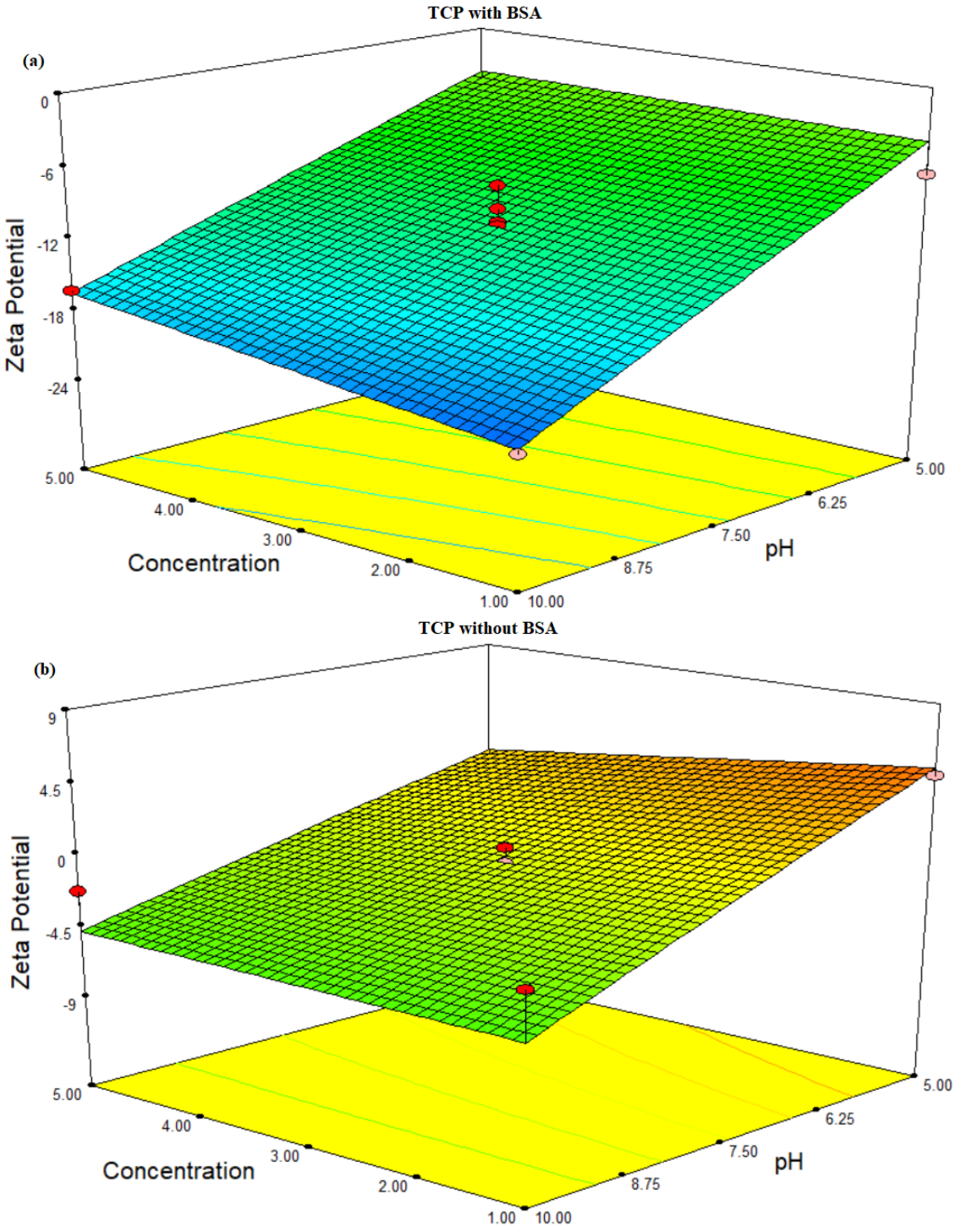

Figure 4.12. Surface curvature graphs of TCP zeta potential model. (a) with BSA. (b) without BSA.

Table 4.8. ANOVA for HAp Z-average and Zeta Potential Models. A: Concentration, B: pH, C: Additive.

Model	Source	Sum of Squares	df	Mean Square	F Value	$p > F$	Significance
HAp Z-average Model	Model	3.47	7	0.50	16.51	< 0.0001	significant
	A	0.43	1	0.43	14.28	0.0016	
	B	0.030	1	0.030	1.01	0.3303	
	C	2.10	1	2.10	69.83	< 0.0001	
	AB	0.11	1	0.11	3.76	0.0702	
	AC	0.28	1	0.28	9.43	0.0073	
	BC	0.18	1	0.18	5.84	0.0280	
	A^2	0.095	1	0.095	3.18	0.0936	
	Residual	0.48	16	0.030			
	Lack of Fit	0.26	9	0.028	0.88	0.5793	not significant
	Pure Error	0.22	7	0.032			
	Cor. Total	3.95	23	3.95	23	3.95	
	R^2				0.8976	0.8784	
	Adjusted R^2				0.8494	0.8252	
	Predicted R^2				0.7756	0.7029	
	Adeq. Precision				12.742	13.378	
HAp Zeta Potential Model	Model	1712.26	8	214.03	18.63	< 0.0001	significant
	A	25.25	1	25.25	2.20	0.1565	
	B	7.44	1	7.44	0.65	0.4320	
	C	1173.34	1	1173.34	102.14	< 0.0001	
	AB	0.21	1	0.21	0.019	0.8931	
	AC	6.70	1	6.70	0.58	0.4556	
	BC	166.68	1	166.68	14.51	0.0014	
	A^2	43.02	1	43.02	3.74	0.0698	
	B^2	0.63	1	0.63	0.055	0.8179	
	Residual	195.29	17	11.49			
	Lack of Fit	70.82	9	7.87	0.51	0.8351	not significant
	Pure Error	124.47	8	15.56			
	Cor. Total	1907.55	25				
	R^2					0.8976	
	Adjusted R^2					0.8494	
	Predicted R^2					0.7756	
	Adeq. Precision					12.742	

Table 4.9. ANOVA for TCP Z-average and Zeta Potential Models. A: Concentration, B: pH, C: Additive.

Model	Source	Sum of Squares	df	Mean Square	F Value	*p* > F	Significance
TCP Z-average Model	Model	1306.96	7	186.71	31.92	< 0.0001	significant
	A	0.72	1	0.72	0.12	0.7307	
	B	520.06	1	520.06	88.91	< 0.0001	
	C	728.38	1	728.38	124.53	< 0.0001	
	AB	6.81	1	6.81	1.16	0.2949	
	AC	14.45	1	14.45	2.47	0.1334	
	BC	36.37	1	36.37	6.22	0.0226	
	B^2	0.19	1	0.19	0.032	0.8591	
	Residual	105.28	18	5.85			
	Lack of Fit	64.92	10	6.49	1.29	0.3677	not significant
	Pure Error	40.37	8	5.05			
	Cor. Total	1412.24	25				
	R^2					0.9254	
	Adjusted R^2					0.8965	
	Predicted R^2					0.8230	
	Adeq. Precision					19.941	
TCP Zeta Potential Model	Model	5.64	6	0.94	28.97	< 0.0001	significant
	A	0.40	1	0.40	12.24	0.0030	
	B	0.12	1	0.12	3.65	0.0742	
	C	4.35	1	4.35	134.02	< 0.0001	
	AB	0.031	1	0.031	0.95	0.3441	
	AC	0.12	1	0.12	3.56	0.0775	
	BC	0.27	1	0.27	8.26	0.0110	
	Residual	0.52	16	0.032			
	Lack of Fit	0.41	9	0.045	2.77	0.0966	not significant
	Pure Error	0.11	7	0.016			
	Cor. Total	6.16	22				
	R^2					0.9157	
	Adjusted R^2					0.8841	
	Predicted R^2					0.7405	
	Adeq. Precision					14.336	

Validation experiments were performed for the developed models by choosing three internal and five external parameter sets in-range values of the parameters. All eight results of the validation experiments for the Z-average models for both HAp and TCP nanomaterials were within the 95% confidence interval range of the models and valid as shown in Table 4.10. For the zeta potential model validation experiments, six out of eight experiment results were in range of 95% confidence intervals and valid for the HAp zeta potential model whereas five of eight experiment results were determined as valid according to the measured values as represented in Table 4.11. For both HAp and TCP zeta potential models, invalid parameter sets did not have a BSA additive. This may be the result of biased model generation for the zeta potential because of the non-uniform dispersion of nanomaterials in the absence of BSA. Unpredictive particle aggregates with various sizes may result in differences in zeta potential values with high deviations and this may result in diverse zeta potential values for the local suspension areas. This bias may also affect the accuracy of the zeta potential model samples without BSA presence. Additionally, the low and high values of 95% confidence intervals have been observed to be more diverse when the additive is not present in the sample. The prominent reason for this gap is polydispersity and the model's prediction of a wide-range of values, especially for Z-average response.

Table 4.10. Validation experiment results of HAp Z-average and TCP Z-average models. The prediction was considered valid if the measured value is in-range of low and high values of %95 confidence interval.

NM	No	Concentration (mg/mL)	Additive	pH	Measured Z-ave (nm)	Predicted Z-ave (nm)	95% CI Low	95% CI High	Prediction
HAp	1	1	Yes	10	469.6	316.159	177,57	562.91	Valid
	2	1.27	No	9.82	2698.75	4024.98	2249,334	7202.021	Valid
	3	3.94	Yes	10	584	761.549	490,26	1182.96	Valid
	4	5	No	10	4790	2723.794	1395,309	5317.140	Valid
	5	1.65	Yes	7.7	424.8	479.694	350,58	656.36	Valid
	6	2.95	Yes	6.42	781.4	1011.8	741.8	1379.76	Valid
	7	4.24	No	8.72	3426	3394.2	2263.8	5090.46	Valid
	8	3	No	7.5	4608	3547.84	2658.58	4734.56	Valid
TCP	1	1	Yes	10	281.8	260.9	173.96	391.28	Valid
	2	1.27	No	9.82	3130.3	2877.65	1794.93	4613.48	Valid
	3	3.94	Yes	10	315.4	336.51	214.14	528.81	Valid
	4	5	No	10	3678.3	4176.81	2347.47	7431.74	Valid
	5	1.65	Yes	7.7	291.8	251.09	181.63	347.11	Valid
	6	2.95	Yes	6.42	631.3	495.30	371.6	660.19	Valid
	7	4.24	No	8.72	3452.5	3683.57	2451.83	5534.10	Valid
	8	3	No	7.5	3454.3	3343.66	2426.87	4606.77	Valid

Table 4.11. Validation experiment results of HAp zeta potential and TCP zeta potential models. The prediction was considered valid if the measured value is in-range of low and high values of %95 confidence interval.

NM	No	Concentration (mg/mL)	Additive	pH	Measured Zeta (mV)	Predicted Zeta (mV)	95% CI Low	95% CI High	Prediction
HAp	1	1	Yes	10	-16.9	-14.71	-18.97	-10.45	Valid
	2	1.27	No	9.82	5.77	7.17	2.81	11.53	Valid
	3	3.94	Yes	10	-10.67	-9.83	-13.04	-6.62	Valid
	4	5	No	10	1.3	8.41	2.76	14.06	Invalid
	5	1.65	Yes	7.7	-10.11	-9.60	-12.51	-6.68	Valid
	6	2.95	Yes	6.42	-6.15	-5.41	-8.13	-2.70	Valid
	7	4.24	No	8.72	5.44	7.91	4.39	11.43	Valid
	8	3	No	7.5	11.97	7	4.24	9.76	Invalid
TCP	1	1	Yes	10	-17.1	-20.64	-24.09	-17.1	Valid
	2	1.27	No	9.82	-6.05	-4.74	-7.80	-1.67	Valid
	3	3.94	Yes	10	-16.6	-17.57	-20.20	-14.94	Valid
	4	5	No	10	0.55	-4.77	-8.22	-1.31	Invalid
	5	1.65	Yes	7.7	-9.78	-12.64	-14.68	-10.60	Invalid
	6	2.95	Yes	6.42	-7.72	-8.15	-9.86	-6.44	Valid
	7	4.24	No	8.72	-7.36	-2.90	-5.03	-0.76	Invalid
	8	3	No	7.5	0.82	-0.64	-2.28	0.99	Valid

Two sets of parameters were determined for both HAp and TCP according to the models obtained via DoE methods. Z-average and zeta potential values of well-dispersed HAp (HAp-WD), aggregated HAp (HAp-AGG), well-dispersed TCP (TCP-WD), and aggregated TCP (TCP-AGG) samples shown in Table 4.12. and Table 4.13. were compared with predicted Z-average and zeta potential values of the corresponding models.

Table 4.12. Z-average measured and predicted values of selected well-dispersed and aggregated sample sets for HAp and TCP.

Sample	Concentration (mg/mL)	Additive	pH	Measured Z-ave (nm)	Predicted Z-ave (nm)	95% CI Low	95% CI High
HAp-WD	2	Yes	10	336.6	472.9	303.15	737.7
HAp-AGG	4	Yes	6.5	1654	1499.4	1086.3	2069.1
TCP-WD	2.5	Yes	10	278.6	217.7	144.3	328.6
TCP-AGG	5	Yes	7.5	595.6	781.8	483.9	1263

Table 4.13. Zeta potential measured and predicted values of selected well-dispersed and aggregated sample sets for HAp and TCP.

Sample	Concentration (mg/mL)	Additive	pH	Measured Zeta (mV)	Predicted Zeta (mV)	95% CI Low	95% CI High
HAp-WD	2	Yes	10	-14.9	-12.09	-15.05	-9.13
HAp-AGG	4	Yes	6.5	-6.49	-4.95	-7.77	-2.14
TCP-WD	2.5	Yes	10	-13.8	-19.07	-21.50	-16.65
TCP-AGG	5	Yes	7.5	-7.46	-10.07	-12.50	-7.64

Parameter sets were determined based on the subsequent cell viability experiments. Cells were treated with various concentrations of nanoparticles ranging from 50 µg/mL to 300 µg/mL in cell viability experiments, hence, stock concentrations of well-dispersed and aggregated samples were set considering the dilution factor that was applied and treatment conditions. The stock sample that was added to cell media was not exceeded 20% of the total volume to prevent the cells from osmotic stress. Although it was possible to achieve a Z-average value of 316.16 nm, the HAp-WD parameter set that yielded Z-average value of 472.91 nm was selected to have appropriate stock concentration value for the subsequent experiments.

The pH values of the samples were determined considering the biological relevance and the extreme values of the models for both HAp and TCP. Since the optimum growth pH for the SaOS-2 cells is neutral pH, it was considered that the pH of the surrounding environment did not change drastically during the treatment process. Additionally, although the Z-average value can be further decreased via increasing the pH, the extreme values and optimum growth pH were taken into account and the pH values of samples were determined accordingly.

It was seen that the BSA presence contributes significantly to the dispersion stability. Nanoparticles have a strong tendency to aggregate without BSA and this potential aggregation behavior is unpredictable since polydispersity indexes of the samples without BSA vary in a wide range. BSA is present in FBS which is used in the cell culture experiments and it is one of the highly encountered proteins in the protein corona structure covering the nanoparticle surface. The use of BSA as an additive during the dispersion process may contribute to the early protein corona formation via the BSA-nanoparticle interaction. This interaction may lead to the attachment of other proteins available in the surrounding environment by providing a docking point on the nanoparticle's surface. Furthermore, BSA-nanoparticle interaction is governed by solvent-accessible amino acid residues of BSA and their surface characteristics. Therefore, the content and charges of interacting amino acids on the surface of BSA define this interaction. It has been observed that solvent-accessible amino acid residues of BSA is rich in alanine, glutamic acid, aspartic acid, lysine, and leucine (Table D.1.). The importance of alanine, glutamic acid, and lysine on the adsorption of proteins on the surface of calcium phosphate derivative compounds has been reported in the literature (Kresak et al., 1977; Duanis-Assaf et al., 2022). Moreover, changes in the concentration of BSA and pH of the surrounding environment may further affect BSA-nanoparticle interaction (Zhu et al., 2006). BSA concentration has been found to affect Z-average values of nanoparticle dispersions in a fluctuating pattern (Figure D.1.). Furthermore, BSA has an isoelectric point between pH 4.5-4.8 at room temperature (Raghuwanshi et al., 2020). Above this pH, the overall charge of BSA is negative as shown in Figure D.3. This overall charge is mainly governed by the solvent accessible surface of BSA in which alanine, glutamic acid, aspartic acid, lysine, and leucine are the prevalent amino acids. When pH of the surrounding environment is between 5 to 10, charges of those amino acids change based on their isoelectric points (Table D.1.). Considering both HAp and TCP have a point of zero charge pH values approximately at neutral pH, electrostatic

interaction of nanoparticles and BSA on neutral pH can be maintained by lysine amino acids (isoelectric point of lysine is 9.47) on the surface of BSA. It must be pointed out that conformation and local charges of side chains of surface amino acids change between pH 5-10. However, steric interactions may also complement the BSA-nanoparticle interaction, maintaining a surface-coating-like relationship between BSA and nanoparticles.

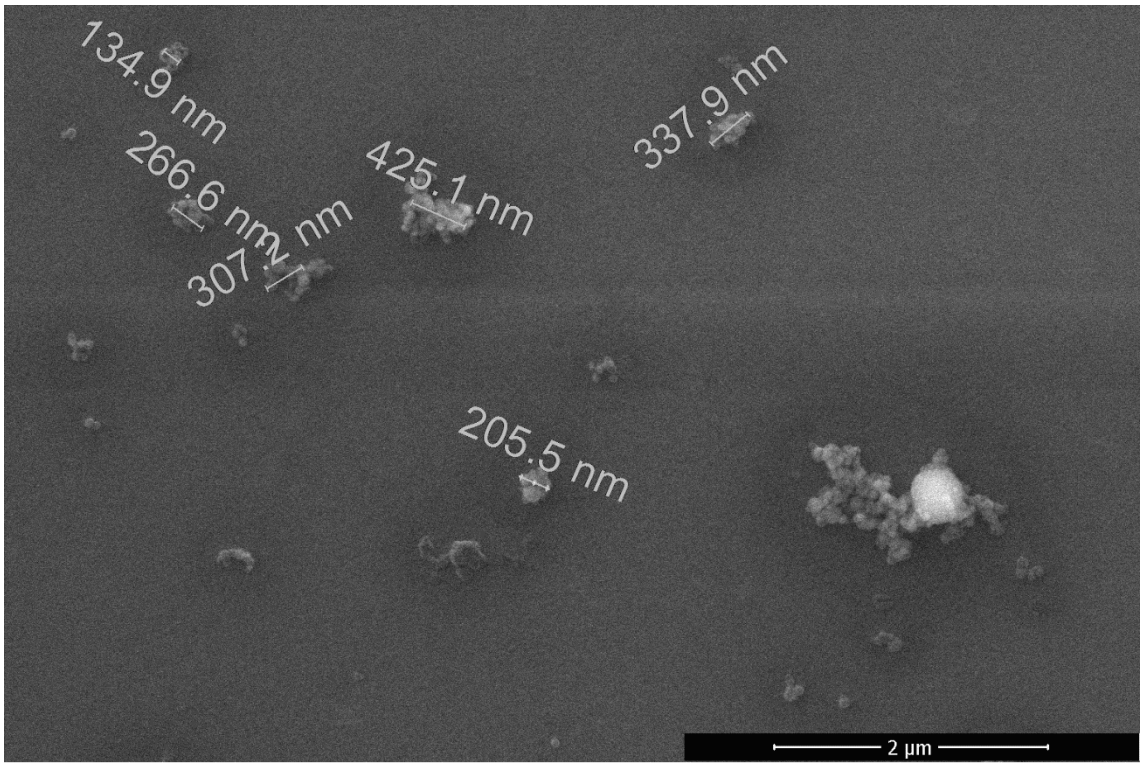

Figure 4.13. SEM image of HAp-WD.

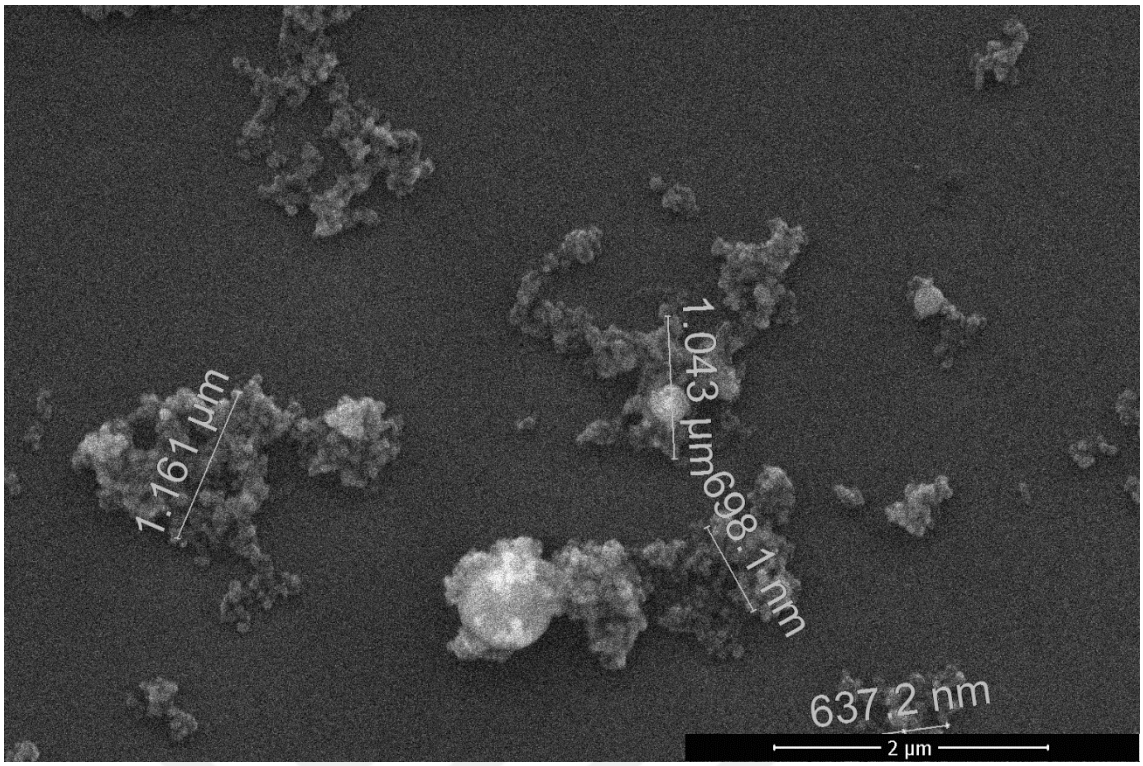

Figure 4.14. SEM image of HAp-AGG.

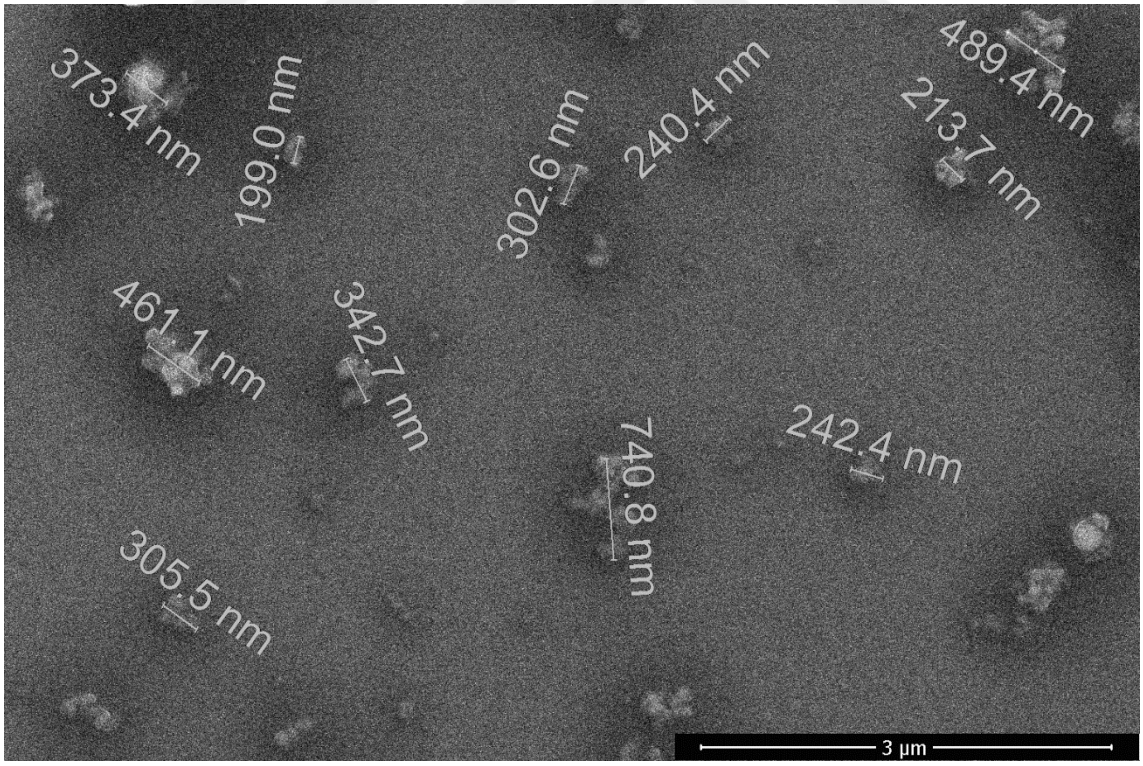

Figure 4.15. SEM image of TCP-WD.

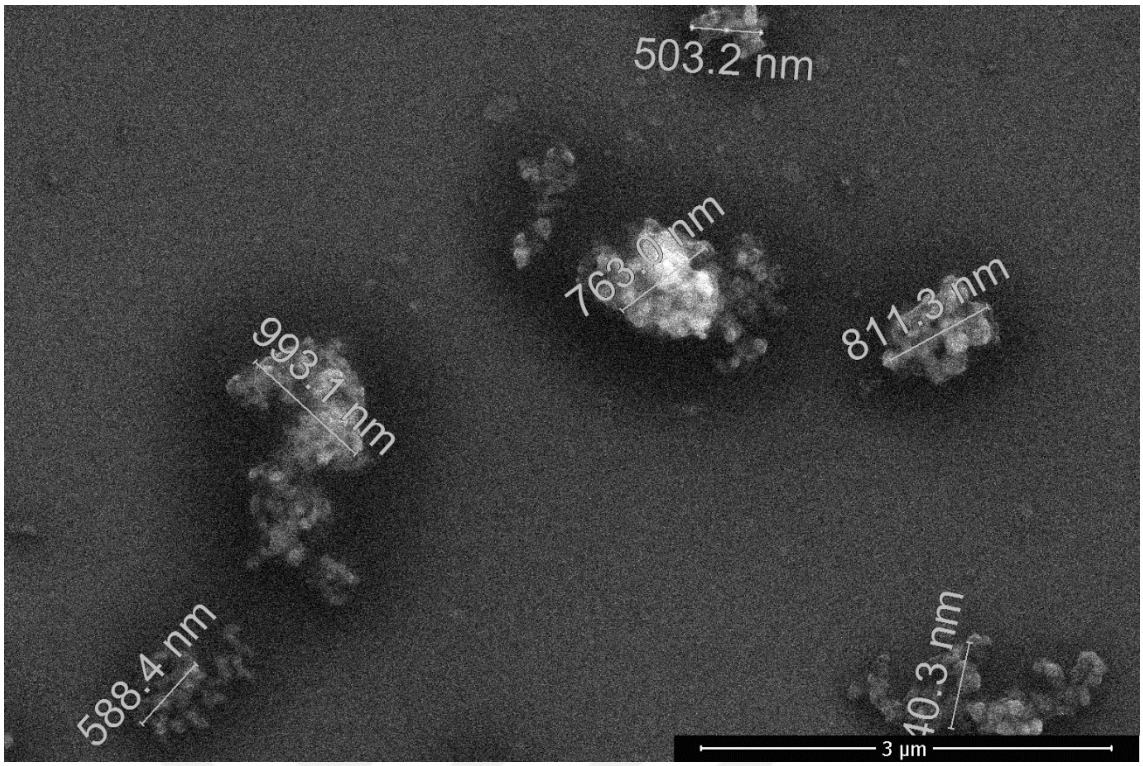

Figure 4.16. SEM image of TCP-AGG.

Hydrodynamic size distribution of HAp-WD, HAp-AGG, TCP-WD, and TCP-AGG can be seen in Figure 4.17., Figure 4.18., Figure 4.19., and Figure 4.20., respectively. Undesired small peaks were observed for samples except for HAp-WD. The band ranges of the peaks show that the nanoparticle dispersion is not completely uniform. Furthermore, it was also seen in the SEM results (Figure 4.13., Figure 4.14., Figure 4.15., and Figure 4.16.) that samples have relatively diverse aggregated shapes and sizes. However, predicted values by corresponding Z-average models show that these various-sized aggregates are within 95% confidence intervals. Although models provide such information, the achieved nanoparticle size interpreted as Z-average is not as same as the individual nanoparticle size. According to SEM images, individual nanoparticles can be distinguished as spherical shaped for both HAp and TCP and their sizes range between 50-80 nm for HAp and 40-75 nm for TCP (Figure E.1.).

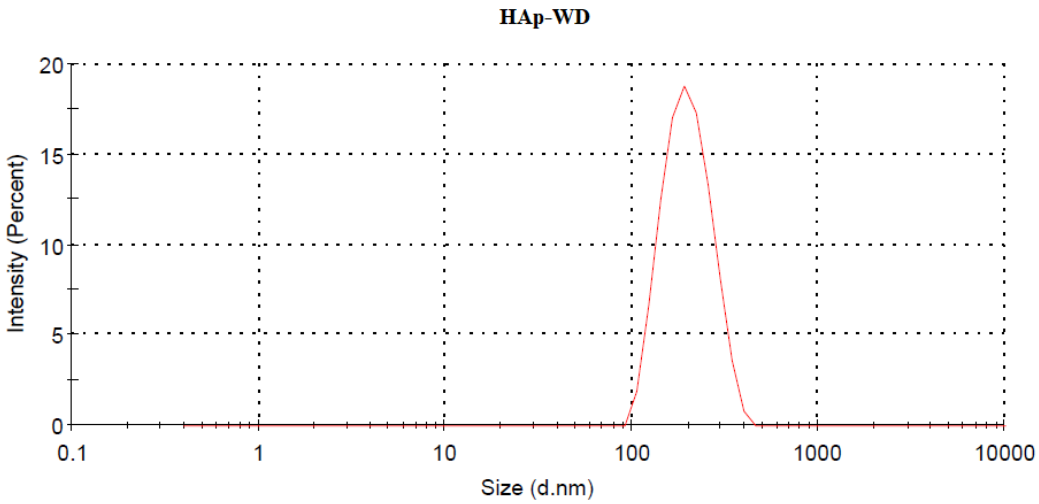

Figure 4.17. Hydrodynamic size distribution of HAp-WD.

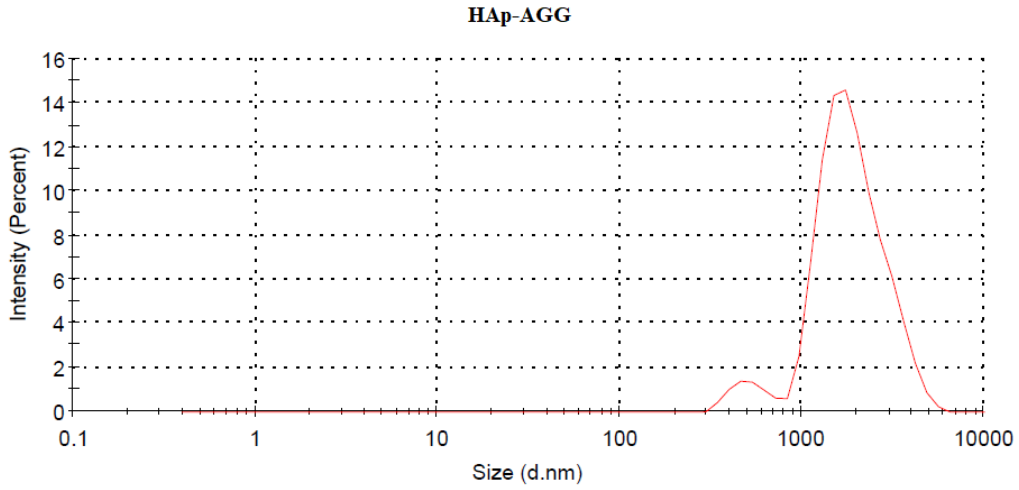

Figure 4.18. Hydrodynamic size distribution of HAp-AGG.

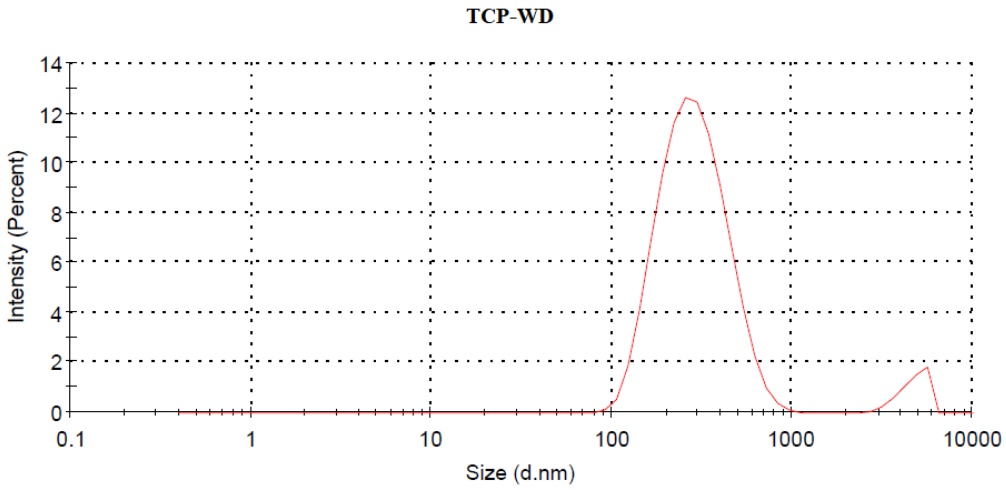

Figure 4.19. Hydrodynamic size distribution of TCP-WD.

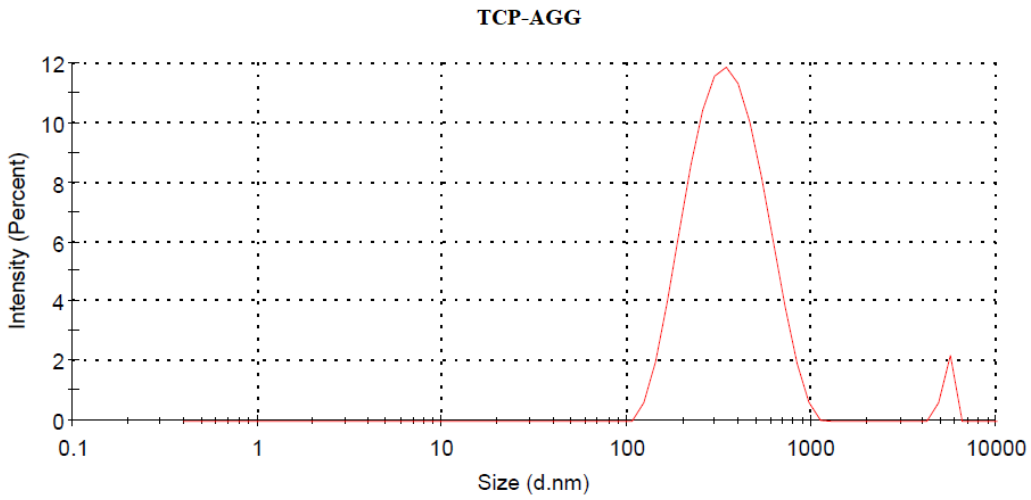

Figure 4.20. Hydrodynamic size distribution of TCP-AGG.

Zeta potential distribution of HAp-WD, HAp-AGG, TCP-WD, and TCP-AGG can be seen in Figure 4.21., Figure 4.22., Figure 4.23., and Figure 4.24. respectively. The magnitude of zeta potential represents the electrostatic repulsion behavior of nanoparticles. In particular, the pH of the surrounding environment and the presence of BSA is expected to affect the zeta potential profile of the samples. For both samples, the magnitude of zeta potential values increase as the pH is further away from the isoelectric point of BSA (around pH 5). A magnitude of the zeta potential value that is higher than 30 mV is generally considered to have greater electrostatic stability (Hartmann et al., 2015). Dispersions are less stable for all samples according to the commonly accepted

electrostatic stability criteria. Despite moderate stability, dispersions can be used in subsequent experiments up to one week after preparation (Figure E.2.).

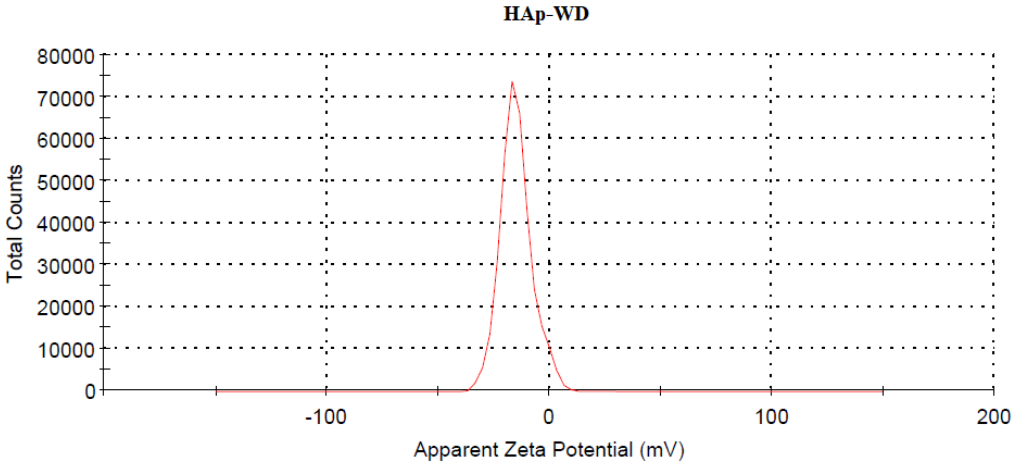

Figure 4.21. Zeta potential distribution of HAp-WD.

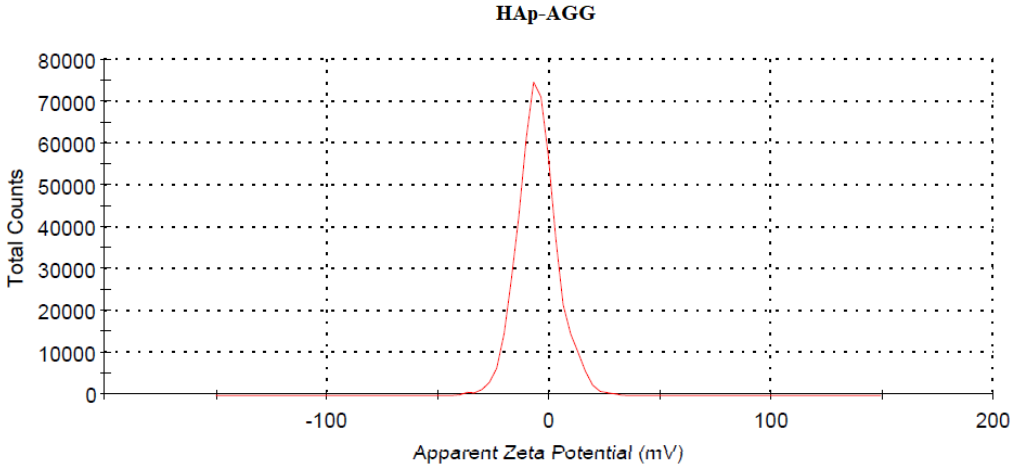

Figure 4.22. Zeta potential distribution of HAp-AGG.

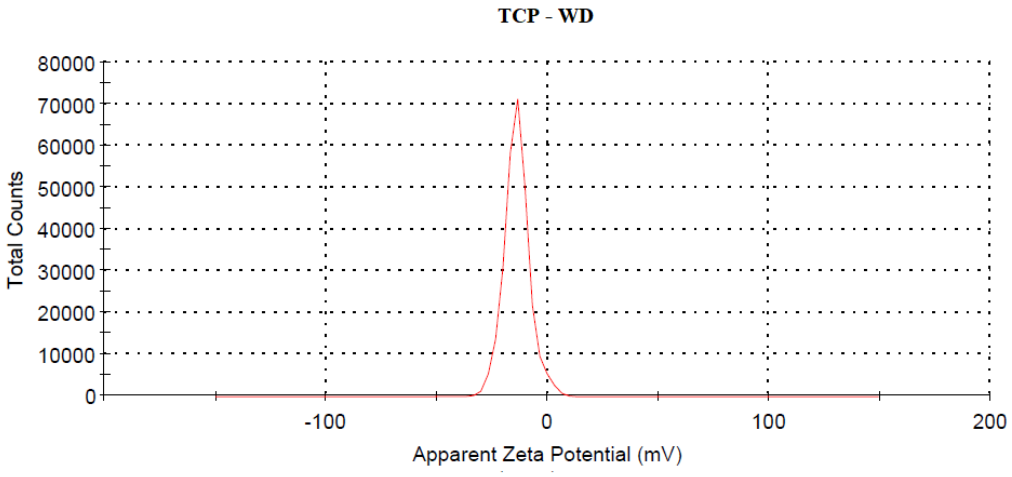

Figure 4.23. Zeta potential distribution of TCP-WD.

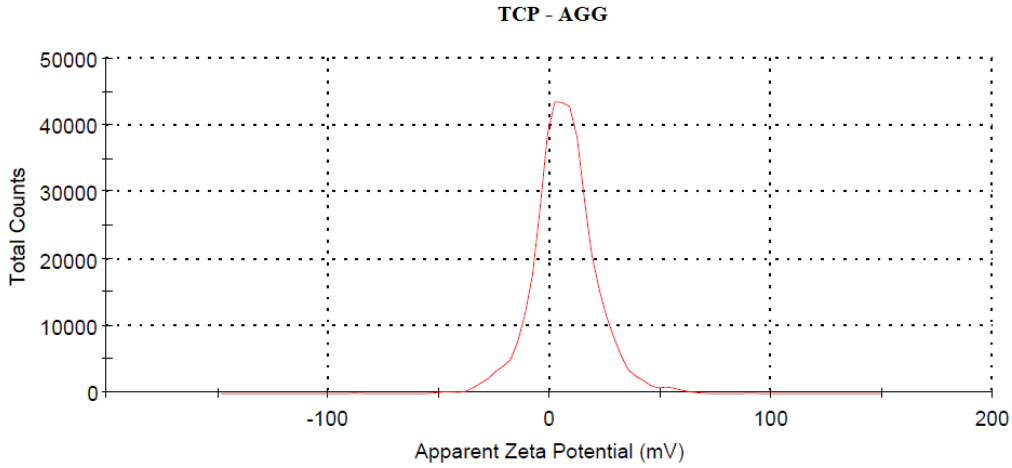

Figure 4.24. Zeta potential distribution of TCP-AGG.

4.3. Cell Viability Assessment of SaOS-2 Cells

Cell viability of SaOS-2 cells after nanoparticle treatment was compared with the untreated control. Both 6- and 24-hour HAp and TCP treated cell viability did not change as shown in Figure 4.25. and Figure 4.26., and no significant differences were observed between cells treated with various concentrations of HAp and TCP nanomaterials. Moreover, there was no significant difference between well-dispersed and aggregated samples of the corresponding nanoparticle samples.

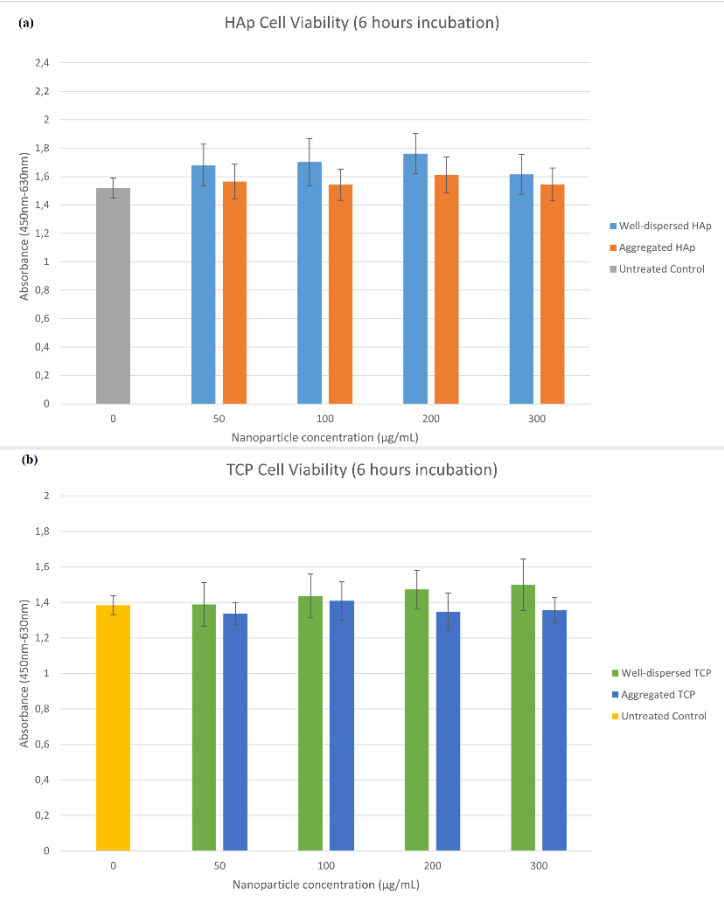

Figure 4.25. Viability results of SaOS-2 cells treated with increasing concentrations of (a) HAp. (b) TCP for 6 hours.

Although no significant difference in cell viability was observed for the investigated conditions, cellular uptake may change due to the changes in particle size and surface potential depending on the parameters used for dispersion. Nanoparticle internalization may occur via distinct pathways in cells, mainly through endocytosis (Yameen et al., 2014). However, the uptake mechanism may change as the nanoparticle aggregation causes the formation of various-sized aggregates since alternative ways such as phagocytosis would be a prevalent option when large-sized aggregates are present (Yameen et al., 2014). Therefore, uptake potential and internalized nanoparticle amount, which can be quantified with methods such as ICP-MS (Reifschneider et al., 2020) and Alizarin Red staining (Zhao et al., 2011), can show the bioavailability difference of nanoparticles with different sizes. Additionally, it was observed during the experiments that adhesion of cells to the cell culture plate was relatively stronger in cells treated with 200 µg/mL and 300 µg/mL of HAp and TCP compared to the cells treated with less concentrations. Therefore, another future perspective of the biological activity of HAp

and TCP can be the investigation of the nanoparticles' effect on SaOS-2 cells' adhesion behavior.

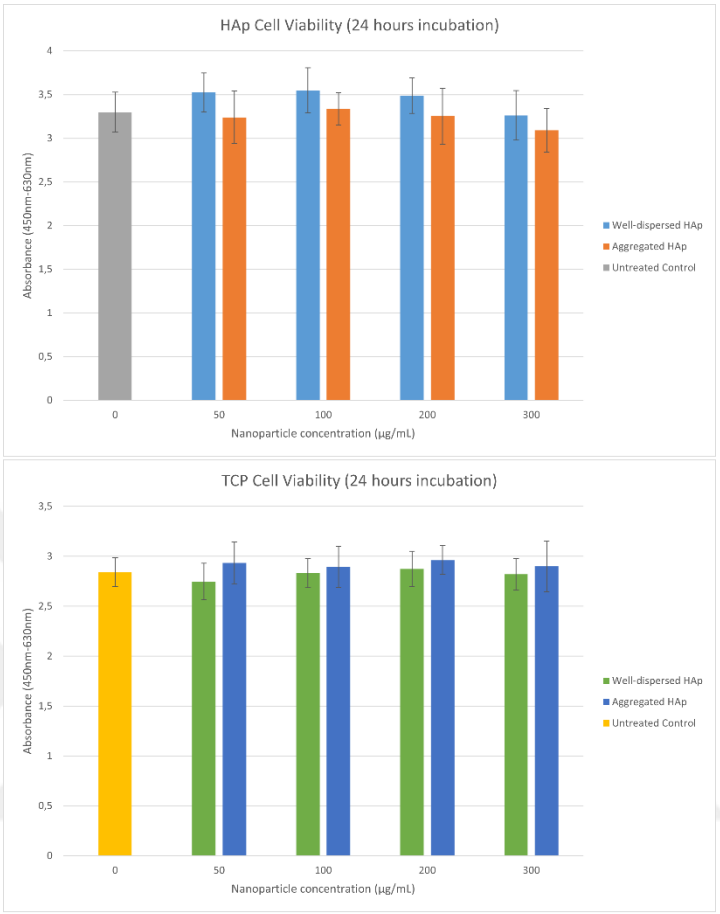

Figure 4.26. Viability results of SaOS-2 cells treated with increasing concentrations of (a) HAp. (b) TCP for 24 hours.

CHAPTER 5

CONCLUSION

Unique physicochemical properties of nanoparticles compared to their bulk counterparts have led to an ongoing increase in their manufacture and commercial use. In particular, the small size of nanoparticles enables them to move more freely throughout the body and interact more efficiently with macromolecules such as lipids and proteins, leading to their widespread use in therapeutics, diagnostics, imaging, drug delivery and dental applications. While there are various ways of classifying nanoparticles (e.g., based on their dimensionality, shape, composition, form, etc.), they are generally grouped into two basic categories: organic (polymeric, protein, or lipid-based) and inorganic (metallic and ceramic) nanoparticles. CeNPs that can be made up of oxides, carbides, phosphates, and metalloids such as calcium show excellent stability and biocompatibility with tissues, making them an excellent candidate for various biomedical applications. Their synthesis procedures often result in the formation of nano-powders which then need to be dispersed in a suitable medium before further use. The scope of this thesis is to develop dispersion protocols for two CeNPs that are commonly used in biomedical applications, HAp and TCP. DoE has been utilized to achieve the models that potentially predict the Z-average and zeta potential values measured via DLS for commercial HAp and TCP products.

HAp and TCP nanomaterials were characterized as-in received form and the results were compared with literature to verify the physicochemical characteristics of the nanomaterials. FTIR was conducted to analyze the bond formation and functional groups of nanomaterials. Crystal structures of nanomaterials were investigated via XRD. EDX analyses were done for elemental composition determination. Surface properties were analyzed with BET method. TGA was utilized to assess the thermal stability of nanomaterials. It was found that present FTIR bands referring to the functional groups were correlated with the literature for both nanomaterials. Crystal structure investigation revealed that HAp had its corresponding crystal structure whereas TCP possessed an apatite-like crystal structure instead of β-TCP. Ca/P ratios of nanomaterials were found within the acceptable range. BET analyses showed that HAp had a larger pore size and volume compared to TCP. The difference between pore size and volume may result in

changes in the bioavailability of these nanomaterials. Both nanomaterials were found thermally stable according to the TGA results.

Two models for each nanomaterial were developed via DoE after the characterization of the nanomaterials. DoE can be used to survey predetermined parameters to evaluate them for the generation of statistically relevant models. In this thesis, parameter pool and their value ranges were determined based on theoretical calculations of sonication parameters, literature review, and expert judgment. It was shown that amongst all selected parameters, concentration and additive (BSA) significantly contributed to the dispersion stability for all models for both nanomaterials. Although the pH of the surrounding environment was not found as a significant contributor to Z-average models, it was considered to be a critical parameter since it regulated the surface charge characteristics of materials in the dispersion environment. Amongst these three parameters, the presence of the additive molecule was the most prevalent parameter that altered the outcome of dispersion drastically. It was found that BSA stabilized the dispersion as the tendency of the nanoparticles to aggregate was greater without BSA. Moreover, DoE allowed evaluating the relationship between these parameters to develop an efficient model to predict Z-average and zeta potential values of HAp and TCP nanomaterials.

The synergetic effect of the three significant parameters is crucial for the aggregation and dispersion stability. Random motion of nanoparticles in the suspension is the main reason for the encounter and collision of individual nanoparticles. Therefore, increased concentration leads to an increase in the rate of encounters and interaction. The collision of nanoparticles may result in aggregation depending on their energy levels. Considering the importance of the electrostatic interactions for the repulsion between nanoparticles, concentration is linked to the pH as well. The pH of the surrounding environment affects the surface charge of the nanoparticles. In electrostatically unstable systems, increased concentration leads to the increased rate of aggregation due to the lack of efficient repulsion between nanoparticles. Besides its relationship with concentration, pH is also important for BSA-nanoparticle interactions. All molecules have a pH point where their overall charge is zero and the molecules must be charged in order to interact electrostatically with their surrounding environment. A pH level that is suitable for both BSA and nanoparticles facilitates their electrostatic interaction, thus improving the dispersion stability by regulating their surface charge profile. In particular, BSA has different conformational structures and surface charge profiles in different pH values.

This, combined with the changes in the surface of nanoparticles, governs the interaction between BSA and the nanoparticle. Therefore, a cross-linked connection of all three parameters directly contribute to the dispersion of nanoparticles.

As an outcome of the parameter evaluation, two different sample sets for each nanomaterial were prepared to investigate the effect of aggregation on biological activity. Based on the literature survey and findings, it was expected to observe an increase in the SaOS-2 cell viability, treated with different-sized nanoparticle samples. However, neither adverse nor proliferative effect on cell viability was observed. The reason could be the intrinsic properties of the nanomaterials and their effect on SaOS-2 cells. Therefore, these results cannot be generalized for different cell lines as well as the results may not be the same for SaOS-2 cells that are treated with other nanomaterial classes. Although the cell viability did not change, the aggregation behavior of nanoparticles may influence the uptake potential of SaOS-2 cells. Nanoparticles are mainly internalized by cells via endocytosis-related mechanisms. The route of nanoparticle uptake is regulated by its size and, thus, the rate of uptake may change when nanoparticle aggregate size changes. This could be further analyzed with methods such as ICP-MS, Alizarin Red staining, and flow cytometry to monitor and quantify the cellular uptake of nanoparticles.

It has been shown with this work that the characterization is important regardless of whether the nanomaterial is synthesized or acquired from a supplier. Physicochemical characteristics of nanomaterials provided by supplier may not be reliable (or even missing), hence, verification of the properties of the product is necessary. Another strength of this study is the leverage of DoE methods for optimizing nanoparticle dispersion. Without DoE, the workload of the study would have been quite intensive since there would be 480 data points (5 concentration, 6 pH, 2 additive, 2 pre-wetting, 2 sonication type, and 2 dispersion medium variables) for each nanomaterial. Instead of following a distinct combination of the variables for given parameters, the most efficient ones have been selected by combining DoE results with expert judgment. This combination has led to the explanation of the results from different perspectives. Moreover, leveraging DoE has been shown to be a promising tool to develop statistically significant models that can efficiently predict Z-average and zeta potential. Nonetheless, this study has several limitations. During the parameter screening, only BSA was included in the parameter set and only one concentration of BSA was evaluated. Other additive molecules that may potentially enhance the dispersion stability of HAp and TCP can be considered for future studies and different concentrations of these molecules can be

evaluated. Moreover, the temperature is an important factor in dispersion. However, it was not included in this study because of its hard maintenance and the local temperature changes inside the suspensions during applications such as sonication can be uncontrollable. Additionally, developed models to predict zeta potential for both nanomaterials have shown that they are biased to the presence of BSA, and their accuracy is lower when BSA is not present in the samples. Furthermore, this study is only valid for nano-sized bioceramic materials and needs to be validated for the other nanomaterial classes.

REFERENCES

Abifarin, J. K.; Obada, D. O.; Dauda, E. T.; Dodoo-Arhin, D. Experimental Data on the Characterization of Hydroxyapatite Synthesized from Biowastes. *Data in Brief* **2019**, *26*, 104485. https://doi.org/10.1016/j.dib.2019.104485.

Augustine, R.; Dalvi, Y. B.; Yadu Nath, V. K.; Varghese, R.; Raghuveeran, V.; Hasan, A.; Thomas, S.; Sandhyarani, N. Yttrium Oxide Nanoparticle Loaded Scaffolds with Enhanced Cell Adhesion and Vascularization for Tissue Engineering Applications. *Materials Science and Engineering: C* **2019**, *103*, 109801. https://doi.org/10.1016/j.msec.2019.109801.

Barnes, C. A.; Elsaesser, A.; Arkusz, J.; Smok, A.; Palus, J.; Leśniak, A.; Salvati, A.; Hanrahan, J. P.; Jong, W. H. de; Dziubałtowska, E.; Stępnik, M.; Rydzyński, K.; McKerr, G.; Lynch, I.; Dawson, K. A.; Howard, C. V. Reproducible Comet Assay of Amorphous Silica Nanoparticles Detects No Genotoxicity. *Nano Lett.* **2008**, *8* (9), 3069–3074. https://doi.org/10.1021/nl801661w.

Baxter, F.; Turner, I.; Bowen, C.; Gittings, J.; Chaudhuri, J. An in Vitro Study of Electrically Active Hydroxyapatite-Barium Titanate Ceramics Using Saos-2 Cells. *Journal of materials science. Materials in medicine* **2009**, *20*, 1697–1708. https://doi.org/10.1007/s10856-009-3734-0.

Baysan, U.; Koç, M.; Koç, B. Food Powders Particle Properties. In *Food Powders Properties and Characterization*. Springer, 2021; pp 37-52.

Behzadi, S.; Serpooshan, V.; Tao, W.; A. Hamaly, M.; Y. Alkawareek, M.; C. Dreaden, E.; Brown, D.; M. Alkilany, A.; C. Farokhzad, O.; Mahmoudi, M. Cellular Uptake of Nanoparticles: Journey inside the Cell. *Chemical Society Reviews* **2017**, *46* (14), 4218–4244. https://doi.org/10.1039/C6CS00636A.

Bhattacharya, S. Central Composite Design for Response Surface Methodology and Its Application in Pharmacy. In (Ed.), Response Surface Methodology in Engineering Science. *IntechOpen* **2021** https://doi.org/10.5772/intechopen.95835

Bordea, I. R.; Candrea, S.; Alexescu, G. T.; Bran, S.; Băciuț, M.; Băciuț, G.; Lucaciu, O.; Dinu, C. M.; Todea, D. A. Nano-Hydroxyapatite Use in Dentistry: A Systematic Review. *Drug Metabolism Reviews* **2020**, *52* (2), 319–332. https://doi.org/10.1080/03602532.2020.1758713.

Brown, S. D.; Brown, L. A. S. Ethanol (EtOH)-Induced TGF-B1 and Reactive Oxygen Species Production Are Necessary for EtOH-Induced Alveolar Macrophage Dysfunction and Induction of Alternative Activation. *Alcoholism: Clinical and Experimental Research* **2012**, *36* (11), 1952–1962. https://doi.org/10.1111/j.1530-0277.2012.01825.x.

Cai, Y.; Liu, Y.; Yan, W.; Hu, Q.; Tao, J.; Zhang, M.; Shi, Z.; Tang, R. Role of Hydroxyapatite Nanoparticle Size in Bone Cell Proliferation. *J. Mater. Chem.* **2007**, *17* (36), 3780–3787. https://doi.org/10.1039/B705129H.

Cao, G. *Nanostructures and Nanomaterials*. United Kingdom: Imperial College Press, 2004.

Caro, A. A.; Cederbaum, A. I. Oxidative Stress, Toxicology, and Pharmacology of CYP2E1. *Annual Review of Pharmacology and Toxicology* **2004**, *44* (1), 27–42. https://doi.org/10.1146/annurev.pharmtox.44.101802.121704.

Carnovale, C.; Bryant, G.; Shukla, R.; Bansal, V. Identifying Trends in Gold Nanoparticle Toxicity and Uptake: Size, Shape, Capping Ligand, and Biological Corona. *ACS Omega* **2019**, *4* (1), 242–256. https://doi.org/10.1021/acsomega.8b03227.

Choi, S.-J.; Oh, J.-M.; Choy, J.-H. Human-Related Application and Nanotoxicology of Inorganic Particles: Complementary Aspects. *Journal of Materials Chemistry* **2008**, *18* (6), 615–620. https://doi.org/10.1039/B711208D.

Dai, W.; Wang, J.; Gan, X.; Wang, H.; Su, X.; Xi, C. A Systematic Investigation of Dispersion Concentration and Particle Size Distribution of Multi-Wall Carbon Nanotubes in Aqueous Solutions of Various Dispersants. *Colloids and Surfaces A: Physicochemical and Engineering Aspects* **2020**, *589*, 124369. https://doi.org/10.1016/j.colsurfa.2019.124369.

DeLoid, G. M.; Cohen, J. M.; Pyrgiotakis, G.; Demokritou, P. Preparation, Characterization, and in Vitro Dosimetry of Dispersed, Engineered Nanomaterials. *Nat Protoc* **2017**, *12* (2), 355–371. https://doi.org/10.1038/nprot.2016.172.

Demir, E.; Aksakal, S.; Turna, F.; Kaya, B.; Marcos, R. In Vivo Genotoxic Effects of Four Different Nano-Sizes Forms of Silica Nanoparticles in Drosophila Melanogaster. *Journal of Hazardous Materials* **2015**, *283*, 260–266. https://doi.org/10.1016/j.jhazmat.2014.09.029.

Donahue, N. D.; Acar, H.; Wilhelm, S. Concepts of Nanoparticle Cellular Uptake, Intracellular Trafficking, and Kinetics in Nanomedicine. *Advanced Drug Delivery Reviews* **2019**, *143*, 68–96. https://doi.org/10.1016/j.addr.2019.04.008.

Duanis-Assaf, T.; Hu, T.; Lavie, M.; Zhang, Z.; Reches, M. Understanding the Adhesion Mechanism of Hydroxyapatite-Binding Peptide. *Langmuir* **2022**, *38* (3), 968–978. https://doi.org/10.1021/acs.langmuir.1c02293.

Nanotoxicity: The Growing Need for in Vivo Study. *Current Opinion in Biotechnology* **2007**, *18* (6), 565–571. https://doi.org/10.1016/j.copbio.2007.11.008.

Hartmann, N. B.; Jensen, K. A.; Baun, A.; Rasmussen, K.; Rauscher, H.; Tantra, R.; Cupi, D.; Gilliland, D.; Pianella, F.; Riego Sintes, J. M. Techniques and Protocols for Dispersing Nanoparticle Powders in Aqueous Media—Is There a Rationale for

Harmonization? *Journal of Toxicology and Environmental Health, Part B* **2015**, *18* (6), 299–326. https://doi.org/10.1080/10937404.2015.1074969.

He, W.; Mosselhy, D. A.; Zheng, Y.; Feng, Q.; Li, X.; Yang, X.; Yue, L.; Hannula, S.-P. Effects of Silica–Gentamicin Nanohybrids on Osteogenic Differentiation of Human Osteoblast-like SaOS-2 Cells. *Int J Nanomedicine* **2018**, *13*, 877–893. https://doi.org/10.2147/IJN.S147849.

Hotze, E. M.; Phenrat, T.; Lowry, G. V. Nanoparticle Aggregation: Challenges to Understanding Transport and Reactivity in the Environment. *Journal of Environmental Quality* **2010**, *39* (6), 1909–1924. https://doi.org/10.2134/jeq2009.0462.

Ibuki, Y.; Toyooka, T. Nanoparticle Uptake Measured by Flow Cytometry. In *Nanotoxicity: Methods and Protocols*; Reineke, J., Ed.; Methods in Molecular Biology; Humana Press: Totowa, NJ, 2012; pp 157–166. https://doi.org/10.1007/978-1-62703-002-1_11.

Israelachvili, J.N. *Intermolecular and Surface Forces* (3rd edition). United States of America: Elsevier, 2011.

Jacobsen, N. R.; Pojano, G.; Wallin, H.; Jensen, K. A. Nanomaterial dispersion protocol for toxicological studies in ENPRA. *Internal ENPRA Project Report* **2010**, 6.

Jahanbakhsh, A.; Shahrokhi, O.; Maroto-Valer, M. M. Understanding the Role of Wettability Distribution on Pore-Filling and Displacement Patterns in a Homogeneous Structure via Quasi 3D Pore-Scale Modelling. *Sci Rep* **2021**, *11* (1), 17847. https://doi.org/10.1038/s41598-021-97169-8.

Jensen, K.A.; Clausen P.A.; Birkedal R.; Kembouche Y.; Christiansen E.; Jacobsen N.R.; Levin M.; Koponen I.; Wallin H.; de Temmerman P.J.; Mast J.; Guiot C.; Spalla O.; Motzkus C.; Shivachev B.; Rousset D.; Witschger O. Standard Operating Procedures for characterization of the selected manufactured nanomaterial types. *NANOGENOTOX deliverable report n°3 June 2011* **2011**, 78.

Khan, I.; Saeed, K.; Khan, I. Nanoparticles: Properties, Applications and Toxicities. *Arabian Journal of Chemistry* **2019**, *12* (7), 908–931. https://doi.org/10.1016/j.arabjc.2017.05.011.

Khattab, I. S.; Bandarkar, F.; Fakhree, M. A. A.; Jouyban, A. Density, Viscosity, and Surface Tension of Water+ethanol Mixtures from 293 to 323K. *Korean J. Chem. Eng.* **2012**, *29* (6), 812–817. https://doi.org/10.1007/s11814-011-0239-6.

Kresak, M.; Moreno, E. C.; Zahradnik, R. T.; Hay, D. I. Adsorption of Amino Acids onto Hydroxyapatite. *Journal of Colloid and Interface Science* **1977**, *59* (2), 283–292. https://doi.org/10.1016/0021-9797(77)90010-8.

Lu, X.; Xu, P.; Ding, H.-M.; Yu, Y.-S.; Huo, D.; Ma, Y.-Q. Tailoring the Component of Protein Corona via Simple Chemistry. *Nat Commun* **2019**, *10* (1), 4520. https://doi.org/10.1038/s41467-019-12470-5.

Mahbubul, I. M.; Saidur, R.; Amalina, M. A.; Elcioglu, E. B.; Okutucu-Ozyurt, T. Effective Ultrasonication Process for Better Colloidal Dispersion of Nanofluid. *Ultrasonics Sonochemistry* **2015**, *26*, 361–369. https://doi.org/10.1016/j.ultsonch.2015.01.005.

Mansur, H. S.; Mansur, A. A. P.; Bicallho, S. M. C. M. Lignin-Hydroxyapatite/Tricalcium Phosphate Biocomposites: SEM/EDX and FTIR Characterization. *Key Engineering Materials* **2005**, *284–286*, 745–748. https://doi.org/10.4028/www.scientific.net/KEM.284-286.745.

Meirelles, L.; Arvidsson, A.; Andersson, M.; Kjellin, P.; Albrektsson, T.; Wennerberg, A. Nano Hydroxyapatite Structures Influence Early Bone Formation. *Journal of Biomedical Materials Research Part A* **2008**, *87A* (2), 299–307. https://doi.org/10.1002/jbm.a.31744.

Monopoli, M. P.; Walczyk, D.; Campbell, A.; Elia, G.; Lynch, I.; Baldelli Bombelli, F.; Dawson, K. A. Physical−Chemical Aspects of Protein Corona: Relevance to in Vitro and in Vivo Biological Impacts of Nanoparticles. *J. Am. Chem. Soc.* **2011**, *133* (8), 2525–2534. https://doi.org/10.1021/ja107583h.

L. Moore, T.; Rodriguez-Lorenzo, L.; Hirsch, V.; Balog, S.; Urban, D.; Jud, C.; Rothen-Rutishauser, B.; Lattuada, M.; Petri-Fink, A. Nanoparticle Colloidal Stability in Cell Culture Media and Impact on Cellular Interactions. *Chemical Society Reviews* **2015**, *44* (17), 6287–6305. https://doi.org/10.1039/C4CS00487F.

Mosquera, J.; García, I.; Liz-Marzán, L. M. Cellular Uptake of Nanoparticles versus Small Molecules: A Matter of Size. *Acc. Chem. Res.* **2018**, *51* (9), 2305–2313. https://doi.org/10.1021/acs.accounts.8b00292.

Nanommune *Periodic Report Summary - NANOMMUNE (Comprehensive assessment of hazardous effects of engineered nanomaterials on the immune system)*. https://cordis.europa.eu/project/id/214281/reporting (accessed 2022-06-19).

OECD WPMN *Guidance Manual for Sponsors of the OECD Sponsorship Programme for the Testing of Manufacture Nanomaterials*. http://www.olis.oecd.org/olis/2009doc.nsf/linkto/env-jm-mono%282009%2920 (accessed 2022-06-19).

Ohshima, H.; Makino, K. *Colloid and Interface Science in Pharmaceutical Research and Development*. United States of America: Elsevier, 2014.

Porter, D.; Sriram, K.; Wolfarth, M.; Jefferson, A.; Schwegler-Berry, D.; Andrew, M. E.; Castranova, V. A Biocompatible Medium for Nanoparticle Dispersion. *Nanotoxicology* **2008**, *2* (3), 144–154. https://doi.org/10.1080/17435390802318349.

Qayyum, A.; Bhatti, I. A.; Ashar, A.; Jilani, A.; Iqbal, J.; Mohsin, M.; Ishaq, T.; Muhammad, S.; Wageh, S.; Dustgeer, M. R. Prewetting Induced Hydrophilicity to Augment Photocatalytic Activity of Nanocalcite @ Polyester Fabric. *Polymers* **2022**, *14* (2), 295. https://doi.org/10.3390/polym14020295.

Quintero-Quiroz, C.; Acevedo, N.; Zapata-Giraldo, J.; Botero, L. E.; Quintero, J.; Zárate-Triviño, D.; Saldarriaga, J.; Pérez, V. Z. Optimization of Silver Nanoparticle Synthesis by Chemical Reduction and Evaluation of Its Antimicrobial and Toxic Activity. *Biomater Res* **2019**, *23* (1), 27. https://doi.org/10.1186/s40824-019-0173-y.

Raghuwanshi, V. S.; Yu, B.; Browne, C.; Garnier, G. Reversible PH Responsive Bovine Serum Albumin Hydrogel Sponge Nanolayer. *Frontiers in Bioengineering and Biotechnology* **2020**, *8*.

Rehman, I.; Bonfield, W. Characterization of Hydroxyapatite and Carbonated Apatite by Photo Acoustic FTIR Spectroscopy. *Journal of Materials Science: Materials in Medicine* **1997**, *8* (1), 1–4. https://doi.org/10.1023/A:1018570213546.

Reifschneider, O.; Vennemann, A.; Buzanich, G.; Radtke, M.; Reinholz, U.; Riesemeier, H.; Hogeback, J.; Köppen, C.; Großgarten, M.; Sperling, M.; Wiemann, M.; Karst, U. Revealing Silver Nanoparticle Uptake by Macrophages Using SR-MXRF and LA-ICP-MS. *Chem. Res. Toxicol.* **2020**, *33* (5), 1250–1255. https://doi.org/10.1021/acs.chemrestox.9b00507.

Rey, C.; Combes, C.; Drouet, C.; Grossin, D.; Bertrand, G.; Soulié, J. 1.11 Bioactive Calcium Phosphate Compounds: Physical Chemistry☆. *Comprehensive biomaterials II*, 2017. pp 244-290.

Rosen, M. J.; Kunjappu, J. T. *Surfactants and Interfacial Phenomena*; John Wiley & Sons, 2012.

Sabet, S. M.; Mahfuz, H.; Hashemi, J.; Nezakat, M.; Szpunar, J. A. Effects of Sonication Energy on the Dispersion of Carbon Nanotubes in a Vinyl Ester Matrix and Associated Thermo-Mechanical Properties. *J Mater Sci* **2015**, *50* (13), 4729–4740. https://doi.org/10.1007/s10853-015-9024-y.

Sharifi, S.; Behzadi, S.; Laurent, S.; Forrest, M. L.; Stroeve, P.; Mahmoudi, M. Toxicity of Nanomaterials. *Chemical Society Reviews* **2012**, *41* (6), 2323–2343. https://doi.org/10.1039/C1CS15188F.

Stern, S. T.; Adiseshaiah, P. P.; Crist, R. M. Autophagy and Lysosomal Dysfunction as Emerging Mechanisms of Nanomaterial Toxicity. *Part Fibre Toxicol* **2012**, *9* (1), 20. https://doi.org/10.1186/1743-8977-9-20.

Sukhanova, A.; Bozrova, S.; Sokolov, P.; Berestovoy, M.; Karaulov, A.; Nabiev, I. Dependence of Nanoparticle Toxicity on Their Physical and Chemical Properties. *Nanoscale Research Letters* **2018**, *13* (1), 44. https://doi.org/10.1186/s11671-018-2457-x.

Tantra, R.; Tompkins, J.; Quincey, P. Characterisation of the De-Agglomeration Effects of Bovine Serum Albumin on Nanoparticles in Aqueous Suspension. *Colloids and Surfaces B: Biointerfaces* **2010**, *75* (1), 275–281. https://doi.org/10.1016/j.colsurfb.2009.08.049.

Taurozzi, J. S.; Hackley, V. A.; Wiesner, M. R. *Preparation of Nanoscale TiO2 Dispersions in an Environmental Matrix for Eco-Toxicological Assessment*; NIST SP 1200-5r1; National Institute of Standards and Technology, 2013; p NIST SP 1200-5r1. https://doi.org/10.6028/NIST.SP.1200-5r1.

Taurozzi, J. S.; Hackley, V. A.; Wiesner, M. R. Ultrasonic Dispersion of Nanoparticles for Environmental, Health and Safety Assessment – Issues and Recommendations. *Nanotoxicology* **2011**, *5* (4), 711–729. https://doi.org/10.3109/17435390.2010.528846.

Tello, I. F. Z.; Almaraz, G. M. D.; Tapia, M. G.; Ambriz, J. L. A. Controlled Pre-Corrosion Attack and Ultrasonic Fatigue Endurance of Titanium Alloy Ti-6Al-4V. *Lat. Am. j. solids struct.* **2017**, *14*, 512–527. https://doi.org/10.1590/1679-78253113.

Vanaja, K.; Shobha Rani, R. H. Design of Experiments: Concept and Applications of Plackett Burman Design. *Clinical Research and Regulatory Affairs* **2007**, *24* (1), 1–23. https://doi.org/10.1080/10601330701220520.

Visser, J. On Hamaker Constants: A Comparison between Hamaker Constants and Lifshitz-van Der Waals Constants. *Advances in Colloid and Interface Science* **1972**, *3* (4), 331–363. https://doi.org/10.1016/0001-8686(72)85001-2.

Warheit, D. B. Hazard and Risk Assessment Strategies for Nanoparticle Exposures: How Far Have We Come in the Past 10 Years? *F1000Res* **2018**, *7*, 376. https://doi.org/10.12688/f1000research.12691.1.

Yameen, B.; Choi, W. I.; Vilos, C.; Swami, A.; Shi, J.; Farokhzad, O. C. Insight into Nanoparticle Cellular Uptake and Intracellular Targeting. *Journal of Controlled Release* **2014**, *190*, 485–499. https://doi.org/10.1016/j.jconrel.2014.06.038.

Yang, J.; Ma, C.; Tao, J.; Li, J.; Du, K.; Wei, Z.; Chen, C.; Wang, Z.; Zhao, C.; Ma, M. Optimization of Polyvinylamine-Modified Nanocellulose for Chlorpyrifos Adsorption by Central Composite Design. *Carbohydrate Polymers* **2020**, *245*, 116542. https://doi.org/10.1016/j.carbpol.2020.116542.

Yu, S.; Liu, J.; Yin, Y.; Shen, M. Interactions between Engineered Nanoparticles and Dissolved Organic Matter: A Review on Mechanisms and Environmental Effects. *Journal of Environmental Sciences* **2018**, *63*, 198–217. https://doi.org/10.1016/j.jes.2017.06.021.

Yu, Z.; Li, Q.; Wang, J.; Yu, Y.; Wang, Y.; Zhou, Q.; Li, P. Reactive Oxygen Species-Related Nanoparticle Toxicity in the Biomedical Field. *Nanoscale Research Letters* **2020**, *15* (1), 115. https://doi.org/10.1186/s11671-020-03344-7.

Zhao, X.; Heng, B. C.; Xiong, S.; Guo, J.; Tan, T. T.-Y.; Boey, F. Y. C.; Ng, K. W.; Loo, J. S. C. In Vitro Assessment of Cellular Responses to Rod-Shaped Hydroxyapatite Nanoparticles of Varying Lengths and Surface Areas. *Nanotoxicology* **2011**, *5* (2), 182–194. https://doi.org/10.3109/17435390.2010.503943.

Zhu, X. D.; Fan, H. S.; Zhao, C. Y.; Ikoma, T.; Tanaka, M.; Chen, J. Y.; Zhang, X. D. Bovine Serum Albumin Adsorption on Hydroxyapatite and Biphasic Calcium Phosphate and the Correlation with Zeta Potentials and Wettability. *Key Engineering Materials* **2006**, *309–311*, 73–76. https://doi.org/10.4028/www.scientific.net/KEM.309-311.73.

APPENDICES

APPENDIX A

SONICATION PARAMETERS

Sonication is widely used in the dispersion protocols. Although sonication only may not be an efficient way to achieve monodisperse suspensions, the effect of sonication should be assessed before any additive is added to enhance the dispersion status. Available literature shows that some of the nanomaterials can be dispersed via sonication and the exact sonication energy and time can be calculated for those nanomaterials (DeLoid, 2017). However, if the nanomaterial that is to be dispersed forms aggregates and has a rather high polydispersity index, the required energy for efficient dispersion may not be calculated properly. In this case, it can be deduced that the system requires an additive molecule to stabilize the dispersion. For this thesis, DSE of two different sonication methods: probe sonication and bath sonication were evaluated. For probe sonication, DSE for 10%, 30%, and 50% sonication amplitudes were calculated based on $P = mC(dT/dt)$ whereas for bath sonication, the amplitude values were 50% and 100%. Concomitantly, for both HAp and TCP nanomaterials, DSEcr measurements were conducted. For probe sonication: hydrodynamic diameters, Z-averages, and polydispersity index of both nanomaterials were measured via DLS after one-minute sonication for every minute for five minutes. For bath sonication, the measurements were done after five-minute sonication for every five minutes for fifteen minutes.

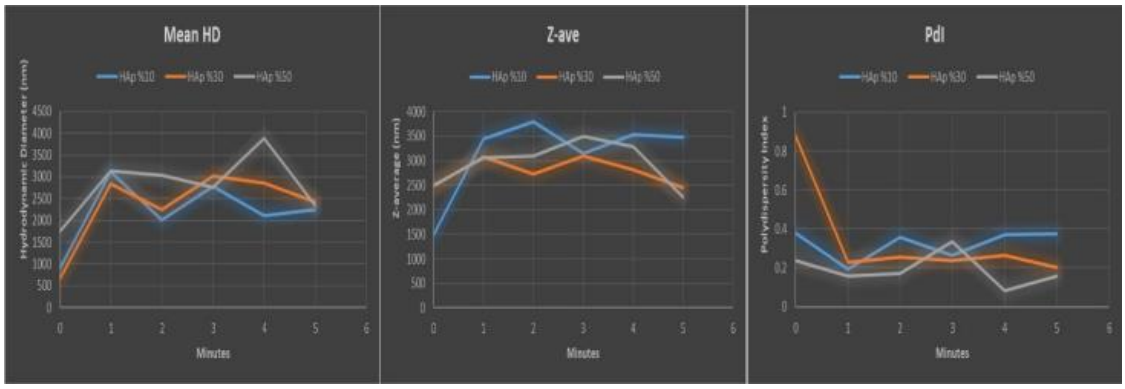

Figure A.1. Critical HAp DSEcr for probe sonication: Mean Peak hydrodynamic diameter (HD), Z-average (Zave), Polydispersity index (PdI) for HAp at three different amplitude values (10, 30, and 50%).

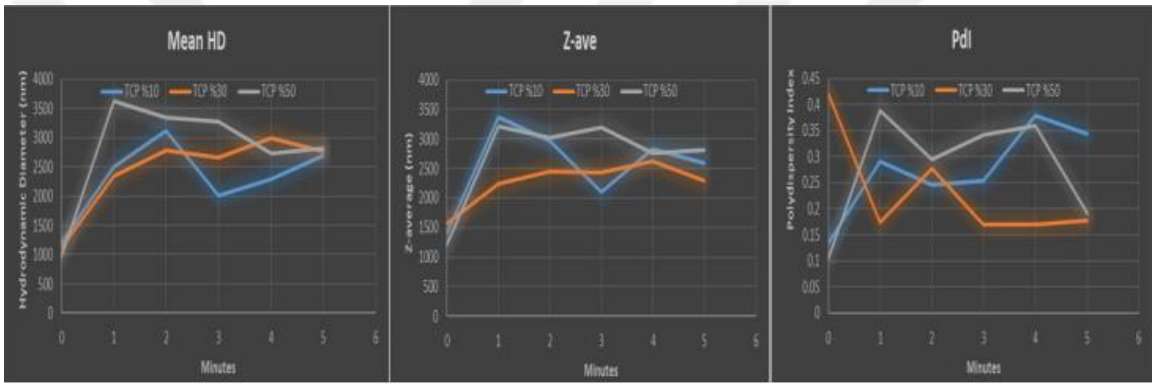

Figure A.2. Critical TCP DSEcr for probe sonication: Mean Peak hydrodynamic diameter (HD), Z-average (Zave), Polydispersity index (PdI) for TCP at three different amplitude values (10, 30, and 50%).

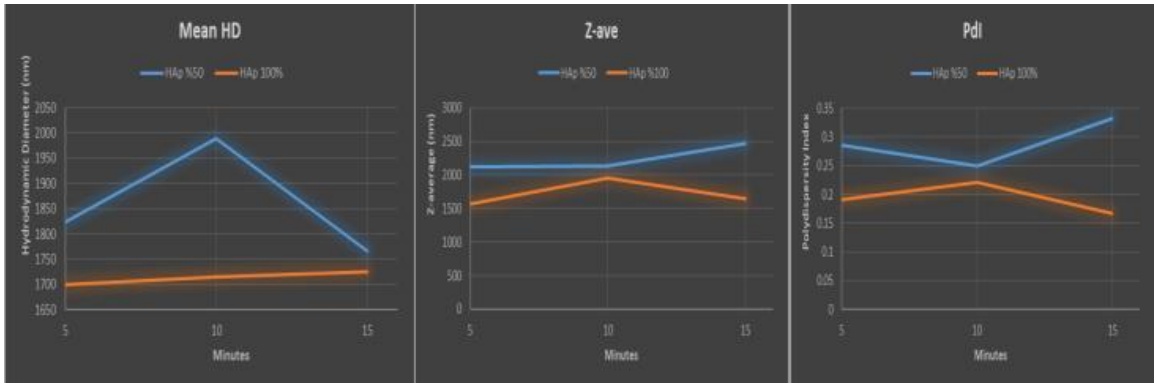

Figure A.3. Critical HAp DSEcr for bath sonication: Mean Peak hydrodynamic diameter (HD), Zaverage (Z-ave), Polydispersity index (PdI) for HAp at two different amplitude values (50% and 100%).

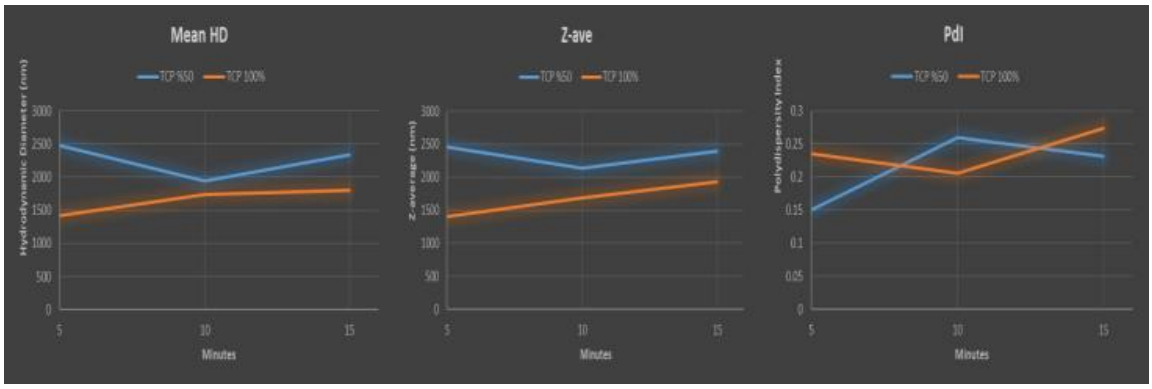

Figure A.4. Critical TCP DSEcr for bath sonication: Mean Peak hydrodynamic diameter (HD), Zaverage (Z-ave), Polydispersity index (PdI) for TCP at two different amplitude values (50% and 100%).

In general, results were not consistent due to the (suspected) polydispersity as shown in Figure A.1., Figure A.2., Figure A.3., and Figure A.4. It was concluded that there was a clear need to use a surfactant-like agent to make the suspension more stable and less aggregated. Although PdI did not necessarily indicate the presence of large aggregates, the hydrodynamic diameter values were not consistent and not correlated with Z-average diameters. Therefore, DSEcr was not calculated for the given samples but final values for HD, Z-ave, and PdI were plotted.

APPENDIX B

MEDIA AND SOLUTION PREPARATION

Dispersion media, solutions to adjust pH levels of dispersion samples, and cell culture complete media were prepared. Ultra-pure water with 18.2 MΩ-cm resistivity was used to prepare all the corresponding solutions that require water.

Prepared dispersion media for experiments are: BSA, PBS, and PBS with BSA. 0.05% weight/volume (w/v) BSA was prepared in two steps: (1) by preparing 1% BSA stocks and (2) dilution and filtration of BSA to 0.05% w/v concentration. 1 gram of BSA was weighed and dissolved in 100 mL of UPW. 100 mL %1 BSA solution was let dissolved in 4^{o}C for 24 hours. The total volume was shared to 10 of 15 mL Falcon tubes and stocks to be used later were stored in -20^{o}C. To dilute and filtrate the 1% stock BSA solution, 10 mL of 1% BSA is first filtrated by using 0.22 µm sterile disposable filters and total volume was completed to 200 mL with either UPW or prepared PBS to achieve 0.05% w/v BSA. PBS solution was prepared by using PBS tablets (Sigma-Aldrich, P4417). 1 tablet was dissolved in 200 mL of UPW to yield 0.01 M phosphate buffer, 0.0027 M potassium chloride, and 0.137 M sodium chloride at pH 7.4 and 25^{o}C. The PBS was used to prepared corresponding 0.05% w/v BSA.

To adjust the pH level of dispersion media, 0.1 M HCl and NaOH solutions were prepared. HCl was prepared from 37% HCl stock solution. Under fume hood, 4.93 mL of 37% HCl was added onto 55.07 mL of UPW and 1 M HCl stock solution was obtained. 1 M HCl was diluted 10-fold and 0.1 M HCl solution was prepared. To prepare 0.1 M NaOH solution, 1 M stock was prepared by weighing 4g of NaOH and dissolving it with 100 mL of UPW. Then obtained solution was diluted 10-fold to prepare 0.1 M NaOH.

Complete cell medium was prepared by using DMEM basal cell medium, heat inactivated FBS, and Penicillin/Streptomycin antibiotic solution (10000 units/mL). The final portions of components are 89% for DMEM basal medium, 10% for FBS, and 1% for Penicillin/Streptomycin.

APPENDIX C

MATERIAL AND ASSAY INTERFERENCE TESTS

The interference of spectrophotometry absorbance of HAp and TCP nanomaterials, MTT solution, and WST-1 solution were assessed. The absorbance spectra of dispersed HAp and TCP were measured between 300-800 nm. The dispersed HAp and TCP with concentrations ranging from 25-400 µg/mL were added into DMEM complete media in 96-well plates. Then the samples were either treated with MTT or WST-1 and incubated for 3 hours to proceed with interference measurements. MTT interference measurement was done at 570 nm with 690 nm non-specific background whereas WST-1 interference measurement was done at 450 nm with 620 nm non-specific background. It has been found that HAp and TCP in DMEM have absorbance peak at around 560 nm (Figure C.1.) and the absorbance wavelengths of nanomaterials in DMEM and MTT have close values. It was shown in Figure C.2. and Figure C.3. that both MTT and WST-1 interference must be considered for the increasing nanomaterial concentrations. According to the results, WST-1 test was selected for the subsequent experiments since nanomaterial in DMEM complete media have absorbance peak very close to MTT formazan absorbance peak (570 nm).

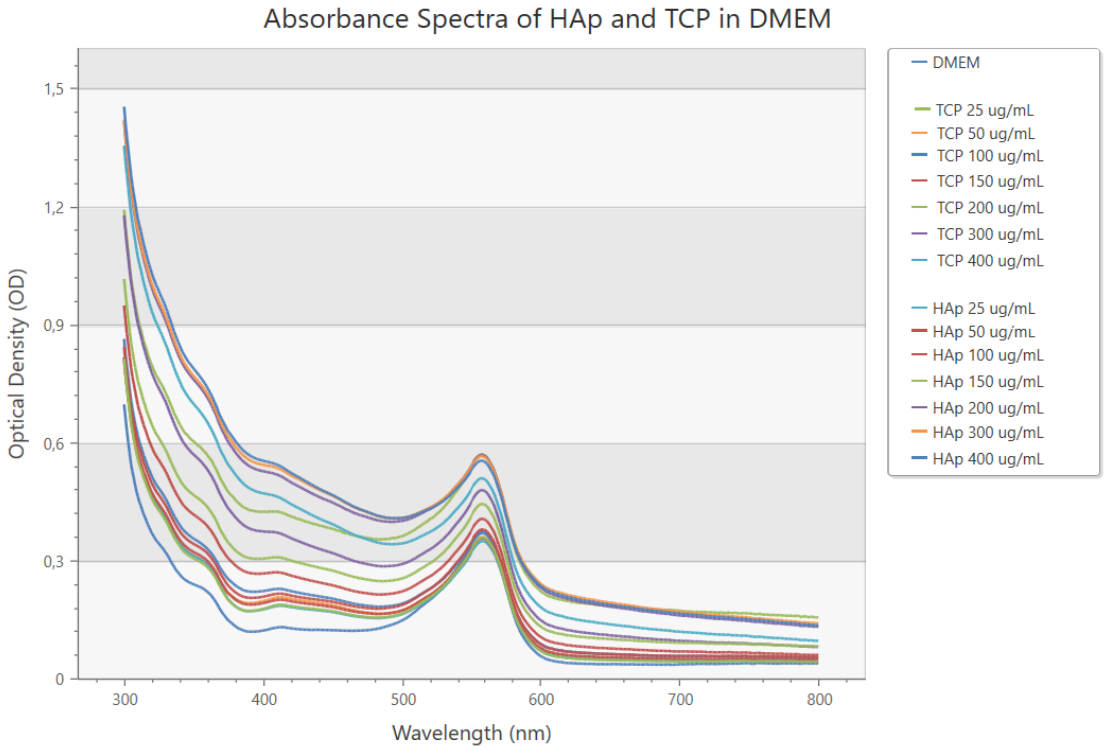

Figure C.1. Absorbance spectra of different concentrations of HAp and TCP in DMEM complete medium.

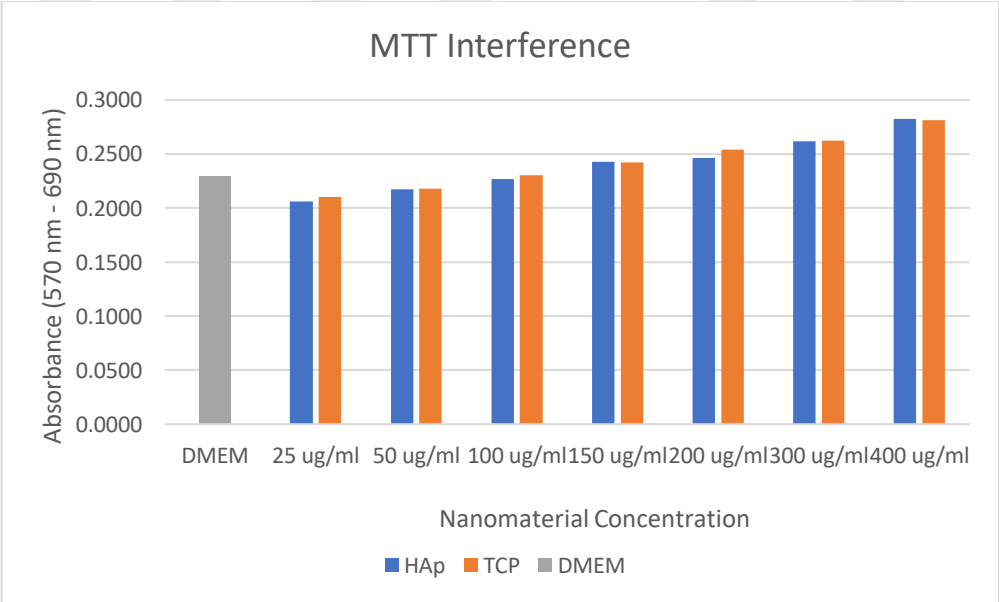

Figure C.2. MTT interference test.

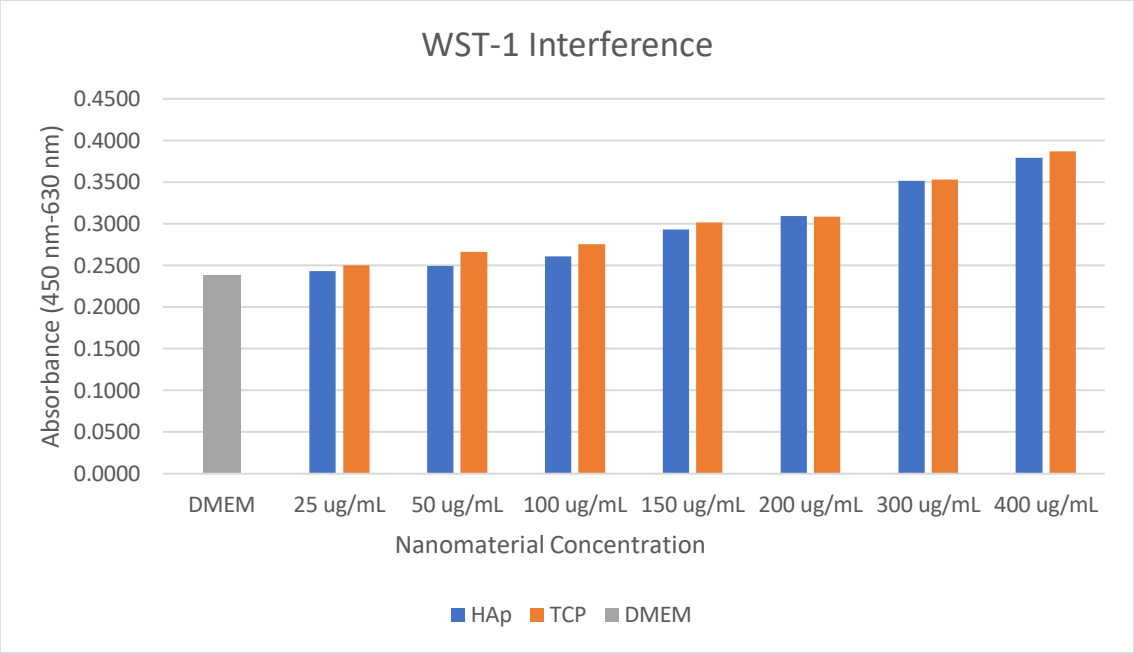

Figure C.3. WST-1 interference test.

APPENDIX D

EVALUATION OF BSA

The role of BSA in dispersion stability is further investigated by analyzing its concentration effect and surface properties. Initially, different concentrations of BSA were used to dispersed 1 mg/mL nanomaterials in pH 10. The fluctuating pattern was observed (Figure D.1.) as the concentration of BSA is not directly correlated with the decrease in the Z-average and magnitude of zeta potential values of the nanomaterials. These results represent that the effect of BSA and its concentration can be further analyzed in future.

Solvent accessible amino acids were determined via PyMOL software with using findSurfaceResidues.py script available via Python Module. The cut-off argument value of the script was set to 3 and doShow argument has been selected as 1 to represent the different layers of surface amino acids. The alpha carbons of all amino acids of BSA can be seen in Figure D.2. The most-inner layer amino acids are represented as white colored whereas the red colored amino acids are the most-outer layer. The content of solvent accessible residues can be seen in Table D.1.

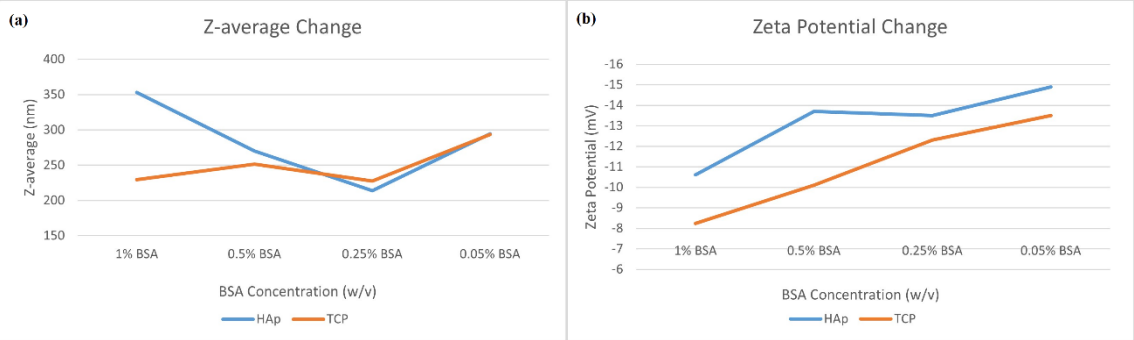

Figure D.1. Effect of BSA concentration on HAp and TCP (a) Z-average and (b) zeta potential values.

Table D.1. The amino acid content of BSA represented as inner, mid, and outer layer based on solvent accessibility.

	Inner Layer	Mid Layer	Outer Layer
Alanine	16	54	22
Cysteine	25	15	30
Aspartic Acid	0	21	60
Glutamic Acid	2	32	84
Phenylalanine	14	8	32
Glycine	8	22	2
Histidine	3	7	24
Isoleucine	10	0	18
Lysine	0	39	79
Leucine	32	4	86
Methionine	2	3	3
Aspargine	2	4	22
Proline	3	22	31
Glutamine	6	11	23
Arginine	0	8	41
Serine	15	19	23
Threonine	3	13	52
Tryptophan	0	0	4
Tyrosine	7	6	27
Valine	23	12	37

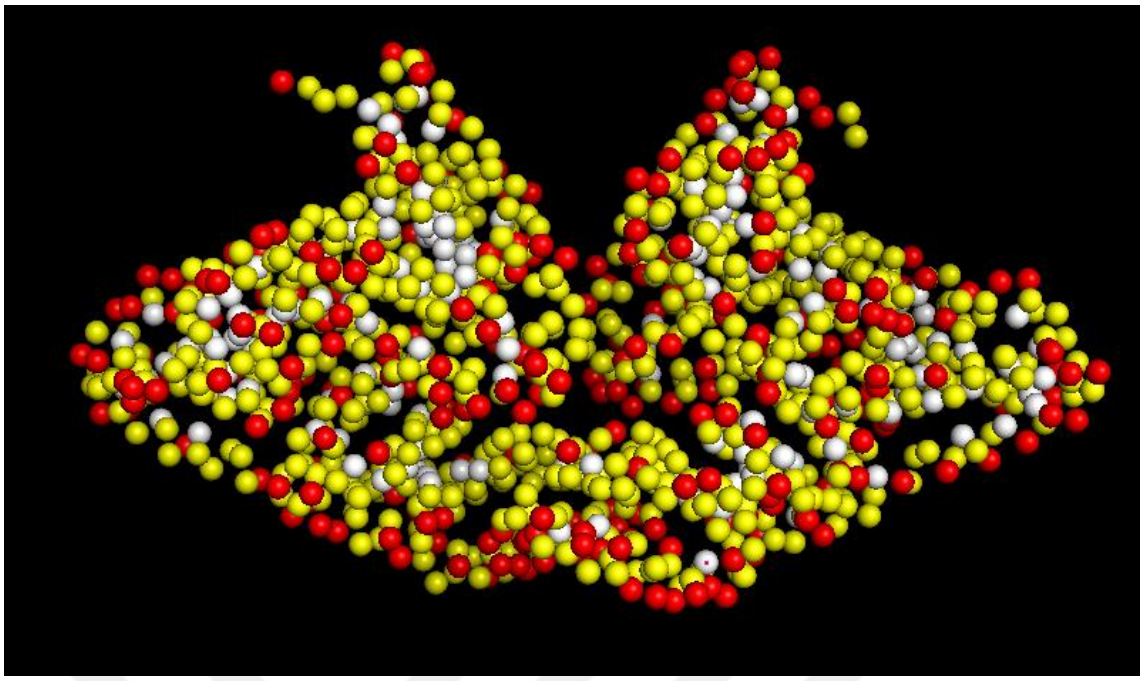

Figure D.2. Alpha carbons of all amino acids of BSA. Red-colored dots represent the outer, yellow-colored represent the mid, and white-colored represent the inner residues according to the cut-off values

Furthermore, surface charge characteristics of BSA in different pH were investigated. First, 4f5s protein data bank (PDB) data was used to create PDB, Qharge, and Radius (PQR) format files of BSA in different pH ranging from 5 to 10 by using PDB2PQR software available in Poisson-Boltzmann server (https://server.poissonboltzmann.org/pdb2pqr). PROPKA script was used to import pKa values of amino acids and AMBER was selected as a forcefield. Achieved PQR files of BSA were analyzed with APBS plugin of PyMOL for the charge density representation as shown in Figure D.1. Blue regions represent positive charges whereas red regions represent negative charges. It has been seen that as the pH increases, the local charges of BSA are more abundant in negatively charged regions as expected due to the isoelectric point of BSA. However, conformational changes of BSA in different pH levels must be considered when BSA-nanoparticle interaction is to be evaluated.

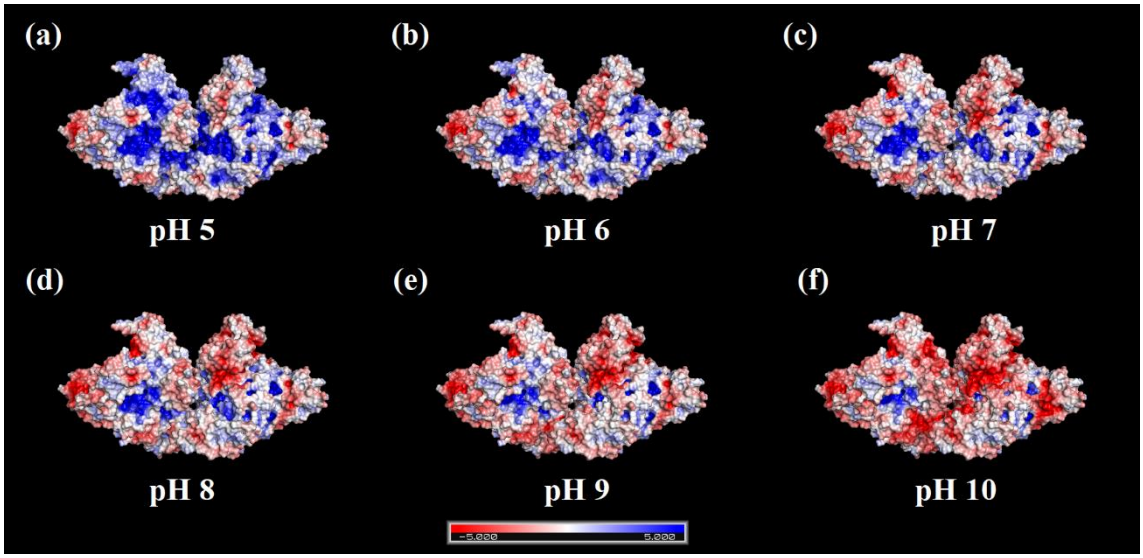

Figure D.3. Charge densities of BSA in (a) pH 5, (b) pH 6, (c) pH 7, (d) pH 8, (e) pH 9, and (f) pH 10. The blue color represents positively charged local areas whereas the red color shows negatively charged residues.

APPENDIX E

SUPPLEMENTARY FIGURES

SEM images that represent individual nanoparticle size, dispersion stability of HAp and TCP, and differences between probe and bath sonication in terms of SEM images and DLS size measurements are shown. It is shown in Figure E.1. that both HAp and TCP are dominant in spherical particles. 1 week stability results show that HAp is relatively stable 1 week after dispersion whereas TCP shows unpredictable aggregation behavior (Figure E.2.). Additionally, Figure E.3. shows whether the sonication method disrupts the nanomaterials or not. Nanomaterial shape is not changed depending on the sonication method used.

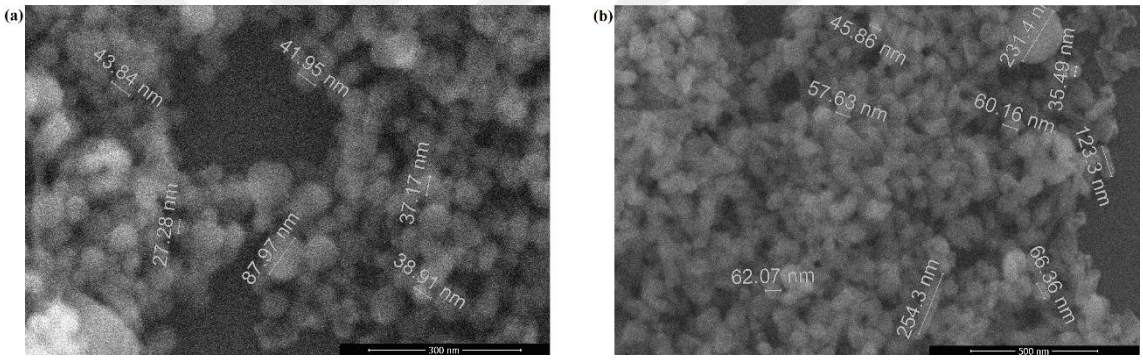

Figure E.1. SEM images for (a) HAp and (b) TCP.

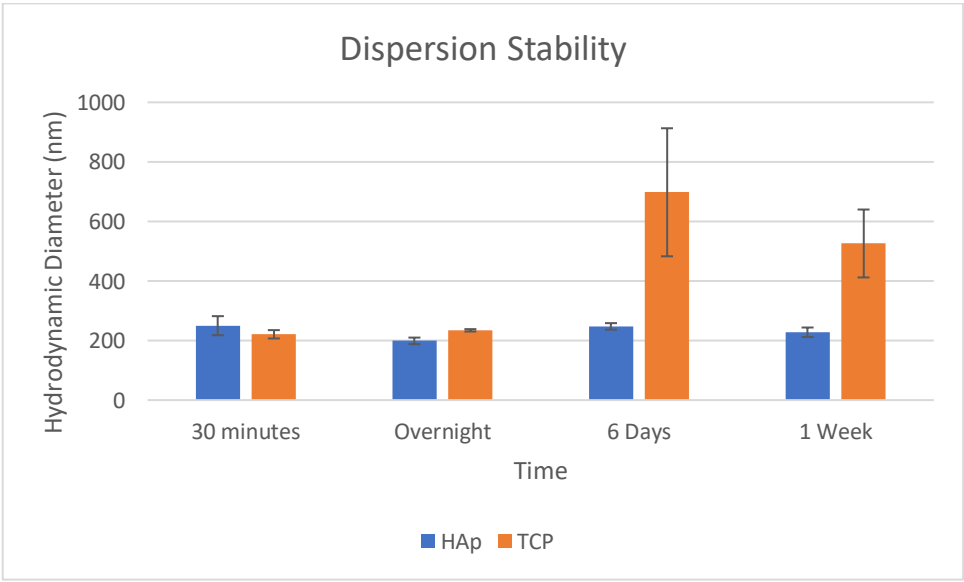

Figure E.2. Dispersion stability of HAp and TCP.

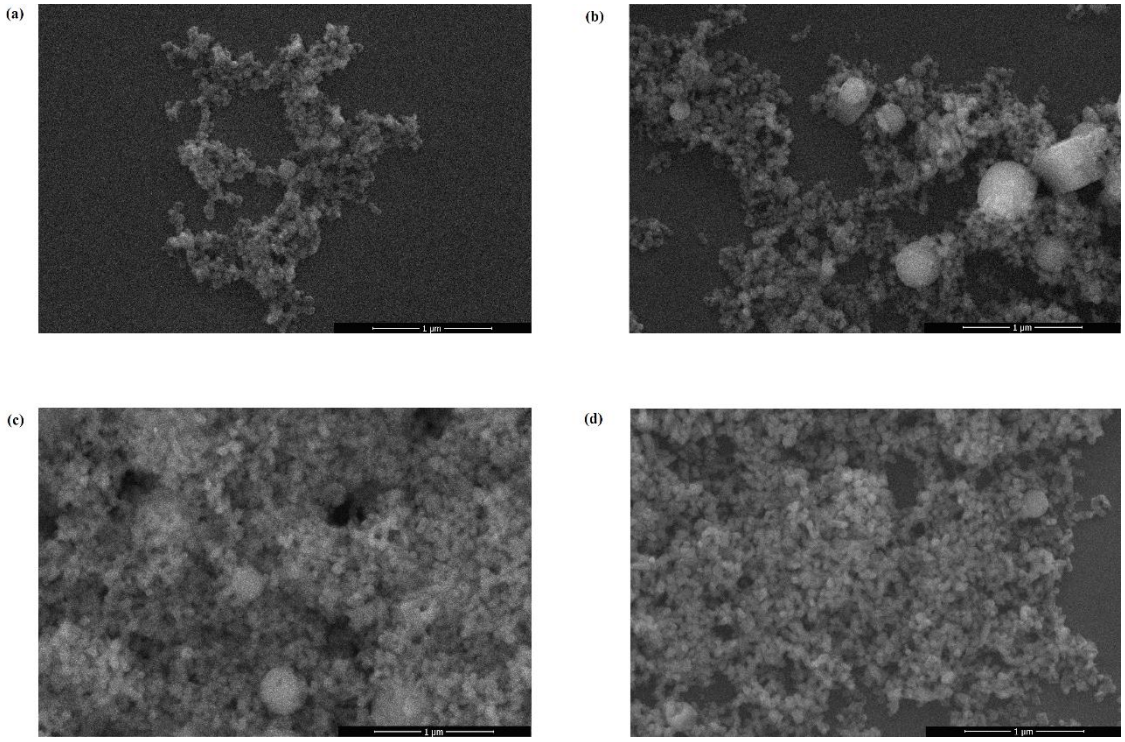

Figure E.3. SEM images of (a) HAp dispersed with bath sonicator, (b) HAp dispersed with probe sonicator, (c) TCP dispersed with bath sonicator, (d) TCP dispersed with probe sonicator.

APPENDIX F

UPTAKE POTENTIAL ASSESSMENT

When a nanoparticle gets near the cell, it interacts with the plasma membrane components. In particular, uptake of the nanoparticle by the cell is highly regulated with rather complex biomolecular interactions (Behzadi et al., 2017). Nanoparticle must overcome the plasma membrane's selective permeability to be internalized successfully (Behzadi et al., 2017). Structural constitution and characteristics of plasma membrane result in overall negative charge with locally cationic regions conferring selective permeability to biological molecules and charged molecules including nanoparticles (Behzadi et al., 2017). Moreover, there are multiple routes of entry for the cellular internalization of nanoparticles, applicable for both *in vivo* and *in vitro* cell exposure. In two distinct categories, these routes can be defined as direct cellular entry and endocytosis-based uptake pathways (Behzadi et al., 2017).

Although endocytosis-based nanoparticle uptake is the common route of internalization, nanoparticles can cross lipid bilayer of cells via alternative pathways, avoiding the endosomal cover and energy-requiring transportation mechanisms (Donahue et al., 2019). Direct translocation, lipid fusion, electroporation, and microinjection are examples of such alternative paths (Donahue et al., 2019). Direct cytoplasmic entry of nanoparticles may occur due to the engagement of the nanoparticles with lipid bilayer. The plasma membrane may be disrupted by the engaging nanoparticle for the direct translocation into cytoplasm (Donahue et al., 2019). Properties of nanoparticles such as their shape, size, and coating material affect the direct translocation. Alternatively, nanoparticles can be internalized via assisting vessels formed by lipids. These vessels can fuse with plasma membrane and bound nanoparticles can be translocated into the cytosol through lipid fusion (Donahue et al., 2019). As invasive approaches, electroporation and microinjection can be used as well to deliver nanoparticles into the cells. Electroporation is a strategy that relies on the physical disruption of plasma membrane upon electricity (Donahue et al., 2019). Due to this disruption, transient pores are created on the surface of the cells and nanoparticles may enter through those pores (Donahue et al., 2019). On the other hand, microinjection relies on the direct injection of nanoparticles into the

cytoplasm by microinjectors that can penetrate plasma membrane without harming the whole structure (Donahue et al., 2019). Despite internalization of nanoparticles can occur via direct cytoplasmic entry, endocytosis-based routes are mechanistically more favorable for the cells because of high regulation and intracellular targeting opportunities (Donahue et al., 2019).

Endocytosis-based nanoparticle uptake occurs through the invaginations of the plasma membrane via engulfment (Mosquera et al., 2018). Formation of endocytic vesicles lead the internalized nanoparticle to its intracellular destination. Whole process of endocytosis can be occurred via many distinct paths based on the type of cell, composition of biological molecules and physicochemical characteristics of the nanoparticle (Mosquera et al., 2018). Five prominent endocytosis types are: phagocytosis, clathrin-mediated endocytosis, caveolin-mediated endocytosis, clathrin-caveolin-independent endocytosis, and macropinocytosis (Donahue et al., 2019). Phagocytosis mainly occurs in phagocytes and usually is involved in the main host defense mechanism for the organism, however, cell types such as epithelial and endothelial cells may possess phagocytic activity as well (Donahue et al., 2019). Nanoparticles that recruit proteins onto their surfaces may initiate phagocytosis in cells. This NP-Protein complex can be recognized by cell membrane receptors in which upon recognition, actin reorganization cause formation of surface extensions and engulfment occurs (Mosquera et al., 2018). Generally, larger NPs can be internalized via phagocytosis (Mosquera et al., 2018). As another path, nanoparticles may get into cells via clathrin-mediated endocytosis. Clathrin-mediated endocytosis is the main route of the uptake of nutrients, biological components such as cholesterol and iron through transferrin carriers (Mosquera et al., 2018). Clathrin is a protein complex found on the plasma membrane and composed of assembly units called triskelions (Mosquera et al., 2018). These three-legged structures with three heavy and three light chains assemble the complex constitution which is responsible for the stability and generation of the budding vesicle (Mosquera et al., 2018). Additionally, adaptor and accessory proteins localized on the cytosolic site of the plasma membrane coordinates clathrin nucleation which promotes the lattice formation instead of pentagons or hexagons to induce invagination of the lipid bilayer into clathrin-coated endocytic vesicles for the uptake of NP (Donahue et al., 2019). In clathrin-mediated endocytosis, nucleation occurs for the formation of coated pits, plasma membrane bends and invagination are mediated, membrane is cleaved to conclude vesicle formation, and uncoating occurs depending on the intracellular trafficking and endocytic proteins are

recovered (Donahue et al., 2019). Intracellular vesicles that are formed via clathrin-mediated endocytosis exhibit approximate sizes between 100 nm and 500 nm (Donahue et al., 2019). Alternatively, caveolin-mediated endocytosis can be utilized in nanoparticle internalization. Caveolin-mediated endocytosis is used by cells in various mechanisms such as cell signaling and regulation of lipids, fatty acids, and proteins (Donahue et al., 2019). Invaginations in shape of flasks that are called caveolae are dispersed throughout the dense region of bodies anchored in cytoskeleton (Donahue et al., 2019). As in clathrin-mediated endocytosis, principle is the recruitment of the proteins for the formation of endocytic vesicle and detachment of the vesicle from the plasma membrane for the intracellular targeting. The flask-shaped vesicles with 50-100 nm diameter are stabilized by caveolin proteins and formed vesicle is then guided to intracellular locations upon activation of complex signaling cascades (Donahue et al., 2019). Endocytosis can also be mediated independent from clathrin or caveolin indicated mechanisms. In such cases, NPs may enter through endocytosis via formation of lipid rafts generated on cholesterol and sphingolipid-rich domains (Donahue et al., 2019). This lipid raft-mediated endocytosis that is one of the prevalent routes for immunological responses can be an alternative route for NP entry into the cell (Donahue et al., 2019). Moreover, one of the unique pinocytosis mechanisms, macropinocytosis is a non-specific cellular uptake mechanism that relies on the extension of the plasma membrane that fuses back into the membrane upon engulfment of the NPs (Behzadi et al., 2017). Macropinocytosis is an important mechanism for the immune system because of its involvement in antigen representation (Behzadi et al., 2017). To summarize, NPs that possess distinct physicochemical characteristics are internalized via various cellular uptake mechanisms. The governance of the uptake is related to the characteristic features of the NPs and their interactions with the cellular components.

Cellular internalization of NPs is strongly influenced by the physicochemical properties of the nanomaterial. For a NP to penetrate the cell membrane, it must be present nearby the cell and interact with it. This interaction may result in uptake of the NP based on its surface characteristics since properties such as shape and surface charge affect the NP recognition and uptake by cells (Behzadi et al., 2017). It can be deduced from the cellular uptake mechanisms that size of the nanoparticle also has a pivotal role in the uptake route and rate. The combination of these parameters and their effectiveness leads to the necessity of the evaluation of these physicochemical characteristics and their contribution to the cell-nanoparticle interaction. Since dispersion is also governed by the

physicochemical properties of the nanoparticles, state of dispersion is directly linked to the outcome of the cell-nanoparticle interactions.

In this thesis, cellular uptake analysis of HAp and TCP nanoparticles was done via flow cytometer (Beckman Coulter, CytoFLEX) to assess nanoparticle uptake potential of SaOS-2 cells. The evaluation of nanoparticle uptake potential was done via forward-scatter (FSC, X axis) versus side-scatter (SSC, Y axis) plot. The forward-scattered light from flow cytometer corresponds to the cell's size and particle's size whereas side-scatter intensity can be evaluated for the granular content within a cell or a particle (Ibuki & Toyooka, 2012). Consequently, it was proposed that nanoparticle uptake by a cell result in increased side-scatter intensity whilst forward-scatter intensity remains unchanged (Ibuki & Toyooka, 2012).

Cultured SaOS-2 cells between passage numbers 1-10 after thawing were used. Cells were subcultured to 12-well plates as 5 x 10^4 cells/well and incubated for 24 hours under 37^{o}C and 5% CO_2 atmosphere. After 24 hours, cells were treated with 150 µg/mL HAp dispersed by following NANOREG dispersion protocol and untreated cells were used as controls. Cells were incubated under 37^{o}C and %5 CO_2 conditions for 24 hours after treatment. The media was discarded, and wells were rinsed with PBS without disturbing the cells. Cells then were treated with 1 mL of trypsin and incubated for 5 minutes under 37^{o}C and %5 CO_2. 1 mL of complete DMEM high glucose media were added to each well and samples were collected to individual 15 mL falcon tubes for centrifugation with 1000 RPM for 5 minutes. After centrifugation, supernatant was discarded, and cell pellet was dissolved in 2 mL of FCM Buffer containing 0.2% Pluronic® F68 (Sigma-Aldrich, P1300) and 1 mmol/L EDTA in PBS. Each sample was analyzed as triplicates via FCM with total cell count determined as 20000. Side-scatter versus forward-scatter pseudocolor graphs were plotted. The graphs were compartmentalized to four distinct quartiles (Q1, Q2, Q3, and Q4) to mark different levels of side-scatter intensities. Changes in distribution profile of cells were investigated according to the compartmentalized quartiles. It was seen in Figure F.1. and Figure F.2. that the side-scatter intensity, hence the granular size inside the cells, have been increased in nanoparticle treated SaOS-2 cells compared to the control. This may be a preliminary result to investigate nanoparticle uptake of the SaOS-2 cells as a next step. Therefore, further analyses can be conducted for the evaluation of nanoparticle uptake change depending on the dispersion stability and aggregate size.

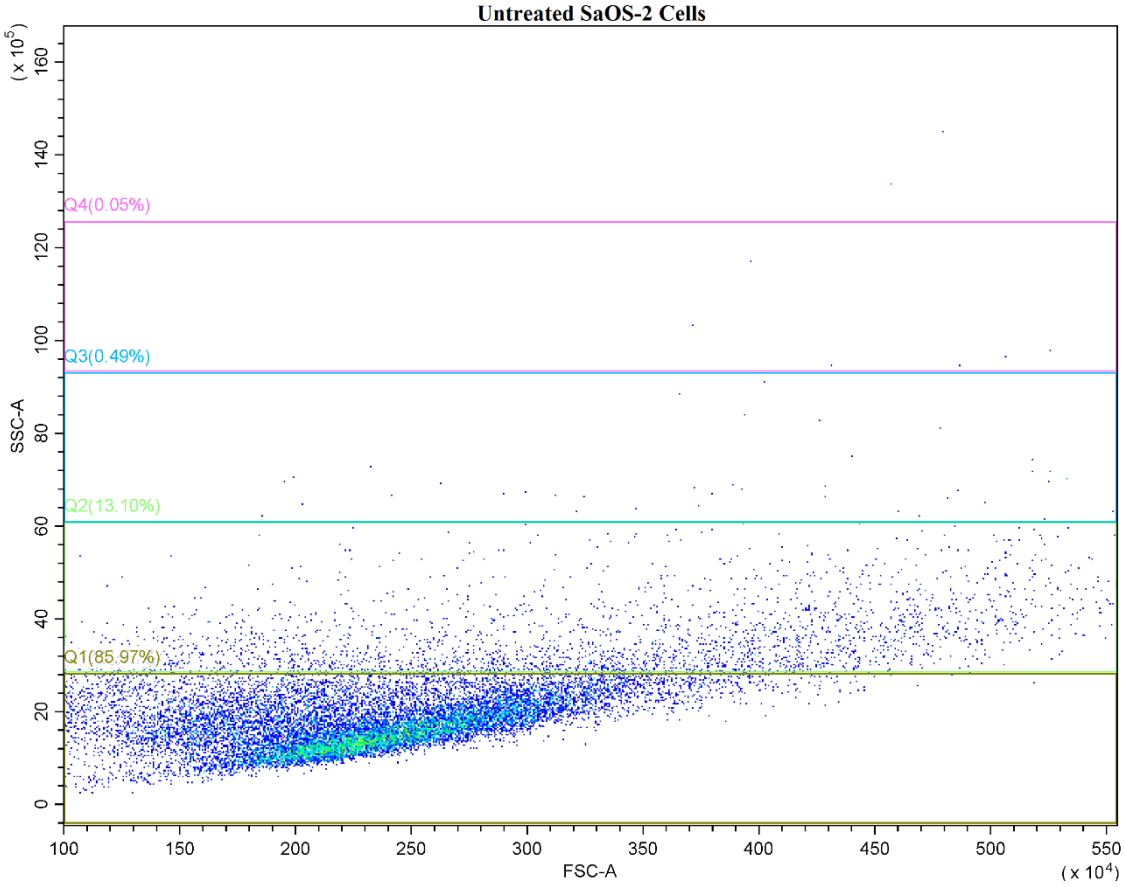

Figure F.1. Distribution of untreated SaOS-2 cells according to the SSC vs. FSC intensities.

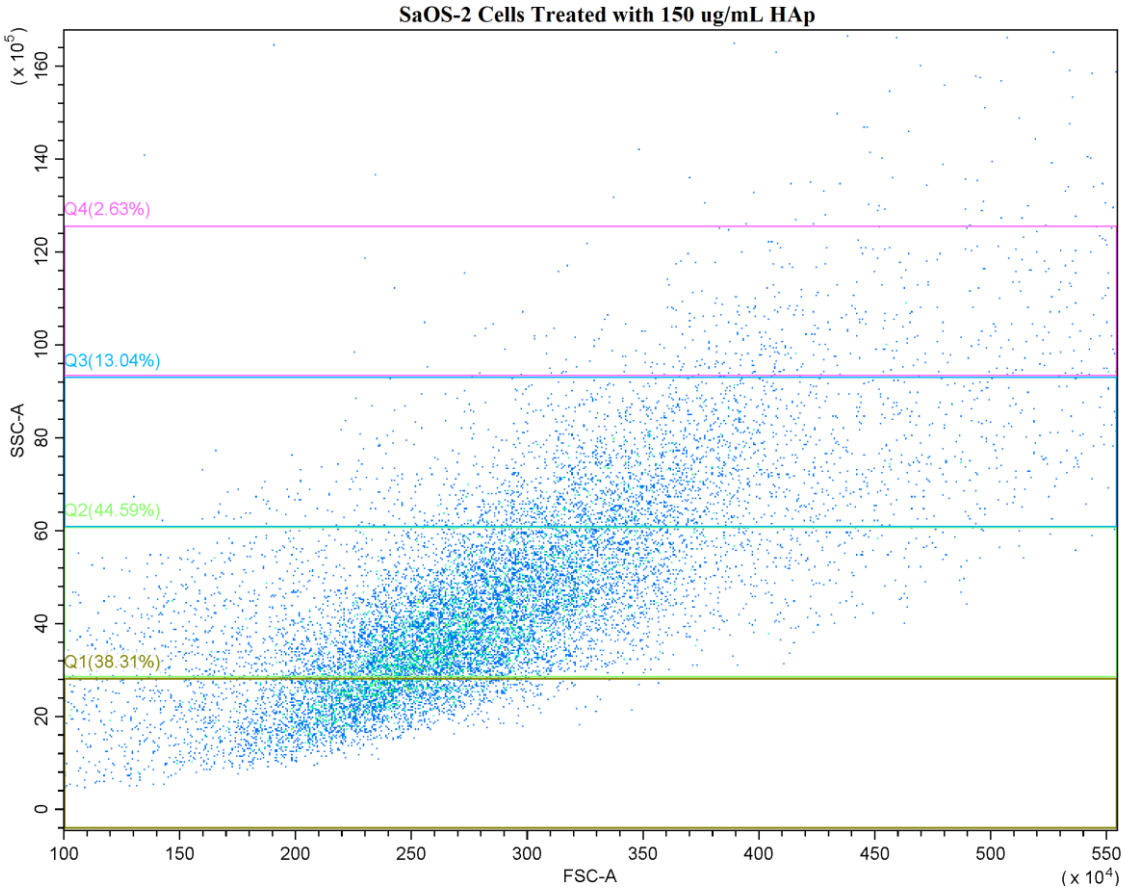

Figure F.2. Distribution of SaOS-2 cells treated with 150 µg/mL HAp, according to the SSC vs. FSC intensities.